

November 2018

Multilayer Dielectric Rod Waveguide and Dielectric Rod Antenna with Enhanced Performance

Denise C. Lugo

University of South Florida, deniselugo@mail.usf.edu

Follow this and additional works at: <https://scholarcommons.usf.edu/etd>



Part of the [Electrical and Computer Engineering Commons](#)

Scholar Commons Citation

Lugo, Denise C., "Multilayer Dielectric Rod Waveguide and Dielectric Rod Antenna with Enhanced Performance" (2018). *Graduate Theses and Dissertations*.
<https://scholarcommons.usf.edu/etd/8125>

This Dissertation is brought to you for free and open access by the Graduate School at Scholar Commons. It has been accepted for inclusion in Graduate Theses and Dissertations by an authorized administrator of Scholar Commons. For more information, please contact scholarcommons@usf.edu.

Multilayer Dielectric Rod Waveguide and Dielectric Rod Antenna with Enhanced Performance

by

Denise C. Lugo

A dissertation submitted in partial fulfillment
of the requirements for the degree of
Doctor of Philosophy in Electrical Engineering
Department of Electrical Engineering
College of Engineering
University of South Florida

Co-Major Professor: Thomas M. Weller, Ph.D.
Co-Major Professor: Jing Wang, Ph.D.
Gokhan Mumcu, Ph.D.
Rasim Guldiken, Ph.D.
Thomas Ketterl, Ph.D.

Date of Approval:
July 27, 2018

Keywords: Additive manufacturing, dielectric end-fire antenna, Ku band, microstrip transition, modeling, 3D-printing

Copyright © 2018, Denise C. Lugo

DEDICATION

To my family and friends

To my professors and mentors

ACKNOWLEDGMENTS

I would like to express my deepest appreciation to Dr. Thomas Weller for his enormous contribution to this work. His vast knowledge, love for teaching and impeccable work ethics are values that will stay with me in my future professional endeavours.

In addition, I would like to thank Dr. Jing Wang for his guidance and encouragement which were crucial for the completion of this dissertation.

I would like to thank the committee members Dr. Gokham Mumcu, Dr. Rasim Guldiken, Dr. Thomas Ketterl, Dr. Yu Sun and the committee chair Dr. Venkat Bhethanabotla for their time and their greatly appreciated suggestions.

My sincere gratitude to the National Science Foundation (NSF), Sciperio, Nscrypt and Rogers for their financial support and valuable donations.

I want to thank my former advisors Dr. Francisco Garcia, Dr. Adelmo Ortiz and Dr. Juan Muci for instilling in me the discipline to carry out a research project and for providing me tools to succeed in my graduate studies.

To the Electrical Engineering faculty members and staff, the NREC staff and the USF machine shop for providing cutting edge facilities and excellent advising.

Many thanks go out to my WAMI friends for their help and for the uncountable good experiences that shaped this journey.

This work would not have been possible without the love and support of my family, friends and my dog Dylan J.

TABLE OF CONTENTS

LIST OF TABLES.....	iii
LIST OF FIGURES.....	iv
ABSTRACT.....	vii
CHAPTER 1: INTRODUCTION.....	1
1.1. Introduction.....	1
1.2. Contributions.....	3
1.3. Dissertation Outline.....	4
CHAPTER 2: BACKGROUND AND LITERATURE REVIEW.....	5
2.1. Introduction.....	5
2.2. Millimeter-Wave and THz Dielectric Waveguides.....	6
2.2.1. Hollow Core Dielectric Waveguides.....	6
2.2.2. Porous Core Dielectric Waveguides.....	7
2.2.3. Solid Core Dielectric Waveguides.....	8
2.2.4. Transition for Dielectric Rod Waveguides to Planar Transmission Lines.....	10
CHAPTER 3: ANALYTICAL STUDY OF MULTILAYER DIELECTRIC ROD WAVEGUIDES.....	13
3.1. Introduction.....	13
3.2. Multilayer Dielectric Rod Waveguide (DRW).....	14
3.2.1. Design Considerations.....	14
3.2.2. Modal Analysis.....	17
3.3. Explicit Model for the Cutoff Frequency of the Multilayer DRW.....	21
3.4. The Cladding Effect on the Multilayer DRW Performance.....	22
3.4.1. Loss Tangent Variation.....	22
3.4.2. Cladding Dimension Variation.....	24
3.4.3. Cladding Permittivity Variation.....	24
3.5. DRW Experimental Characterization at the Ku Band.....	25
3.5.1. Straight DRW Characterization with and Without Cladding.....	25
3.5.2. Dielectric Rod Waveguide Bends.....	28
3.5.3. Loss Analysis for the Multilayer DRW.....	30
3.6. D Band Dielectric Rod Waveguide.....	33
3.7. Conclusions.....	34
CHAPTER 4: KU-BAND ADDITIVE MANUFACTURED MULTILAYER DIELECTRIC ROD WAVEGUIDE.....	36
4.1. Introduction.....	36
4.2. Preparation and Characterization of the Medium- k Electromagnetic Composites for FDM.....	36
4.2.1. Preparation of Ceramic Thermoplastic EM Composites.....	36
4.2.2. Dielectric Characterization of EM Composites.....	37
4.3. Multilayer Dielectric Rod Waveguide (DRW) Design and Fabrication.....	37
4.4. Characterization and Measured Results.....	38
4.5. Conclusions.....	40
CHAPTER 5: KU BAND METAL-STRIP-LOADED DIELECTRIC ROD WAVEGUIDE FILTER.....	41
5.1. Introduction.....	41
5.2. Metal-Strip-Loaded Dielectric Rod Waveguide (MSL DRW) Design and Fabrication.....	41
5.3. MSL DRW Characterization and Measured Results.....	42

5.4. Conclusions	44
CHAPTER 6: MULTILAYER DIELECTRIC END-FIRE ANTENNA WITH ENHANCED GAIN.....	45
6.1. Introduction	45
6.2. Dielectric Rod Antenna Design and Fabrication	46
6.3. DRA Characterization and Measurements	47
6.4. Parametric Study of the Cladding Properties.....	52
6.5. Conclusions	54
CHAPTER 7: 3D PRINTED MULTILAYER MM-WAVE DIELECTRIC ROD ANTENNA WITH ENHANCED GAIN	55
7.1. Introduction	55
7.2. Preparation and Characterization of the Medium- <i>K</i> Electromagnetic Composite for FDM.....	55
7.3. Dielectric Rod Antenna (DRA) Design and Fabrication	56
7.4. Measured Results	57
7.5. Conclusions	58
CHAPTER 8: KU BAND METAL-STRIP-LOADED DIELECTRIC ROD ANTENNA WITH NARROWBAND GAIN ENHANCEMENT	59
8.1. Introduction	59
8.2. Metal-Strip-Loaded Dielectric Rod Antenna (MSL DRA) Design and Fabrication	59
8.3. MSL DRA Characterization and Measured Results	60
8.4. Conclusions	62
CHAPTER 9: KU BAND BROADBAND TRANSITION FOR DIELECTRIC ROD WAVEGUIDES TO PLANAR TRANSMISSION LINES	63
9.1. Introduction	63
9.2. Transition Design and Fabrication	63
9.2.1. Design Considerations	63
9.2.2. Fabrication	65
9.3. Characterization and Measured Data.....	66
9.4. Transition Loss Analysis	67
9.5. DRA Planar Feed Characterization and Measured Data	68
9.6. Conclusions	71
CHAPTER 10: RECOMMENDATIONS AND FUTURE WORK	72
REFERENCES	73
APPENDIX A: COPYRIGHT PERMISSIONS	79
A.1. Permissions for Chapter 3.....	79
A.2. Permissions for Chapter 4.....	80
A.3. Permissions for Chapter 6.....	81
A.4. Permissions for Chapter 7.....	82
ABOUT THE AUTHOR	END PAGE

LIST OF TABLES

Table 8-1: Peak gain frequency and variation with LM.....	61
Table 9-1: Transition dimensions of interest	65

LIST OF FIGURES

Figure 2-1:	Illustration of some hollow core dielectric waveguides configurations	7
Figure 2-2:	Illustration of some porous dielectric waveguides configurations	8
Figure 2-3:	Illustration of solid core dielectric waveguides configurations	9
Figure 2-4:	Illustration of dielectric slab (a), ribbon (b) and dielectric rod (c) waveguides.....	10
Figure 2-5:	Dielectric rod waveguide and microstrip line interconnect design for the G band [47]	11
Figure 2-6:	Transition between rectangular dielectric rod waveguide and microstrip design (left) and simulated data (right) from 60 to 90 GHz [48].....	11
Figure 2-7:	Transition for dielectric rod waveguide to CPW at D band [49].....	12
Figure 2-8:	PCB-embedding scheme for dielectric ribbon waveguide at D band [46]	12
Figure 3-1:	Multilayer dielectric rod waveguide cross-section and key parameters	14
Figure 3-2:	Electric field magnitude of the fundamental mode for different core and cladding permittivity at 14 GHz.....	16
Figure 3-3:	DRW fundamental mode E and H field vectors (a) E_{y11} field magnitude (b) and E_{y11} field vector (c) in the core cross-section	17
Figure 3-4:	DRW E-field magnitude and vector for the first 3 higher order modes in a DRW with 2:1 aspect ratio and air cladding (a) and other common higher order modes (b)	18
Figure 3-5:	Dielectric rod waveguide normalized phase constants for the first 4 modes using Marcatali's explicit approximation [51] and numerical simulation.....	19
Figure 3-6:	Cross-section of a DRW indicating the field variations in the core and cladding and the gray regions not considered in Marcatali's approximation	20
Figure 3-7:	Simulated cutoff frequency for the dielectric rod waveguide fundamental mode and proposed model playback.....	21
Figure 3-8:	DRW normalized phase constants for the fundamental mode and variable cladding dimensions.....	22
Figure 3-9:	Diagram showing the transition from dielectric rod waveguide to rectangular waveguide.....	22
Figure 3-10:	Simulated attenuation versus loss tangent variation at 14 GHz (a) and 18 GHz (b)	23
Figure 3-11:	Simulated 1 dB and 2 dB cutoff frequency versus cladding width/height for square cross-sections	24
Figure 3-12:	Simulated 1 dB and 2 dB cutoff frequency versus cladding permittivity	25

Figure 3-13: Diagram of the 2-port measurement setup showing the transition from dielectric rod waveguide to rectangular waveguide and the key dimensions (a) and fabricated DRW with cladding (b)	25
Figure 3-14: Measured and simulated S parameters for the Ku band DRW with transitions to RWG without cladding (a) [50], with 10×10 mm ² ABS cladding (b) [50] and with 20×20 mm ² ABS cladding (c).....	26
Figure 3-15: Measured S parameters for the Ku band DRW with transition to RWG without cladding (top) and with ABS cladding (bottom).....	28
Figure 3-16: Measured and simulated S-parameters of the DRW core (a) and with 10 × 10 mm ² ABS cladding (b) for a 35 mm bend DRW	29
Figure 3-17: Simulated and measured attenuation versus radii of curvature of a DRW bend without (a) and with (b) the ABS cladding at 12 GHz and 14 GHz.....	29
Figure 3-18: Attenuation of the DRW without (a) and with (b) ABS cladding due to radiation, due to the dielectric and total attenuation.....	32
Figure 3-19: Attenuation of the DRW due to the transition to RWG and impedance mismatch with and without ABS cladding	32
Figure 3-20: Illustration of solid core DWG (W=0.32mm, H=0.64mm, Lt=4mm, LD=10mm) (a), diagram of the D-band measurement setup (b), and picture of the D-band measurement setup (c)	33
Figure 3-21: Measured and simulated D band S-parameters	34
Figure 4-1: Proposed multilayer dielectric rod waveguide design and dimensions	38
Figure 4-2: Picture of the FDM-fabricated dielectric rod waveguide without the cladding (top) and with the ABS cladding (bottom).....	38
Figure 4-3: Measured and simulated S-parameters for the DRW with transition to WR-62 waveguide ports without cladding (a), and with ABS cladding (b).....	39
Figure 5-1: MSL DRW geometry and key parameters.....	42
Figure 5-2: Measured and simulated S parameters of the MSL DRW of L _m =1.12 mm and L _{gap} =4 mm.....	43
Figure 5-3: Simulated transmission coefficient of the MSL DRW of L _m =1.12 mm and variable L _{gap}	43
Figure 5-4: Simulated S parameters of the MSL DRW of L _{gap} =3 and 5.5 mm	44
Figure 6-1: Proposed multilayer DRA geometry and key dimensions, showing the inner core (top) and multilayer design (bottom)	47
Figure 6-2: Measured and simulated peak gain (a) and reflection coefficient (b-c) of the single and multilayer DRA with different cladding permittivities.....	48
Figure 6-3: Measured and simulated E-plane radiation pattern for the single (top) and multilayer (bottom) DRA with $\epsilon_r = 2.6$ cladding at 12.2 GHz [50]	49
Figure 6-4: Measured and simulated E-plane radiation pattern for the single (top) and multilayer (bottom) DRA with $\epsilon_r = 1.6$ cladding at 17.2 GHz.....	49

Figure 6-5:	Simulated E-Field distribution at 17.2GHz for single (top), and multilayer (bottom) DRA with $\epsilon_r = 2.6$ cladding	50
Figure 6-6:	Simulated d far field 3D radiation pattern for the single (a) and multilayer (b) DRA.....	51
Figure 6-7:	Simulated gain vs frequency for different length increments of the body gradient in a single layer DRA	51
Figure 6-8:	Simulated gain vs frequency for different length increments of the body gradient in a single and multilayer DRA	52
Figure 6-9:	Simulated end-fire gain versus loss tangent variation at 14 GHz (a) and 18 GHz (b).....	53
Figure 6-10:	Simulated gain vs frequency for different cladding permittivities	53
Figure 6-11:	Simulated gain vs cladding to core permittivity ratio for different frequencies	54
Figure 7-1:	Antenna physical geometry and dimensions (a), and fabricated prototype (b).....	56
Figure 7-2:	Measured and simulated gain vs frequency (top) and return loss (bottom) of the multilayer DRA	57
Figure 7-3:	Measured and simulated E-plane radiation pattern without and with ABS cladding for the dielectric rod antenna at 35.6 GHz	58
Figure 8-1:	Antenna physical geometry and key parameters	59
Figure 8-2:	Measured and simulated gain vs frequency for the dielectric rod antenna with and without metal strips of $L_m=2.25$ mm	60
Figure 8-3:	Simulated gain vs frequency for the DRA with metal strips of variable widths.....	61
Figure 8-4:	Measured and simulated E-plane radiation pattern without and with metal strips for the dielectric rod antenna at 13 GHz.....	61
Figure 9-1:	Proposed transition geometry and key parameters	64
Figure 9-2:	Electric field magnitude in the proposed transition and DRW at 20 GHz.....	65
Figure 9-3:	Measured and simulated S parameters of the back to back transition with a 55 mm DRW (a) and MDRW (b).....	66
Figure 9-4:	Proposed transition thru connection	67
Figure 9-5:	Measured and simulated S parameters of the proposed transition thru connection.....	67
Figure 9-6:	Simulated transmission coefficient of the proposed back to back transition under different material loss conditions.....	68
Figure 9-7:	DRA geometry and key dimensions (a), proposed transition with a single (b) and with a multilayer DRA (c).....	69
Figure 9-8:	Measured and simulated peak gain (a) and reflection coefficient (b-c) of the DRA and MDRA.....	69
Figure 9-9:	Measured and simulated E-plane radiation pattern for the single DRA (a) and multilayer DRA (b) at 16.5 GHz	70
Figure 9-10:	Simulated E-Field distribution at 20 GHz for single (top), and multilayer (bottom) DRA	71

ABSTRACT

This dissertation presents first a comprehensive study of the design and performance of a multilayer dielectric rod waveguide (DRW) with rectangular cross-section. The design is comprised of a high permittivity core encased by a low permittivity cladding. A modal analysis of the multilayer DRW with a 2:1 core aspect ratio is presented and a mathematical model is proposed to characterize the fundamental mode cutoff frequency in terms of the core and cladding permittivity and the core dimensions. The explicit nature of the model is useful for design and it offers an excellent match to the full-wave EM simulation data. The multilayer DRW performance is measured for the extended Ku band (10-18 GHz) considering straight and bent waveguides with different radius of curvature. The multilayer configuration shows a 16.7% and 24% reduction of the 1 dB cutoff frequency for a $10 \times 10 \text{ mm}^2$ and $20 \times 20 \text{ mm}^2$ cladding area, respectively, when compared to a single layer design of the same core dimensions. It is also demonstrated that the multilayer DRW shows reduced radiation at the lower end of the band when compared to its single layer counterpart, for different radius of curvature bends. Specifically, the multilayer DRW shows an insertion loss improvement of 9.5 dB at 12 GHz for a 35 mm radii of curvature bend.

In a second chapter, a proposed multilayer DRW designed for the extended Ku band (10-18 GHz) is fully developed and fabricated by using additive manufacturing technologies, particularly fused deposition modeling (FDM). The multilayer DRW is formed by a medium- k dielectric core printed with a custom-made ceramic composite and a low permittivity ABS cladding. Both materials are compatible with FDM. Device performance is measured with and without the presence of the low permittivity cladding. The insertion loss of the multi-layer DRW is less than 0.012 dB/mm and the attenuation due to each waveguide feed transition falls within 0.29 to 0.98 dB in the entire frequency range. Additionally, the presence of the cladding extends the 1 dB cut-off frequency by 2 GHz, thus improving the 1dB operational bandwidth by 50 %.

The effect of a low permittivity cladding used in a multilayer end-fire dielectric rod antenna (DRA) design is studied in terms of return loss, gain and half power beamwidth in the extended Ku band (10-18 GHz). Gain improvement ranging from 4 dB to 7 dB is achieved using cladding permittivities between 1.6 and 2.6 when compared to a single layer design of the same length. For example, a cladding of $\epsilon_r = 1.6$ leads to a peak gain increment of 4.5 dB at 18 GHz and a 20 degree HPBW reduction compared to the non-cladded rod. It is also demonstrated that this

design has the same maximum gain as a non-cladded design that is 1.8 times longer. The cladding permittivity in the multilayer DRA can be adjusted to achieve peak performance at different frequencies within the band, while providing gain enhancement in the entire band without reducing the bandwidth.

A multilayer dielectric rod antenna (DRA) design is proposed for mm-wave applications. The multilayer DRA is formed by a medium permittivity dielectric rod core encased by a low permittivity cladding to increase the peak gain. The antenna is fabricated using fused deposition modeling (FDM) of two thermoplastics; a ceramic composite material for the core and acrylonitrile butadiene styrene (ABS) for the cladding. The antenna performance is measured from 30 to 40 GHz and the results are validated using numerical simulations. The peak gain of the multilayer antenna is over 22 dBi for the entire frequency range. The effect of the cladding on the antenna performance is to increase the gain by 3-8.5 dB, with a reduction in the half power beamwidth of 22 degrees at the center frequency. The multilayer DRA design offers high gain performance, scalability to other frequency ranges and low-cost fabrication.

A metal grating pattern was implemented on a dielectric rod antenna (DRA) with rectangular cross-section to increase the antenna gain in a narrowband. The DRA is formed by a high permittivity core that is cut into shape using laser machining. The metal strip loading is added using micro-dispensing of silver paste. The proposed design was characterized from 12.4 to 18 GHz, a peak gain increment of 2 dB was measured at 13 GHz and a half power beamwidth (HPBW) reduction of 12 degrees was obtained with metal strip length of $0.27 \lambda_g$. An improvement that yields ~ 50% reduction in body gradient size when compared to a non-loaded antenna. Simulated data shows the inverse relationship between the end fire peak gain frequency and the strip length.

CHAPTER 1: INTRODUCTION

1.1. Introduction

Adapted versions of common planar waveguides such as microstrip and coplanar waveguides are often integrated into microwave applications; but their characteristics lead to high ohmic losses when implemented at millimeter wave and THz frequencies [1]. Low losses in the THz range, on the other hand, have been achieved by dielectric waveguides with either hollow or porous cores [2], but their delicate geometry is not generally considered attractive from a system integration standpoint. On the contrary, other designs with rectangular cross sections such as dielectric rod waveguides and dielectric ribbons have already been implemented in multilayer PCBs, exhibiting broad band performance in the mm-wave range [1].

In this work dielectric rod waveguides and dielectric end-fire antennas are studied and their performance is enhanced at the Ku and K bands using dielectric loading techniques. The proposed designs have a rectangular cross section that offers the possibility of integration with mm-wave systems and it can be easily scaled to operate at other frequency ranges. Dielectric rod waveguides and traveling wave antennas are an attractive option for many applications in the upper microwave and mm-wave frequency range due to some key advantages including small size, high gain, broadband performance, and low loss depending on the constituent materials [3]. Dielectric devices typically have easier, less expensive fabrication process and more tolerance for geometric discontinuities as compared to metal devices.

Dielectric rod antennas (DRAs) represent a viable option for ultra-wideband (UWB) end-fire systems when compared to conventional aperture horn antennas or tapered slot radiators. DRAs can often achieve a performance similar to these alternative approaches accompanied not only with lighter weight, reduced volume and small cross-section, but also with low mutual coupling between single elements in array configurations [4]. These characteristics continue to generate interest in a wide variety of fields and applications such as satellite communications [5], radar systems [6], chip-to-chip communications [7], and millimeter-wave imaging [8, 9].

It has been demonstrated that DRA's performance can be enhanced with several methods that somehow modify the structure of the single element. These methods include altering the physical geometry of the antenna in

order to modify its physical shape [9], or increasing the number of elements to create end-fire array configurations[10]. It is also common to feed the DRA with tapered slot antennas or to implement the rod itself as a feed for reflector antennas, such as horns or parabolic dishes [11, 12]. More recent studies include substrate integrated waveguide feed networks and embedded multilayer structures to avoid excitation of high-order modes [4, 13]. Certainly, all of the above mentioned methods will need a re-design stage if an improvement in performance is needed once the antenna is operating.

Different dielectric loading studies have been performed previously to vary the cut-off frequencies of rectangular waveguides (RWG) [14], and also as a way to modify the electrical length of traveling wave antennas such as Vivaldi tapered slot antennas and waveguide fed aperture radiators with the purpose of gain and half power beamwidth improvements [15, 16] . Dielectric loading techniques have also been used for antenna miniaturization; the addition of dielectric materials is used to increase the effective permittivity causing a reduction of the wave propagation velocity and a reduction of the guided wavelength, allowing the required antenna dimensions to be decreased. Reduction of the cut-off frequency, increased antenna peak gain and miniaturization are just some of the advantages of dielectric loading techniques. Nevertheless, the addition of dielectric materials might require in some cases a modification of the antenna design [15]. Also, it might increase the fabrication cost and complexity as reported for the multi-filar dielectric loaded antennas [17].

This work investigates the use of a non-invasive dielectric cladding that can be directly incorporated into a dielectric waveguide or antenna structure to improve the performance without the need for redesign. The cladding can be fabricated using digital additive manufacturing (AM), specifically fused deposition modeling. The AM approach is especially useful in this study as it provides a low cost means of experimentally validating different designs with a rapid turn-around time. Similar techniques have been used with great success in the fabrication of other RF/microwave components [18, 19].

Additive manufacturing (AM), has proven to be a good manufacturing alternative for the integration and fabrication of RF/microwave and even mm-wave devices [18], The 3-D printing technology has awakened a continuous and growing interest among a diverse range of research, industrial, commercial and educational institutions. This in large part thanks to the possibility of rapid prototyping of custom design parts for a low to mid-volume production. Fused deposition modeling (FDM) in particular has become one of the popular low-cost fabrication techniques in recent years, since it has an advantage of efficient management of printing resources (e.g.

minimum material waste) through a controlled layer by layer deposition process. FDM can employ common thermoplastics such as acrylonitrile butadiene styrene (ABS) or polylactic acid (PLA), or novel engineered composite materials [20]. Due to the low conductivity and high surface roughness for printed silver pastes, design of dielectric waveguide structures is preferred for signal transmission at mm-wave frequencies and beyond. For micro-dispensed CB028 silver paste, a lower than bulk conductivity of $3.94e^6$ S/m [18] and a surface roughness of $3.68\mu\text{m}$ are expected, with significant variations of both variables across the surface [21].

In a second part of this work, the multilayer dielectric rod waveguide and end-fire dielectric rod antenna designs proposed are adapted to be completely fabricated using additive manufacturing (AM), specifically fused deposition modeling (FDM). A ceramic composite that is compatible with FDM and has a higher dielectric constant than commercially-available 3D printing materials was used for the core [22]. A low permittivity ABS cladding is included to improve the waveguide bandwidth and to enhance the antenna gain performance in the entire frequency range.

A metal grating pattern was implemented to the proposed dielectric rod waveguide and dielectric end-fire antenna. In the case of the DRW, the corrugated metal layer is included to create a band stop filter embedded in the waveguide core. The band stop center frequency can be adjusted by changing the periodicity of the metal strips and the rejection level can be varied with the number of filter stages. Band stop filter in dielectric rod waveguides have been proposed in the literature by introducing alternating layers of high and low permittivity materials [23]. For the DRA the metal grating pattern periodicity allows to vary the antenna peak gain frequency, this lead to a gain enhancement in a narrow bandwidth.

In a final part of this work, a broadband transition for dielectric rod waveguides to planar transmission line is proposed and characterized for the Ku band. The transition is used to characterize single and multilayer dielectric rod waveguides and dielectric rod antennas. The performance of the proposed transition is compared against a standard transition to rectangular waveguide.

1.2. Contributions

The main objective of the following research is based on a comprehensive study and system characterization that will provide improvements in the state of art of dielectric rod waveguides, dielectric end-fire antennas and interconnects using additive manufacturing techniques.

Some specific contributions include:

1. Implementation of additive manufactured low permittivity cladding to improve the performance of dielectric rod waveguides (DRW) and end-fire dielectric rod antennas (DRA).
2. Comprehensive study of the low permittivity cladding effect on DRW to provide an explicit analytical model of the multilayer DRW cut-off frequency.
3. Design and characterization of fully 3D printed multilayer Ku band dielectric rod waveguide with enhanced bandwidth using novel FDM composite material.
4. Advancement in state of the art of additive manufactured dielectric end fire antennas
5. Design and implementation of novel low loss DRW transition to microstrip and integration with passive systems.
6. Design and implementation of metal strip loaded DRW band stop filter.
7. Corrugated edge integration for side lobe reduction and front to back ratio improvement in dielectric end-fire antennas.

1.3. Dissertation Outline

This dissertation is comprised of 9 chapters organized as follows; a literature review of dielectric rod waveguides, dielectric end fire antennas and transition to planar transmission lines is presented in chapter II. A comprehensive study of dielectric rod waveguides and the effect of the cladding in the DRW performance is presented in chapter III. The multilayer dielectric rod waveguide presented in chapter III is adjusted to be completely fabricated using FDM and the measured results are analyzed in chapter IV. Chapter V explains the design and characterization of a metal strip loaded DRW filter for the Ku band. A dielectric end-fire antenna with enhanced gain is proposed to operate at the Ku band, the design procedure and measured performance is presented in chapter VI. A fully 3D printed version of the multilayer dielectric end fire antenna is designed and implemented at the Ka band, the performance is discussed in chapter VII. Chapter VIII presents the design and characterization of a metal strip loaded dielectric rod antenna with a narrowband gain enhancement. Finally, Chapter IX proposed a broadband transition from dielectric rod waveguides and dielectric rod antennas to microstrip for the Ku band.

CHAPTER 2: BACKGROUND AND LITERATURE REVIEW

2.1. Introduction

The continuous and systematic push of the Internet of Things (IoT) and 5G wireless protocols will require millimeter wave systems that offer wide channel bandwidth and high power handling for successful data transmission to end users [24]. The implementation of low loss waveguide structures at these frequencies is thus of ever growing importance. Planar metal-based transmission lines, such as microstrip and CPW that are successfully used at microwave frequencies, exhibit high losses in the mm-wave range [2]. This characteristic is due to the increased ohmic loss and surface roughness of the conductive layers, along with the dielectric losses. Dielectric waveguides naturally eliminate conductor losses and have been successfully implemented in the mm-wave and THz regimes. High performance dielectric waveguides are used for a wide variety of applications such as biomedical imaging [25], spectroscopy [26] and communication systems [27].

Dielectric waveguides are usually divided into 3 categories: hollow core, porous core and solid core [26]. Typically, the hollow core waveguides exhibit the lowest losses since most of the electromagnetic power propagates through the hollow center of the guide [26]. But in order to allow most of the electromagnetic power to propagate in the core, the core dimension has to be much larger than the wavelength and this can lead to narrow operational bandwidths or multimode propagation [26, 28]. Porous core waveguides are created by introducing a certain distribution of sub-wavelength air holes into the core of the dielectric structure. Some very innovative geometric designs have been proposed in order to achieve low transmission loss and high mode confinement [29-32]. The main disadvantage of these designs is typically the fabrication complexity that depends on the distribution, shape and size of the air holes [26]. Among dielectric waveguides, the solid core designs introduce the higher dielectric absorption losses but their simplified fabrication, wide bandwidths and the possibility of planar implementation are attractive features. Some solid core waveguide designs such DRWs with rectangular cross-sections and as dielectric ribbons are highly compatible with multilayered PCBs [23] and on-wafer integration [33].

2.2. Millimeter-Wave and THz Dielectric Waveguides

The selection of a waveguide structure to be used in a particular application is usually determined by considering three main factors: the frequency band of operation, the amount of power to be transferred and the transmission losses that the system can tolerate [34].

The design of effective waveguides for the mm-wave frequency range is not as simple as scale down the dimensions of the designs used at RF and microwave. Transmission lines such as microstrip and CPW that have a good performance at microwave frequencies also present high ohmic losses in the mm-wave range and above. Changes in these transmission lines designs has to be implemented in order to reduce the losses at higher frequencies, for example an air-cavity inverted microstrip line has been optimized from microwave to millimeter wave and have reported a maximum attenuation of 0.08 dB/mm up to 100 GHz in a simulation environment [35]. Other efforts has been dedicated to reduce the propagation losses by using low loss materials. A recently published characterization of a microstrip on liquid crystal polymer has shown a very good performance on the D band with a maximum attenuation of 0.331 dB/mm at 170 GHz [36].

From the 3D digital manufacturing perspective, the resolution of the current technology makes possible the fabrication of a wide variety of waveguide designs for the mm-wave frequencies. The typical dimensions of mm-wave waveguides are within the 3D printing capabilities. Equipment with multiple nozzles and the availability of different materials such as ceramic, metal, plastic and other polymers also make possible the fabrication of multiple layer waveguides [19]. The reduced conductivity of the silver paste and surface roughness issues make dielectric waveguide or “metal free” waveguide designs a very attractive option.

A lot of effort have been devoted to dielectric waveguide research and have made possible to reduce the attenuation level from 100 dB/m to 1 dB/m in the THz regime [2]. A comprehensive review of the main dielectric waveguide designs is presented in this section.

In general terms, dielectric waveguides have been classified into 3 major categories: solid core, hollow core and porous core:

2.2.1. Hollow Core Dielectric Waveguides

Hollow core is considered any waveguide in which most of the electromagnetic power propagates through the air core and just a small fraction in the cladding, despite the cladding material or geometry.

The main advantage of hollow core waveguides is that material absorption is negligible since most of the electric field is confined in the air core. On the other hand, the low loss and low dispersion characteristics are only achieved in a small frequency range. To allow most of the electromagnetic power propagates in the core, the core dimension has to be much larger than the wavelength which causes multimode operation. Higher-order modes can be eliminated by reducing the core size, since it increments the cut-off frequency of the higher order modes but this increases the attenuation of the fundamental mode. By reducing the core size a larger fraction of electromagnetic power will now be propagating through a different material (cladding) which can lead to higher dispersion [2, 37].

The diameter of this waveguides at mm-wave frequencies is typically about a few millimeters. These structures are normally rigid and not very practical for circuit integration.

Fig 2-1 presents three variations of hollow core dielectric waveguides for THz frequencies; a single clad waveguide or dielectric tube [2], dielectric lined hollow cylindrical metallic waveguide or hybrid cladding waveguide [38] and concentric cylindrically periodic Bragg fiber [39]. The diameter of the core varies from 1 mm for the Bragg fiber to 8 mm for the single clad. Attenuation values are as low as 1 dB/m as reported for the dielectric lined waveguide [38].

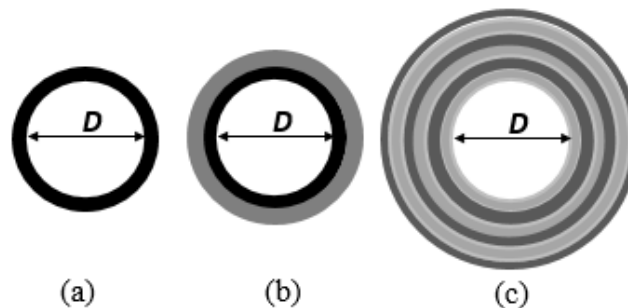


Figure 2-1: Illustration of some hollow core dielectric waveguides configurations. (a) Single clad dielectric waveguide (b) dielectric lined hollow cylindrical metallic waveguide (c) Concentric cylindrically periodic fiber with different permittivity materials in the cladding.

2.2.2. Porous Core Dielectric Waveguides

Porous core waveguides are created by introducing a certain distribution of sub-wavelength air holes in the core of the structure. Typically, this type of waveguides also presents lower material loss compared to the solid core since less material is placed in the core.

A good porous core waveguide design will increase the power confinement in the air holes, which is very important in bends and discontinuities. The overall losses will depend on the material used, the size of the holes and

the percentage of porosity that can be achieved which is the fraction of air holes relative to the total core area. Creative geometrical shapes has been proposed in the literature for the porous core to improve the performance of these waveguides but complicated geometries represent a fabrication challenge due to the small dimensions at such high frequencies [31, 40].

Fig. 2-2 presents an illustration of three porous core dielectric waveguide designs: hexagonal array, hexagonal and spider web polymer porous fibers. The illustrated designs were fabricated using Polymethyl methacrylate (PMMA) with 57% and 65% porosity. The air holes sizes vary between 200 and 600 μm [31, 32].

As mentioned, both the design and the material properties play a critical role in the porous waveguide. A low loss flexible porous waveguide fabricated in cyclic olefin copolymer (COC) Topas has reported an attenuation below 0.1 dB/cm measured at 0.6 THz. The design is similar to the hexagonal array in Fig. 2-2(a) with a 6 mm outer diameter, 250 μm hole diameter and 560 μm pitch. The same work has also shown that the resulting attenuation using Topas can be 10 times lower than the one using PMMA [41].

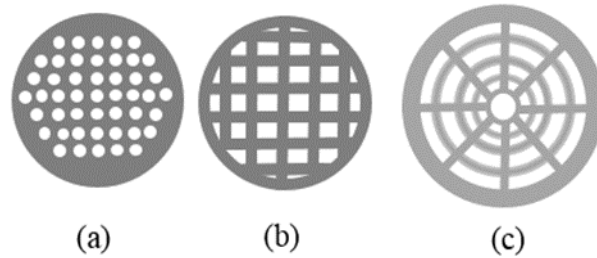


Figure 2-2: Illustration of some porous dielectric waveguides configurations. (a) Hexagonal array (b) rectangular (c) spider-web air-hole porous fiber [31, 32].

2.2.3. Solid Core Dielectric Waveguides

In the solid core waveguide as the name implies the electric field is guided in a dielectric substrate. Solid core dielectric waveguides can be typically classified according to the cross sectional geometry into circular, elliptical and rectangular dielectric waveguides. For solid-core and porous-core waveguides the guiding mechanism is total internal reflection if the dielectric constant of the core is greater than the dielectric constant of the cladding. The guiding mechanism is based on photonic bandgaps when the dielectric constant of the core is smaller than the dielectric constant of the cladding [34, 42].

The only dielectric material with negligible absorption at high frequencies is air, this is the main reason why hollow or porous core dielectric waveguide have typically the lowest attenuation values. In general terms solid core

waveguides are easier to fabricate but the overall losses are determined by the dielectric absorption which can be frequency dependent [34].

Two options can be implemented to decrease the loss value of a solid-core waveguide. The first one is using the lower loss dielectric materials available so the minimum loss will be limited to the bulk material loss. The second option is reducing the waveguide core dimension so a greater amount of the electric field will be propagating in the air. The disadvantage of this approach is that when the modes less confined to the waveguide it increase the sensitivity to external perturbations and increase the radiation losses on bents and discontinuities [34, 43].

Some common variations of solid core dielectric waveguides are illustrated in Fig. 2-3. A dielectric ribbon waveguide created with polymer-ceramic nanocomposites have reported an attenuation of 0.001dB/mm at 200 GHz, which is 6 times lower than the one from a microstrip at the same frequency. These values were derived from simulated data in HFSS [44].

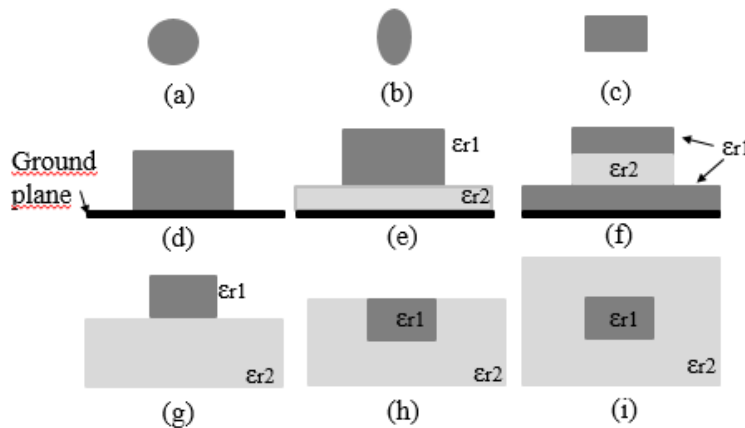


Figure 2-3: Illustration of solid core dielectric waveguides configurations. (a) Circular (b) elliptical (c) rectangular (d) mirror (e) isolated mirror (f) layered ribbon (g) strip loaded (h) embedded strip (i) buried channel dielectric waveguide [45].

It is worth to mention the difference in three dielectric waveguide structures since often can lead to confusion. Fig. 2-4 present a dielectric slab waveguide, this is a 2-dimensional waveguide since the width is always consider infinite. A ribbon waveguide is shown in Fig. 2-4(b), this is a multilayers dielectric waveguide where the width is considered much greater than the core height. A dielectric rod waveguide without cladding is presented in Fig. 2-4(c), in this structure the core height and width have comparable dimensions.

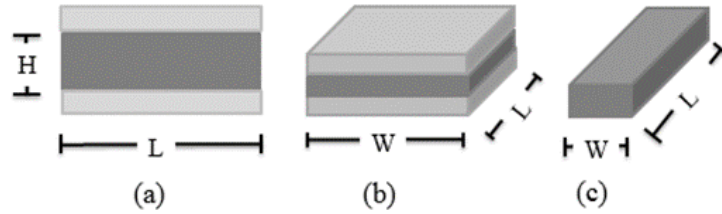


Figure 2-4: Illustration of dielectric slab (a), ribbon (b) and dielectric rod (c) waveguides.

The only dielectric waveguide geometries that possess exact analytic solutions to guided wave problems are the slab, circular cylinder and the elliptical cylinder waveguides. There is no exact analytic solution to the propagation characteristics of a wave traveling along a rectangular dielectric guide or other cross-sectional geometries. Some approximation methods have been proposed in the literature to address the issue [42].

2.2.4. Transition for Dielectric Rod Waveguides to Planar Transmission Lines

The increasing propagation loss of planar metal-based transmission lines with frequency due to metal skin depth and the challenge of achieving single mode operation makes dielectric waveguides an attractive option for guiding signals at mm-wave and well into the THz range for chip-to chip and module to module interconnects [46]. One of the main challenges to make dielectric waveguides a viable option for board level interconnect is the development of effective low loss planar feeds compatible with standard PCB processes [46]. It is part of the scope of this dissertation the design and characterization of a low loss broadband dielectric rod waveguide transition to planar transmission lines.

One of the most straightforward transitions between dielectric rod waveguides and microstrip consist of tapering the DRW ends and directly placing the taper section on top of the microstrip line. The tapered section gradually matches the impedance to the 50Ω microstrip line. A disadvantage that might be associated with this type of transition is the higher radiation loss which can lead to a bandwidth reduction.

Fig. 2-5 (left) illustrate this microstrip-DRW transition designed for the G band [47]. The transition was fabricated using Quartz for the microstrip substrate, a Ti/Au thin film for the conductive layer and high resistivity silicon for the DRW. The reported minimum insertion loss for a back to back transition and a 10 mm DRW is 1.55 dB from simulated data and 4.9 dB from measured data. Fig. 2-5 shows the simulated and measured S parameters of the transition for DRW of two different lengths. Since the attenuation of the 10 and 20 mm DRWs is comparable, the results indicate that the majority of the loss comes from the transition.

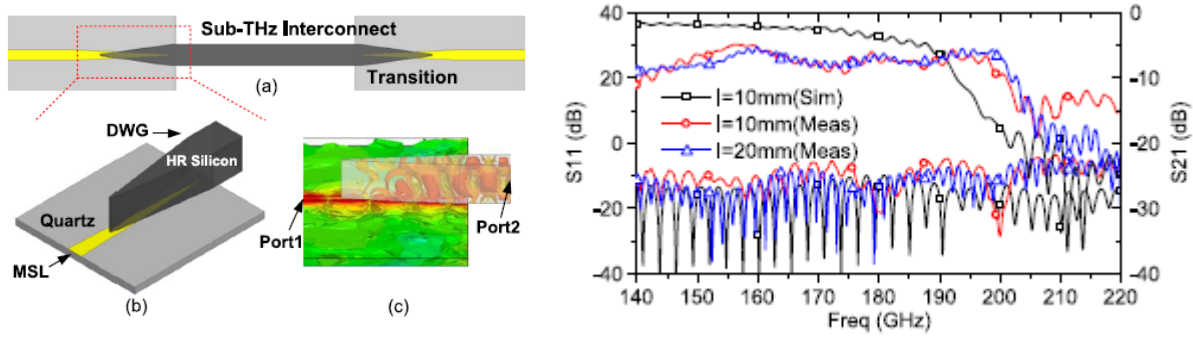


Figure 2-5: Dielectric rod waveguide and microstrip line interconnect design for the G band [47].

A similar transition between a dielectric rod waveguide and a microstrip line has been designed from 60 to 90 GHz [48]. As illustrated in Fig. 2-6, the transition is made by tapering the dielectric rod waveguide and adding a top metal layer to the dielectric core. Transmission losses above 3.5 dB and return losses above 8 dB were reported from simulated data of a back to back structure from 70-83 GHz.

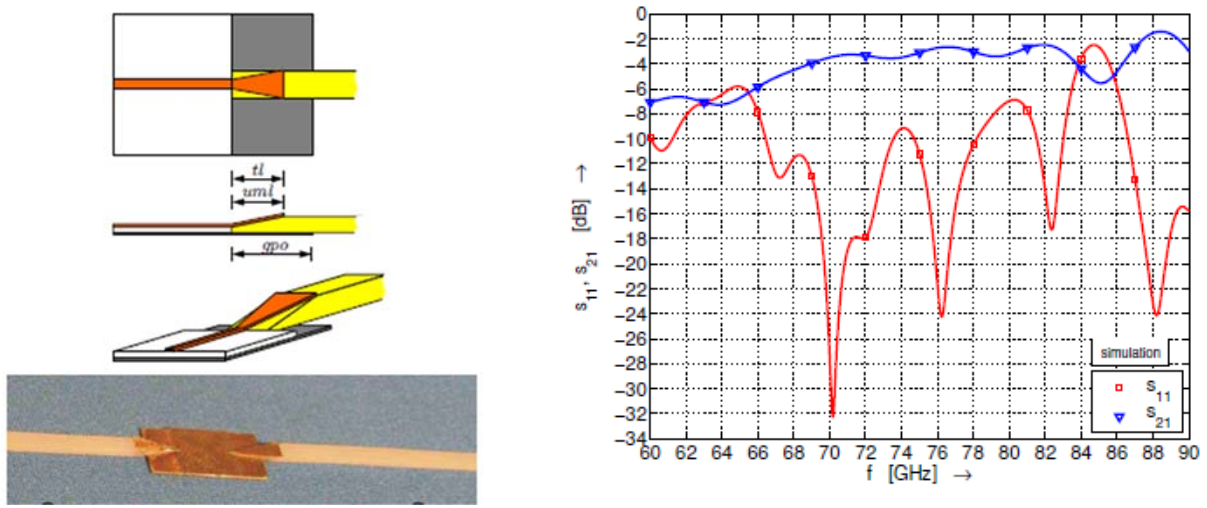


Figure 2-6: Transition between rectangular dielectric rod waveguide and microstrip design (left) and simulated data (right) from 60 to 90 GHz [48].

Recently a transition for dielectric rod waveguide to CPW using an intermediate metallic horn has been proposed [49]. The transition is depicted on Fig. 2-7 and it shows a tapered ridge metallic horn as an intermediate transition between CPW and a dielectric waveguide with rectangular cross section. The metal horn is included to improve the coupling between the waveguides. The transition was designed and characterized for the D band and it was fabricated using polystyrene for the DRW and Rogers RO5880 for the planar substrate. Fig. 2-7 presents the

measured S parameters showing a minimum attenuation of 5 dB for a back to back transition with an 8 cm long DRW. A minimum return loss of 5 dB at 125 GHz and 145 GHz reduces the transition bandwidth significantly.

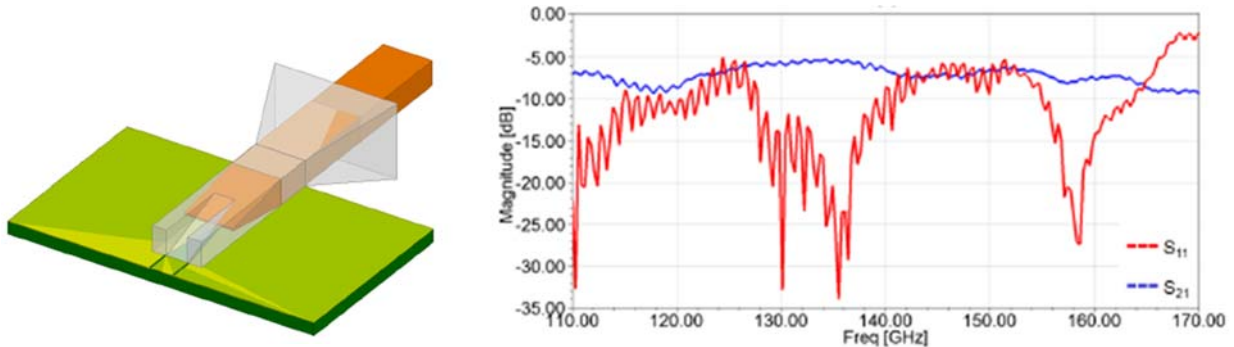


Figure 2-7: Transition for dielectric rod waveguide to CPW at D band [49].

Another novel transition has been published recently for PCB integration of dielectric ribbon waveguides [46]. The design is illustrated in Fig. 2-8 (left) and the measured S parameters at D band are shown in Fig. 2-8 (right). The dielectric ribbon is transitioned to CPW using a Vivaldi type launcher. Measurements were done using GSG on-wafer probes via an intermediate planar balun. The measured attenuation at 140 GHz for a back to back transition and an 8.5 cm dielectric waveguide was reported to be 10 dB, where 2 dB are attributed to the losses from the dielectric waveguide and 8 dB to the losses from the transition.

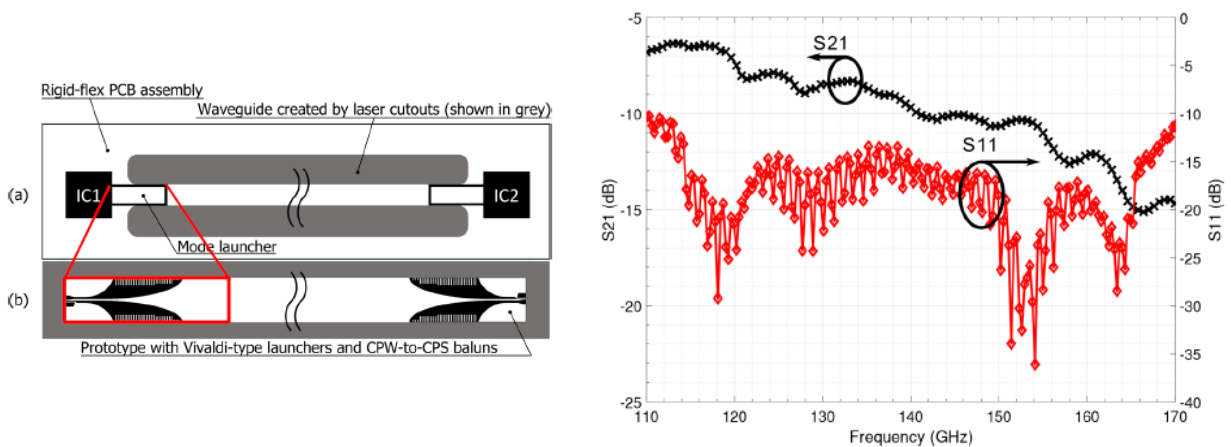


Figure 2-8: PCB-embedding scheme for dielectric ribbon waveguide at D band [46].

CHAPTER 3: ANALYTICAL STUDY OF MULTILAYER DIELECTRIC ROD WAVEGUIDES

3.1. Introduction

This chapter investigates the design and performance of multilayer dielectric rod waveguides with rectangular cross-section. The proposed design is formed by a high permittivity rod surrounded by a low permittivity cladding. The low permittivity cladding is used to enhance the waveguide performance by increasing the bandwidth and reducing the losses in bends. This additional dielectric layer does not increase the waveguide insertion loss since most of the electric field propagates in the waveguide core and it also can be specifically selected to increase the field confinement. The cladding also reduces the possible electromagnetic interactions between waveguide core and adjacent structures since it encompasses the totality of the electric field. As shown in [50], this characteristic can be used to prevent degradation of the waveguide performance due to lossy substrates or neighboring waveguides.

In this work, the cladding is fabricated using a digital additive manufacturing (AM) technology called fused deposition modeling (FDM), which has been proven to perform efficiently up through mm-wave frequencies [18, 19]. With FDM, structures are formed using a controlled layer-by-layer deposition of a thermoplastic filament. The layer height depends on the printing nozzle size and typically can range from 300 down to 25 μm . Similar techniques have been used with great success in the fabrication of other RF/microwave components [18, 19]. The AM approach is especially useful in this study as it provides a low cost means of experimentally validating different designs with a rapid turn-around time.

In addition to experimental results, this chapter presents a closed-form model for multilayer DRW that is useful for design purposes. It is well known that there is no analytical solution to the wave propagation problem in a rectangular rod, which can make the analysis of rectangular DRWs very challenging. Several approximation methods have been proposed in the literature to address this issue; two of the most popular were proposed by Marcatili [51] and Goell [52]. Marcatili's method is derived in the Cartesian coordinate system by considering the rod as a superposition of two dielectric slab waveguides and assuming well confined modes. Goell solves the problem using a cylindrical coordinate system and proposes a solution based on a modified Bessel function multiplied by trigonometric functions. Herein, an explicit analytical model for the waveguide cutoff frequency is proposed. The model predicts

the appropriate waveguide dimensions for a given cutoff frequency, based on the material properties and operational frequency.

This chapter is organized as follows: section 3.3 presents a study of the multilayer DRW design guidelines and modal analysis. Section 3.4 proposes an explicit analytical model of the multilayer DRW cutoff frequency as a function of the core dimension and material properties of the core and cladding. The model is derived for multilayer DRW with rectangular cross-section and 2:1 aspect ratio. Section 3.5 presents a study of the cladding effect in the multilayer DRW performance and section 3.6 shows the characterization of the multilayer DRW for the extended Ku band that was first described in [50]. In this section, measured data of different straight and bent waveguides are presented and a breakdown of the losses due to the dielectric material, transition and radiation is presented.

3.2. Multilayer Dielectric Rod Waveguide (DRW)

3.2.1. Design Considerations

The proposed multilayer DRW design is comprised of a high dielectric constant core surrounded by a low dielectric constant cladding [50]. The core is a dielectric rod waveguide with rectangular cross-section as illustrated in Fig. 3-1. In this work, the width of the core is optimized for the Ku band, based on numerical simulation data obtained using Ansys (HFSS). As a starting point for the optimization, the width of the core can be approximated to the maximum thickness for a dielectric slab waveguide with single mode operation [45]:

$$\text{Slab Thickness} < \frac{\lambda_0}{2} \frac{1}{\sqrt{n_{\text{core}}^2 - n_{\text{clad}}^2}} \quad (3.1)$$

where n_{core} and n_{clad} are the refractive indexes of the core and cladding, respectively.

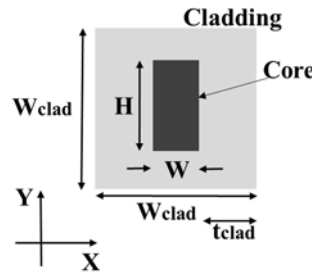


Figure 3-1: Multilayer dielectric rod waveguide cross-section and key parameters.

In the DRW, the guiding mechanism is total internal reflection and the modes it supports are hybrid and polarized in the x or y directions assuming propagation in the z direction. The modes belong to either the E_{nm}^y or E_{nm}^x families, where n and m are the number of maxima in the x and y directions, respectively, and the superscript x

or y indicates the direction of the field polarization [51]. If the core refractive index is lower than that of the cladding, the guiding no longer occurs by total internal reflection but by photonic bandgap.

The core cross-section and the refractive indexes of the core and cladding determine the DRW mode cutoff frequencies. If n_{core} and n_{clad} are very close in value, the largest field component is normal to the propagation direction or TEM-like [51]. On the other hand, it has been demonstrated that a small difference between the refraction indexes that satisfy (3.2) will cause the modes E_{mn}^y and E_{mn}^x to be degenerate regardless of the core geometry. A larger difference between the refractive indexes of the core and cladding will break field degeneracies depending on the core aspect ratio [51]

$$\frac{1}{n_{core}}(n_{core} - n_{clad}) \ll 1 \quad (3.2)$$

Considering a certain field polarization, a square core cross-section provides the largest single mode operation bandwidth or the largest difference between the first two cutoff frequencies for the E_{11} and E_{21} modes [28, 51]. When x and y field polarizations are present in the square dielectric waveguide, due to symmetry, all the modes are degenerate even for larger differences between n_{core} and n_{clad} . In this case, a core aspect ratio different from 1:1 can break the field degeneracies, but as one dimension increases over the other the single mode operation bandwidth reduces [28, 51]. As previously mentioned, the cladding refractive index affects the mode cutoff frequencies. For a certain n_{core} , increasing the value of n_{clad} decreases the higher order mode cutoff frequencies as the effective core size increases. The dielectric cladding can be formed by materials with different refractive indexes in each direction, but there are advantages to using a symmetric DRW over an asymmetric design in terms of cross-section dimensions and guiding properties [51]. The cladding effect on the DRW performance will be discussed in more detail in section II B.

Unlike metal waveguides, modes in dielectric rod waveguides extend outside the waveguide geometry. The rod geometry, material properties and frequency determine the field confinement inside the waveguide core. The dielectric waveguide normalized propagation constant is defined as

$$P^2 = \frac{(K_z/K_{clad})^2 - 1}{(K_{core}/K_{clad}) - 1}, \quad (3.3)$$

where K_z is the axial propagation constant, $K_{core} = \omega(\mu_0 \epsilon_{core})^{1/2}$ and $K_{clad} = \omega(\mu_0 \epsilon_{clad})^{1/2}$. The normalized propagation constant can vary for guided modes from 0, when the mode starts propagating and $K_z = K_{clad}$, to 1, when the mode is completely confined inside the core and $K_z = K_{core}$.

Fig. 3-2 illustrates the DRW fundamental mode field distribution for different permittivity conditions; the normalized propagation constant is used in each case to quantify the field confinement. For these data, a DRW with rectangular cross-section and 2:1 aspect ratio is considered and the fields are presented at 14 GHz in all cases. Fig. 3-2(a) and 3-2(b) show a waveguide core of 4.5 mm x 9 mm cross-section with permittivities of 4.85 and 10.2, respectively, and an air cladding. Increasing the core permittivity decreases the waveguide cutoff frequency and increases the field confinement, similar to a dielectric slab waveguide. In this particular example the fundamental mode cutoff frequency decreases from 7 to 5.59 GHz and the normalized propagation constant P^2 increases from 0.27 to 0.57 at 14 GHz.

Increasing the core permittivity can be used to miniaturize the core dimension. Fig. 3-2(a) and 3-2(c) illustrate two DRWs with the same cutoff frequency of 7 GHz, with permittivities of 4.82 and 10.2, respectively, and air cladding. It is shown that the high permittivity core width is reduced by 1 mm leading to 39.5% area reduction. A mathematical relationship between the cutoff frequency, the core permittivity and core width is proposed in section 3.4.

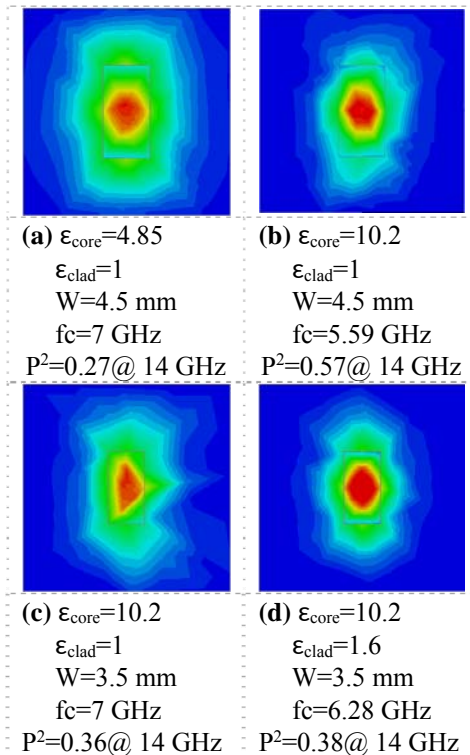


Figure 3-2: Electric field magnitude of the fundamental mode for different core and cladding permittivity at 14 GHz.

A dielectric cladding can be used to decrease the waveguide cutoff frequency and it could be selected to improve the field confinement. Fig. 3-2(c) and 3-2(d) show the same high permittivity core surrounded by air and by an infinite 1.6 permittivity cladding, respectively. It is shown that the cladding addition decreases the cutoff frequency by 0.72 GHz and there is an increase in the field confinement according to (3.3).

In this work, a rectangular cross-section with a height to width ratio of 2:1 is used to maintain single polarization operation [51, 52] and to avoid field degeneracies. The materials used for simulation and fabrication of the high permittivity core and the cladding are Rogers RO3010 ($\epsilon_r=10.2$ and loss tangent=0.0035 @ 9 GHz) and acrylonitrile butadiene styrene (ABS) ($\epsilon_r=2.6$ and loss tangent=0.0052 @ 9 GHz), respectively. The DRW was optimized for the Ku band and the resulting core dimensions are $W=2.5$ mm and $H=5$ mm. The baseline cladding cross-section area was selected to be a square of 10 mm by 10 mm.

3.2.2. Modal Analysis

As shown in the previous section, the fundamental propagation mode in a dielectric rod waveguide is E_{11} in which most of the electric field is propagated through the center of the waveguide core. Fig. 3-3(a) depicts the E- and H-field vectors of the fundamental mode in a DRW with an air cladding and an aspect ratio of 2:1. Fig. 3-3(b) and 3-3(c) show the E-field magnitude of the fundamental mode $E_{y_{11}}$ in the core cross-section and E-field vector, respectively. The E-field magnitude and vectors of the first three higher order modes are shown in Fig. 3-4(a), and Fig. 3-4(b) illustrates the E-field magnitudes for other higher order mode configurations that the DRW can support.

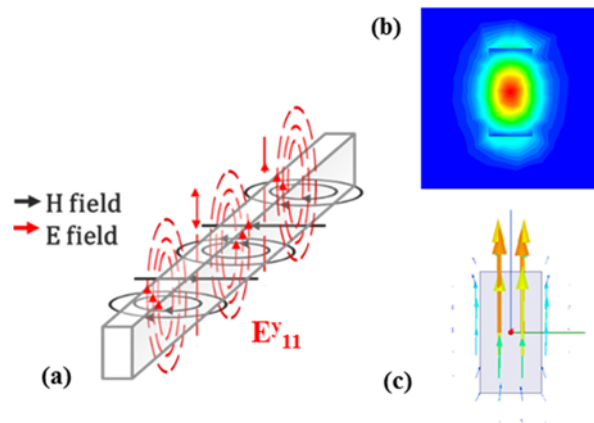


Figure 3-3: DRW fundamental mode E and H field vectors (a) $E_{y_{11}}$ field magnitude (b) and $E_{y_{11}}$ field vector (c) in the core cross-section.

The only dielectric waveguide geometries that possess exact analytical solutions to guided wave problems are the slab, circular cylinder and the elliptical cylinder waveguides. There is no exact solution to the propagation characteristics of a wave traveling along a rectangular dielectric guide or other cross-sectional geometries. The propagation characteristics for DRW with rectangular cross-sections must be found either numerically or by using approximate methods.

Even numerical computation of the fields in rectangular dielectric waveguides can be challenging due to the behavior of the fields in the waveguide corners and the nature of the boundary conditions. The transverse field components are known to be discontinuous and to diverge in the corners, especially for high refractive index ratios between the core and cladding, which might lead to slow convergence of the numerical methods [53].

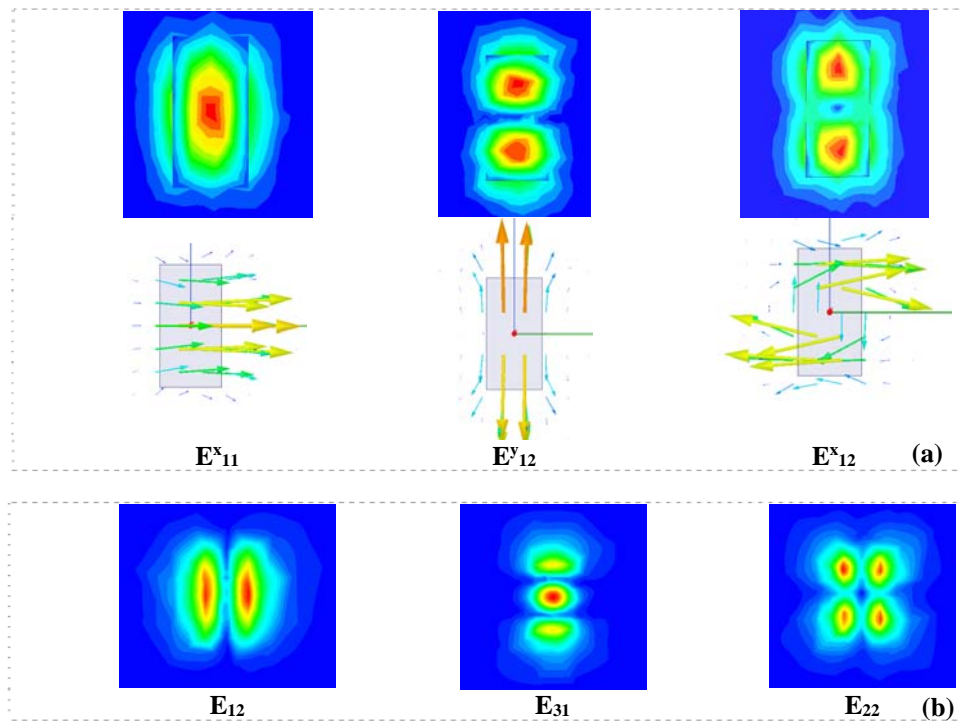


Figure 3-4: DRW E-field magnitude and vector for the first 3 higher order modes in a DRW with 2:1 aspect ratio and air cladding (a) and other common higher order modes (b).

Fig. 3-5 presents the normalized phase constant of the fundamental mode and the first three higher order modes of the DRW simulated using Ansys (HFSS). In this simulation, a DRW of Rogers RO3010 core is considered, the width of the core is 2.5 mm and the aspect ratio is 2:1. The results are presented for the DRW with an air cladding in Fig. 3-5(a) and ABS cladding in Fig. 3-5(b). The calculated phase constant using Marcatili's explicit approximation is also plotted in Fig. 3-5 for comparison purposes.

In Marcatili's approximation, the axial propagation constant β or K_z is given by

$$K_z = \sqrt{K_{core}^2 - K_x^2 - K_y^2}, \quad (3.4)$$

where K_x and K_y are the transverse propagation constants along x and y, respectively, and K_{core} is the propagation constant of a plane wave in a medium of refractive index n_{core} [51]. The mathematical expression of K_{core} is $K_0 n_{core}$ or $(2\pi/\lambda_0) n_{core}$ where λ_0 is the free space wavelength [51].

For E_{mn}^y modes the transverse propagation constants are given by [51]:

$$K_x = \frac{m\pi}{W} \left(1 + \frac{2A}{\pi W}\right)^{-1}, K_y = \frac{n\pi}{H} \left(1 + \frac{2A}{\pi H} \frac{n_{clad}^2}{n_{core}^2}\right)^{-1} \quad (3.5)$$

and for E_{mn}^x modes the transverse propagation constants are given by [51]:

$$K_x = \frac{m\pi}{W} \left(1 + \frac{2A}{\pi W} \frac{n_{clad}^2}{n_{core}^2}\right)^{-1}, K_y = \frac{n\pi}{H} \left(1 + \frac{2A}{\pi H}\right)^{-1} \quad (3.6)$$

where A is the maximum thickness for which an equivalent slab waveguide supports only the fundamental mode, or the maximum thickness in (3.1).

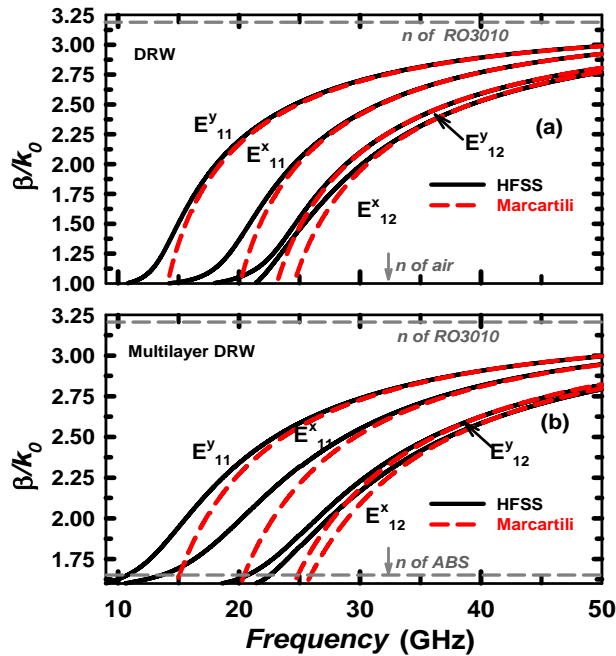


Figure 3-5: Dielectric rod waveguide normalized phase constants for the first 4 modes using Marcatili's explicit approximation [51] and numerical simulation.

It is important to mention that in Fig. 3-5(a) the normalized phase constant changes from 1, which corresponds to the refractive index of air, to the refractive index of RO3010 when the mode is totally confined. While

in in Fig. 3-5(b) the normalized phase constant varies from the refractive index of ABS at cutoff to the refractive index of RO3010, since in this case the core is surrounded by an infinite homogeneous ABS cladding.

Results in Fig. 3-5 show a good agreement well above cutoff between the EM simulation results and Marcatili's approximation for the DRW modes. The largest discrepancy occurs near the cutoff frequency for each mode due to the validity of the approximation assumptions.

Guided modes in the DRW vary sinusoidally inside the core and decay exponentially in the cladding. To obtain a closed form solution Marcatili assumes: a) well-guided modes, which means that most of the electric field is confined inside the core, b) the field strength in the areas on the core corners is negligible; these are illustrated as shaded regions in Fig. 3-6, and c) the refractive index of the core is slightly larger than the claddings, so the largest field components are normal to the propagation direction [51]. This derivation was realized in the Cartesian coordinate system by considering a DRW as a structure formed by two dielectric slab waveguides perpendicular to each other as shown in Fig. 3-6. These assumptions explain the discrepancies in the normalized phase constant of Fig. 3-5, as well-confined modes do not occur near cutoff but the field confinement improves as the frequency increases.

It is worth mentioning that among the modes shown in Fig. 3-5, only E_{y11} and E_{y12} will be excited if the DRW is fed with a rectangular waveguide (RWG). Consequently, the single mode operation bandwidth is determined by the cutoff frequency of both.

For design purposes an explicit mathematical expression that can accurately predict the DRW mode cutoff frequencies is highly desirable. The accuracy of full-wave EM simulations implies extensive computational time and resources, especially when multiple iterations of the waveguide dimensions and refractive indexes need to be considered. In the next section, a proposed closed-form model to determine the cutoff frequency of the DRW fundamental mode is presented.

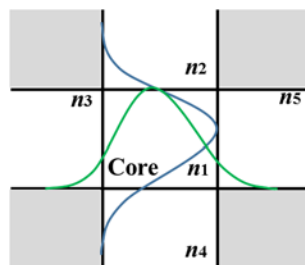


Figure 3-6: Cross-section of a DRW indicating the field variations in the core and cladding and the gray regions not considered in Marcatili's approximation.

3.3. Explicit Model for the Cutoff Frequency of the Multilayer DRW

In this section, an explicit model is proposed to calculate the cutoff frequency of the fundamental mode in multilayer DRW of 2:1 aspect ratio. Fig. 3-7 presents the cutoff frequency of 2:1 DRW for different values of core permittivity and widths. These values were obtained with full-wave EM simulations using Ansys HFSS. The curves in Fig. 3-7 consider a core immersed in an infinite homogeneous cladding of different permittivities, and in all cases the core and cladding materials are assumed to be lossless. A mathematical fit was performed to the data using the Levenberg–Marquardt algorithm. The resulting model equation is:

$$f_c = \frac{0.8c}{K W^{0.9} (\epsilon_r^{0.5} - 1)} \quad (3.7)$$

where W is the core width, c is the speed of light in vacuum and K is given by

$$K = 3.671 + 9.5244e^{-0.2297\epsilon_r} \quad (3.8)$$

The model equation is an adaptation of the dielectric slab waveguide expression for the dielectric rod. The model playback shows an excellent agreement with the simulated data. As shown in Fig. 3-7, increasing the core permittivity allows a reduction in the required core dimensions for the same cutoff frequency, as expected. Increasing the permittivity of the cladding also allows the core dimensions to be reduced. For the same core size, increasing the cladding permittivity from 1 (air) to 2.6 (ABS) can decrease the cutoff frequency by up to 1 GHz.

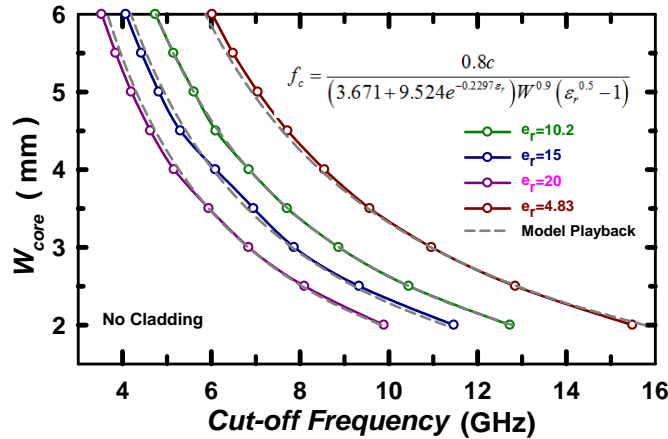


Figure 3-7: Simulated cutoff frequency for the dielectric rod waveguide fundamental mode and proposed model playback.

As mentioned previously, the model assumes a DRW core immersed in an infinite cladding. The normalized phase constant as a function of cladding size is presented in Fig. 3-8. The cladding considered is formed of ABS and has a square cross-section, as shown in Fig. 3-1. When the cladding dimensions increase, the cutoff frequency reduces

until it reaches a minimum after which there is no significant variation. In this case, a maximum reduction in the cutoff frequency of 1.25 GHz is achieved for sizes above 35x35 mm².

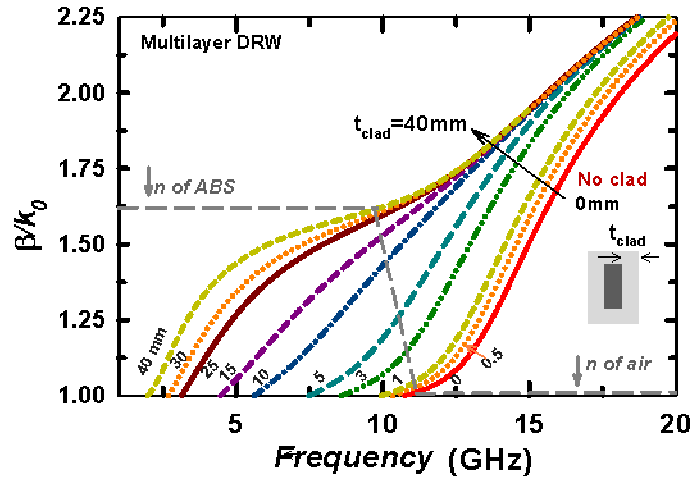


Figure 3-8: DRW normalized phase constants for the fundamental mode and variable cladding dimensions.

3.4. The Cladding Effect on the Multilayer DRW Performance

In this chapter, a transition to rectangular waveguide (RWG) is implemented to characterize the multilayer DRW. The transition, depicted in Fig. 3-9, has the DRW core partially inserted into the RWG and maintains the same electric field direction in both waveguides. The inserted core terminations are tapered to gradually match the impedance and to improve the coupling between the waveguides. In the following sub-sections, the effect of the cladding on the DRW performance is analyzed and the transition to WR-62 waveguide is considered in the simulations.

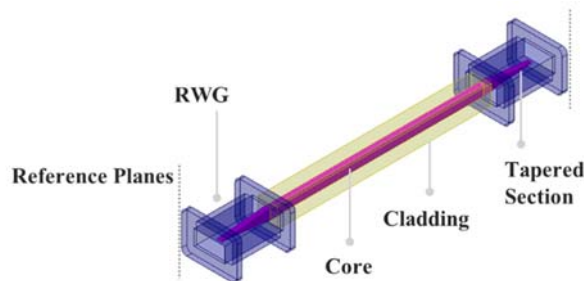


Figure 3-9: Diagram showing the transition from dielectric rod waveguide to rectangular waveguide.

3.4.1. Loss Tangent Variation

The effect of the loss tangent is studied in Fig. 3-10 by considering two cases separately: by varying cladding $\tan\delta$ for lossless as well as Rogers RO3010 cores, and by varying the core $\tan\delta$ for lossless as well as ABS claddings.

In both these cases, $\tan\delta$ is varied from 0 to 0.015. The simulated attenuation data are presented at 14 GHz and 18 GHz in Fig. 3-10(a) and (b), respectively. Across the entire frequency band, the attenuation is more sensitive to the core loss tangent than the cladding loss tangent, since most of the electromagnetic field propagates through the core. For the same reason, the difference between the attenuation curves for RO3010 and the lossless core (dashed and solid black lines) is larger than the difference between the curves for ABS and lossless cladding (dashed and solid red lines). This result is observed despite the fact that RO3010 has a lower loss tangent than ABS. In addition, the attenuation due to the loss tangent of the core shows a stronger frequency dependence than the attenuation due to the loss tangent of the cladding.

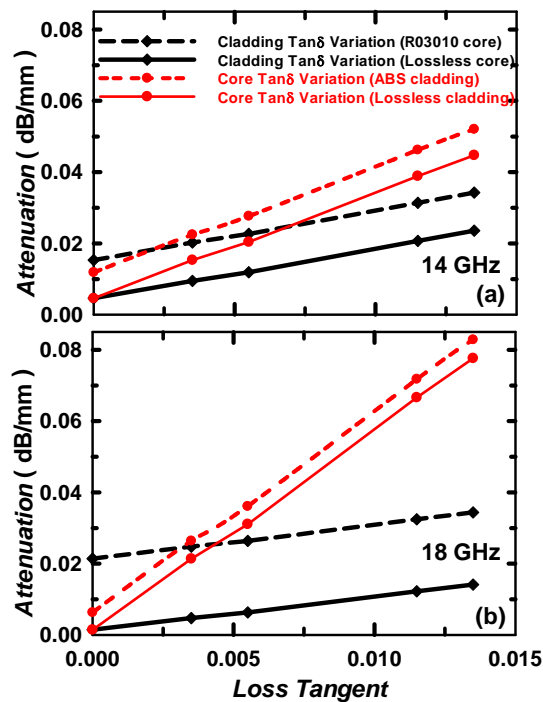


Figure 3-10: Simulated attenuation versus loss tangent variation at 14 GHz (a) and 18 GHz (b).

These results indicate that DRW design allows for more flexibility when choosing the cladding material than the core material since lossy claddings result in a smaller increase in the overall loss of the DRW. In this study, the data show that selecting a cladding with $\tan\delta=0.015$ over a cladding with $\tan\delta=0.0035$ results in an attenuation increment of ~ 0.02 dB/mm while a similar selection for the core results in $0.04 - 0.07$ dB/mm increase in attenuation.

It is worth mentioning that for the materials considered in this design, the simulations shown in Fig. 3-10 predict an attenuation of about 0.022-0.026 dB/mm at 14 and 18 GHz. The result can be obtained from the curve labeled ‘Core Tan δ Variation (ABS cladding)’ by reading the attenuation for $\tan\delta=0.0035$ (which is the loss tangent

of RO3010). Alternatively, the same result can also be obtained from the curve labeled ‘Cladding $\tan\delta$ variation (RO3010 core)’ at $\tan\delta=0.0052$ (which is the loss tangent of ABS).

3.4.2. Cladding Dimension Variation

The cladding dimension also influences the waveguide performance. Fig. 3-11 shows the 1 dB and 2 dB S_{21} cutoff frequency of the design formed by a Rogers RO3010 core and a square ABS cladding with a varying cross-sectional area. The 1 and 2 dB cutoff frequencies in this case are calculated as the point where S_{21} reduces by 1 and 2 dB from the minimum insertion loss. The results in Fig. 3-11 indicate that the optimal cross-section for this design is $20 \times 20 \text{ mm}^2$. As shown in Fig. 3-8, increasing the cladding size of the multilayer DRW (without any transition) reduces the fundamental mode cutoff frequency up to a certain value. For cladding sizes larger than $20 \times 20 \text{ mm}^2$ the apparent increase in the cutoff frequency is due to the ineffective feeding at the RWG transition. The results in Fig. 3-11 suggest that the best values for this design are between 10 and 20 mm.

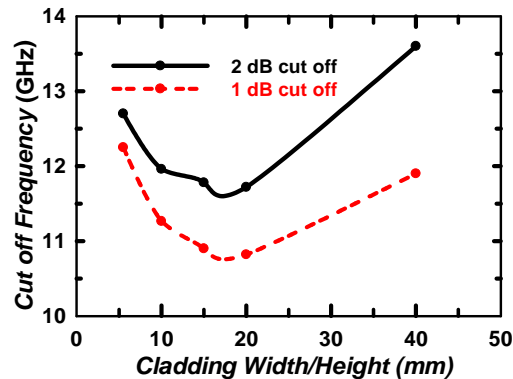


Figure 3-11: Simulated 1 dB and 2 dB cutoff frequency versus cladding width/height for square cross-sections.

3.4.3. Cladding Permittivity Variation

Fig. 3-12 presents the 1 dB and 2 dB S_{21} cutoff frequencies of the design formed by a Rogers RO3010 core and a $10 \times 10 \text{ mm}^2$ cladding with a relative permittivity from 1 to 7. As the permittivity increases from 1, the cutoff frequency decreases, thus providing more bandwidth. This result agrees with the one presented in Fig. 3-7 and shows that when the cladding permittivity increases the reduction of the cutoff frequency diminishes. In this case, the optimal values for permittivity lie between 2 and 4, since substantial decrease in cutoff frequency is observed in this range. The material chosen for this cladding (ABS) provides a 11.8% improvement in the 1 dB cutoff frequency.

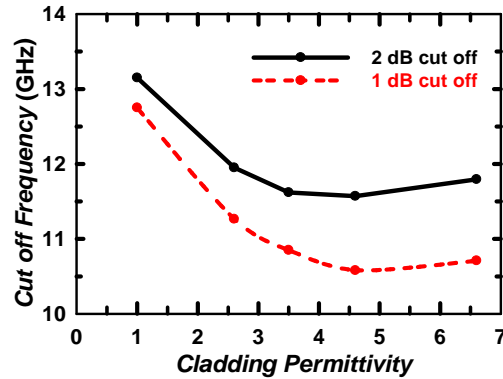


Figure 3-12: Simulated 1 dB and 2 dB cutoff frequency versus cladding permittivity.

3.5. DRW Experimental Characterization at the Ku Band

3.5.1. Straight DRW Characterization with and Without Cladding

The performance of the multilayer DRW was assessed with a transition to standard rectangular waveguide WR-62 as shown in Fig. 3-9. The dimensions of the design are presented in Fig. 3-13(a). The length of the tapered section at each port was optimized in HFSS using a parametric sweep. This type of transition to RWG has been effectively implemented at the W, D and F bands using sapphire or silicon waveguides [28, 45, 54].

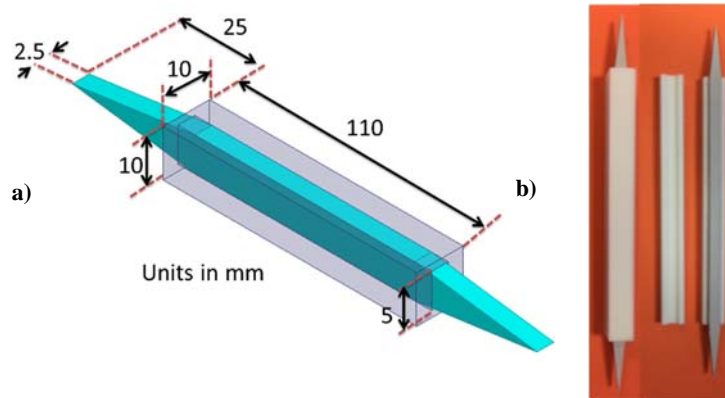


Figure 3-13: Diagram of the 2-port measurement setup showing the transition from dielectric rod waveguide to rectangular waveguide and the key dimensions (a) and fabricated DRW with cladding (b).

A picture of the fabricated multilayer waveguide is shown in Fig. 3-13(b). The RO3010 waveguide core was cut into shape using a Rabbit HX-1290SE laser cutter. A 10x10 mm² and 20x20 mm² cladding were manufactured as a hollow structure by fused deposition modeling of ABS with 100% infill and 150 μm layer thickness using a tabletop nScript 3D printer. A 50 micron layer of Rogers Ultralam 3850 liquid crystal polymer (LCP) ($\epsilon_r=3.14$, $\tan\delta=0.002$ at

10 GHz) was patterned and attached to the WR-62 flange to hold the DRW core in the center of the RWG aperture. The performance of this waveguide with and without a $10 \times 10 \text{ mm}^2$ cladding was presented in [50].

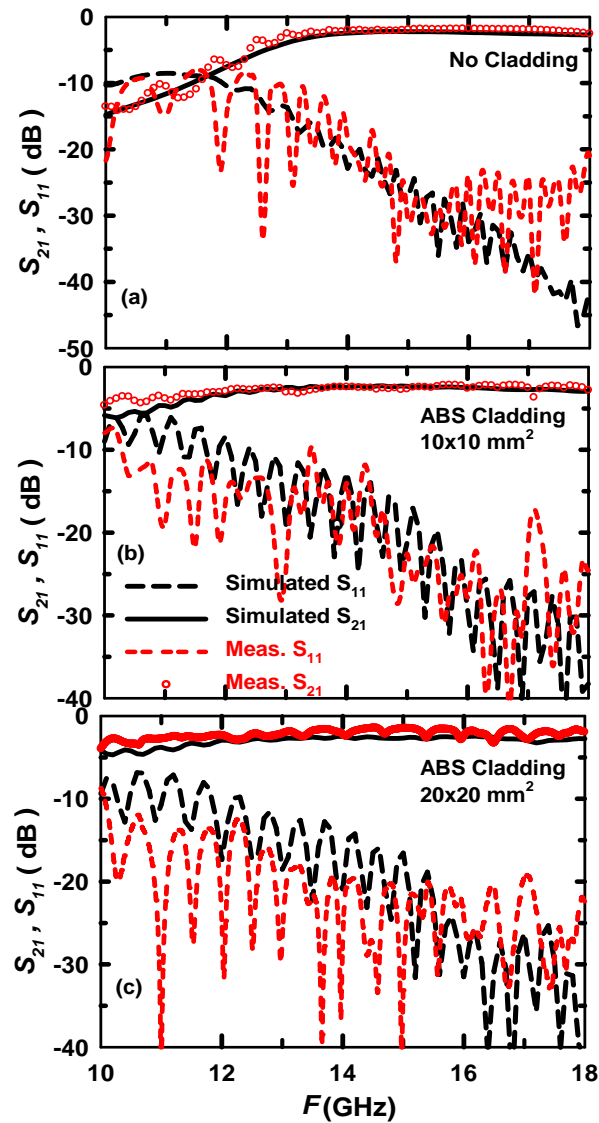


Figure 3-14: Measured and simulated S parameters for the Ku band DRW with transitions to RWG without cladding (a) [50], with $10 \times 10 \text{ mm}^2$ ABS cladding (b) [50] and with $20 \times 20 \text{ mm}^2$ ABS cladding (c).

The measured and simulated data of the Rogers DRW core without and with a $10 \times 10 \text{ mm}^2$ ABS cladding are shown in Fig. 3-14 (a) and (b), respectively. These results include the effects of back-to-back transitions to RWG. The addition of the cladding decreases the low end 1 dB and 3 dB cutoff frequencies by 1 GHz and 2.5 GHz, respectively. A total attenuation between 0.019 and 0.04 dB/mm is achieved over the extended Ku-band. The simulated and measured data for a design with a $20 \times 20 \text{ mm}^2$ cladding are presented in Fig. 3-14(c), showing even

greater improvement in the waveguide performance at low frequencies. In all cases, the measured S-parameters show good agreement with the simulated results and the discrepancies between the measured and simulated data can be ascribed to misalignments of the DRW during measurements.

A similar multilayer waveguide design was implemented for the Ku Band and completely fabricated using FDM. The cladding is made of ABS, while the core is formed using a custom ceramic composite. This design presents and 1 dB cutoff frequency reduction of 2 GHz when compared to the single layer waveguide. The multilayer DRW has an attenuation of ~0.02 dB/mm for a back to back transition at 18 GHz [55]. This attenuation value is comparable to the one of planar waveguides such as CPW lines in copper-clad LCP with a reported attenuation of ~0.02 dB/mm at 17 GHz [17, 22].

The presence of the cladding has minimal impact on the DRW insertion loss at higher frequencies since most of the electric field is concentrated in the waveguide core. The high frequency attenuation is thus comparable to the attenuation of a plane wave propagating in an infinite, uniform medium of the same material as the core. The attenuation of a plane wave is given by [56]

$$\alpha = \omega\sqrt{\mu\varepsilon} \left\{ \frac{1}{2} \left[\sqrt{1 + \left(\frac{\sigma}{\omega\varepsilon} \right)^2} - 1 \right] \right\}^{1/2}; \quad (3.9)$$

for low loss dielectric it can be approximated to

$$\alpha \approx \frac{\sigma}{2} \sqrt{\frac{\mu}{\varepsilon}}, \quad (3.10)$$

where $\sigma = \tan\delta\omega\varepsilon$. Using the properties of RO3010, (3.10) yields 0.018dB/mm at 18 GHz, which is comparable to the 0.023 dB/mm attenuation for the multilayer DRW shown in Fig. 3-14.

To achieve results comparable to those of the multilayer DRW but without the cladding, the core cross section needs to increase, which might impede an efficient transition to the metal waveguide feed. Increasing the core cross-section significantly with respect to the RWG aperture requires a longer tapered section that extends outside the RWG and can increase the transition loss. This can be a concern especially for lower permittivity cores that are inherently larger with respect to their high- k counterparts.

One of the benefits of the ABS cladding is that it can serve as a support for the DRW during packaging and integration into a system. In particular, there is potential electromagnetic interaction between the DRW and adjacent structures or electronics given the nature of the DRW field confinement. Fig. 3-15 shows the measured S-parameters of the waveguide-fed DRW with and without contact to a lossy, 10 Ω -cm silicon wafer. The top plot in the figure

demonstrates significant degradation in the S-parameters due to contact with the silicon substrate. The lower plot shows that with the cladding, which effectively inserts a 2.5 mm-thick ABS layer between the silicon and the DRW, there is no noticeable effect from the lossy substrate.

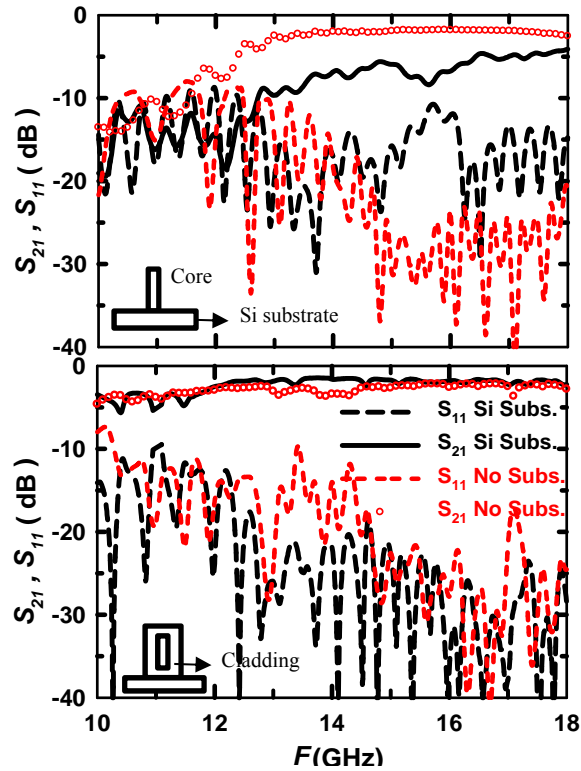


Figure 3-15: Measured S parameters for the Ku band DRW with transition to RWG without cladding (top) and with ABS cladding (bottom). Each showing measured data with and without a 10 Ω cm Si substrate.

3.5.2. Dielectric Rod Waveguide Bends

Fig. 3-16 shows the performance of a DRW with a 35 mm radius of curvature 90° bend without (a) and with (b) a 10 × 10 mm² ABS cladding. The results indicate that the use of cladding improves the performance of bends in the DRW by extending the operational bandwidth in the lower end of the frequency band. Additionally, by comparing the straight DRW in Fig. 3-14 and the bent DRW in Fig. 3-16, a reduction in the attenuation due to the bent section of the waveguide can be isolated. In this case, the attenuation of the bent section at 12 GHz is 10 dB and 1 dB for the DRW without and with cladding, respectively.

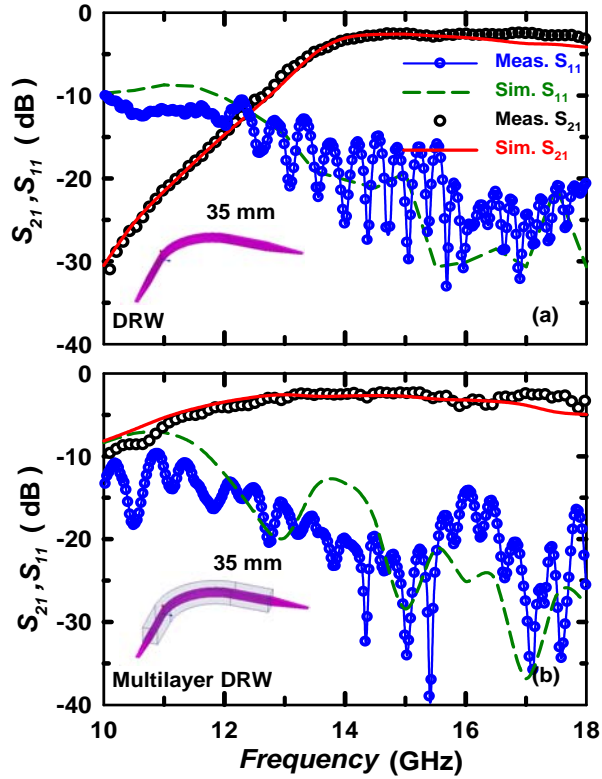


Figure 3-16: Measured and simulated S -parameters of the DRW core (a) and with $10 \times 10 \text{ mm}^2$ ABS cladding (b) for a 35 mm bend DRW.

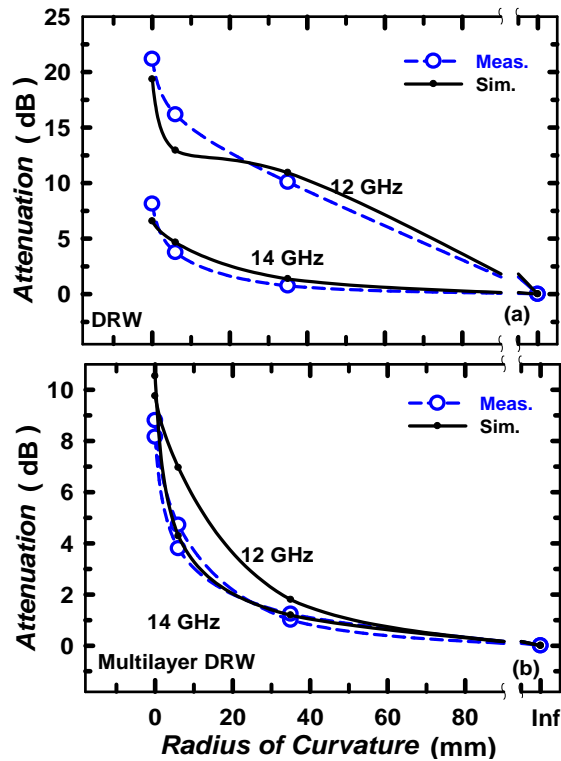


Figure 3-17: Simulated and measured attenuation versus radii of curvature of a DRW bend without (a) and with (b) the ABS cladding at 12 GHz and 14 GHz.

Fig. 3-17 shows the measured and simulated attenuation of DRW bends with different radii of curvature with and without the $10 \times 10 \text{ mm}^2$ ABS cladding at 12 and 14 GHz. As the radius of curvature decreases, a higher portion of the E-field is radiated resulting in higher attenuation. These data are normalized with respect to the straight waveguide (infinite radius of curvature). As the radius of curvature increases, the attenuation decreases and approaches 0 dB - the value for the straight waveguide. The effect of the cladding is significant at low frequencies, while for frequencies above 15 GHz the attenuation with and without the cladding is approximately the same, as shown in Fig. 3-16.

3.5.3. Loss Analysis for the Multilayer DRW

The total attenuation of the multilayer DRW is a function of the transition to RWG, the total length of the waveguide and the material properties of the core and cladding. The attenuation due to the DRW can be isolated from the attenuation due to the transitions by applying the multiline method [28, 57, 58]. This numerical calibration method is used to remove the effect of the transitions at each port from the uncalibrated S parameters. The cascade or transmission parameters of the entire system $[T_t]$ can be written as the multiplication of the cascade matrices of each transition $[T_{trans}]$ and the cascade matrix of the DRW $[T_{DRW}]$ as shown in (3.11)

$$[T_t]^i = [T_{trans1}] \cdot [T_{DRW}]^i \cdot [T_{trans2}], \quad (3.11)$$

where the index i denotes the length of the DRW. The transmission matrix of the entire system can be directly determined from the measured or simulated S parameters as

$$[T_t]^i = \frac{1}{S_{21}^i} \begin{bmatrix} S_{12}^i S_{21}^i - S_{11}^i S_{22}^i & S_{11}^i \\ -S_{22}^i & 1 \end{bmatrix}. \quad (3.12)$$

Assuming that the DRW is an ideal transmission line, its transmission parameters are given by

$$[T_{DRW}]^i = \begin{bmatrix} e^{-\gamma li} & 0 \\ 0 & e^{\gamma li} \end{bmatrix}, \quad (3.13)$$

where γ is the propagation constant and li is the physical length of the line.

Considering two dielectric rod waveguides of different lengths $L=li$ and $L=lj$, with otherwise identical parameters, (3.11) can be rewritten as follows

$$[T_t]^{ij} \cdot [T_{trans1}] = [T_{trans1}] \cdot [T_{DRW}]^{ij}, \quad (3.14)$$

where

$$[T_t]^{ij} = [T_t]^j \cdot [T_t]^{i-1}, \quad (3.15)$$

and

$$[T_{DRW}]^{ij} = [T_{DRW}]^j \cdot [T_{DRW}]^{i-1}. \quad (3.16)$$

Substituting (3.13) into (3.16), the combined transmission parameters of the two waveguides $[T_{DRW}]^{ij}$ can be written as:

$$[T_{DRW}]^{ij} = \begin{bmatrix} e^{-\gamma(lj-li)} & 0 \\ 0 & e^{\gamma(lj-li)} \end{bmatrix}. \quad (3.17)$$

Since $[T_{DRW}]^{ij}$ is a diagonal matrix, its diagonal elements are the eigenvalues of $[T_{DRW}]^{ij}$ and these are also the eigenvalues of $[T_t]^{ij}$ as shown in (3.14). The eigenvalues of $[T_t]^{ij}$ can be calculated from the combined system's transmission matrix as follows

$$\lambda_{1t}^{ij}, \lambda_{2t}^{ij} = \frac{(T_{t11}^{ij} + T_{t22}^{ij}) \pm \sqrt{(T_{t11}^{ij} - T_{t22}^{ij})^2 + 4 T_{t12}^{ij} T_{t21}^{ij}}}{2}. \quad (3.18)$$

The resulting eigenvalues of $[T_t]^{ij}$ can be equated to the eigenvalues of $[T_{DRW}]^{ij}$ to determine the transmission line's propagation constant. The eigenvalues of $[T_{DRW}]^{ij}$ are given by

$$\lambda_{1DRW}^{ij}, \lambda_{2DRW}^{ij} = e^{\pm\gamma(lj-li)}. \quad (3.19)$$

Finally, the DRW propagation constant can be expressed as

$$\gamma = \frac{\ln(\lambda_t^{ij})}{li-lj}, \quad (3.20)$$

where λ_t^{ij} is the average of both eigenvalues

$$\lambda_t^{ij} = \frac{1}{2} \left(\lambda_{1t}^{ij} + \frac{1}{\lambda_{2t}^{ij}} \right). \quad (3.21)$$

Therefore the total attenuation of the multilayer DRW can be calculated as:

$$\alpha_{Total} = \text{Re}\{\gamma\}. \quad (3.22)$$

The attenuation due to radiation can be calculated with (3.22) by repeating the multiline method this time with lossless waveguides. Finally, the attenuation due to the dielectric can be determined by subtracting the attenuation due to radiation from the total attenuation:

$$\alpha_{Dielectric} = \alpha_{Total} - \alpha_{Radiation}. \quad (3.23)$$

The resulting attenuation due to the dielectric, due to radiation and the total attenuation are presented in Fig. 3-18 for the proposed DRW design without (a) and with (b) a $10 \times 10 \text{ mm}^2$ ABS cladding. As expected, the addition of the cladding reduces the total attenuation at lower frequencies without negatively impacting the attenuation at higher frequencies. In both cases the maximum attenuation due to the dielectric is $\sim 0.023 \text{ dB/mm}$. The attenuation due to the

dielectric increases with frequency since a higher portion of the E-field travels through the dielectric. The attenuation due to radiation is very low for the DRW with cladding in the entire frequency range and for the DRW without cladding above 14 GHz. The average $\alpha_{Radiation}$ above 14 GHz in both cases is $\sim 7 \times 10^{-4}$ dB/mm.

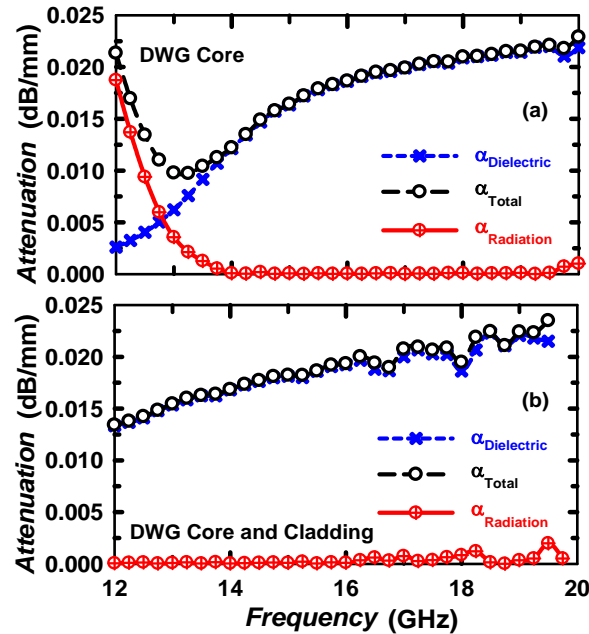


Figure 3-18: Attenuation of the DRW without (a) and with (b) ABS cladding due to radiation, due to the dielectric and total attenuation.

The difference between the calculated values of the total attenuation in a 110 mm long DRW and the measured S_{21} is presented in Fig. 3-19. This additional loss is due to the transition to RWG and impedance mismatch. Above 14 GHz where the DRW is well matched, the attenuation is mainly due to the transition. For the DRW with and without cladding, the attenuation due to the transition ranges from 0.2 dB to 0.55 dB per transition.

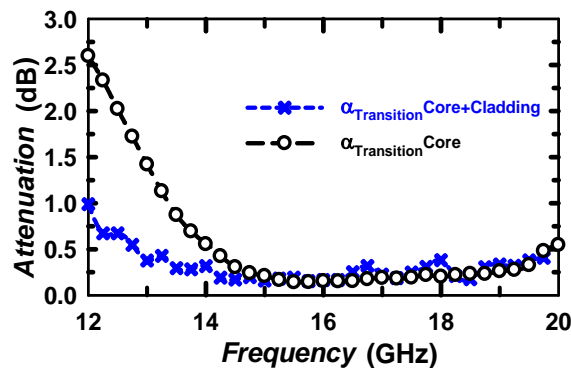


Figure 3-19: Attenuation of the DRW due to the transition to RWG and impedance mismatch with and without ABS cladding.

3.6. D Band Dielectric Rod Waveguide

As operating frequencies are continuously pushing the limits to sub-mm wave range and beyond it becomes crucial to count on effective, low loss waveguiding structures at high frequencies. It is within the scope of this research to implement a low loss DRW to operate at the D band (110-170 GHz), and that is fabricated completely using FDM.

As a first approach a scaled version of the DRW presented in section 3.3 was implemented for the D-band. This waveguide was fabricated by laser machining a Rogers RO3010 laminate for the core. Fig. 3-20 (a) shows the DRW geometry and the key parameters: $W=0.32\text{mm}$, $H=0.64\text{mm}$, $L_t=4\text{mm}$, $L_D=10\text{mm}$.

A transition to rectangular waveguide was implemented using standard straight rectangular WR 06. Fig. 3-20 (b) shows a diagram and (c) a picture of the set up used to perform the D band measurements. A D band T/R and T frequency extension modules by OML were connected to an Agilent PNA N5227A. Two straight WR 06 rectangular waveguide pieces were connected to the module's output to protect the connectors and to facilitate the calibration process. Two additional straight WR 06 waveguide pieces were attached to serve as transitions. It can be noticed from the diagram that the calibration reference planes do not include the pieces used for transition purposes. In a similar way as its low frequency counterparts the dielectric waveguide core was placed in the center of the rectangular waveguides to perform the measurements. To hold the waveguide in place a 50 micron layer of Rogers Ultralam 3850 (LCP) was used.

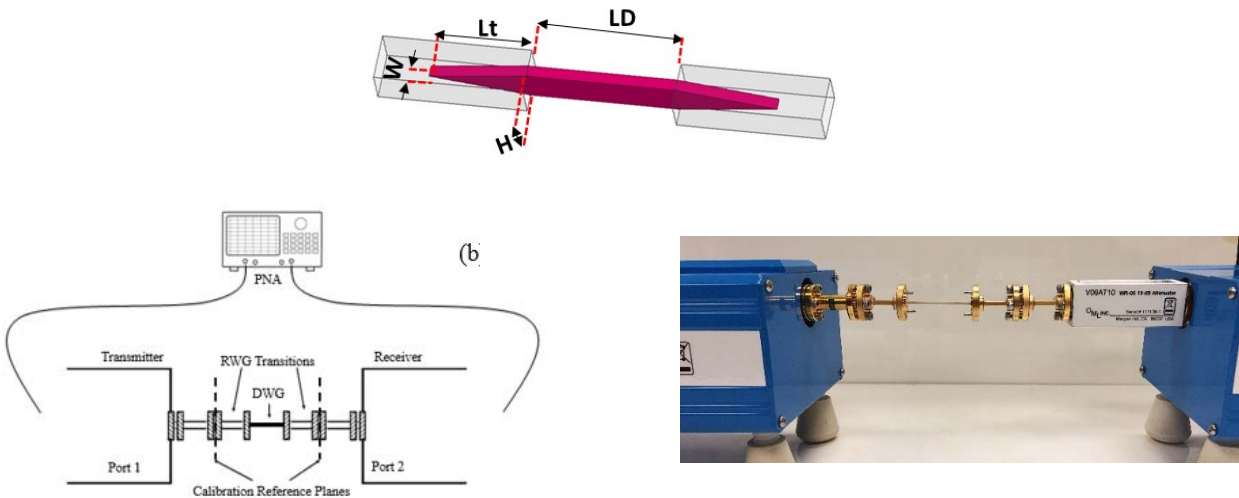


Figure 3-20: Illustration of solid core DWG ($W=0.32\text{mm}$, $H=0.64\text{mm}$, $L_t=4\text{mm}$, $L_D=10\text{mm}$) (a), diagram of the D-band measurement setup (b), and picture of the D-band measurement setup (c).

Fig. 3-21 presents the measured and simulated S parameters of the D band DRW. Excluding transition loss, the measured attenuation at mid-band with a back to back transition to rectangular WR 06 waveguide is 0.44 dB/mm. The discrepancies between the simulated and measured data shown in Fig. 3-21 are attributed to the underestimation of the Rogers RO3010 loss factor at the D Band, microwave properties for the Rogers material were assumed in the simulations. Further geometry optimizations are being made to improve the design performance in this frequency range.

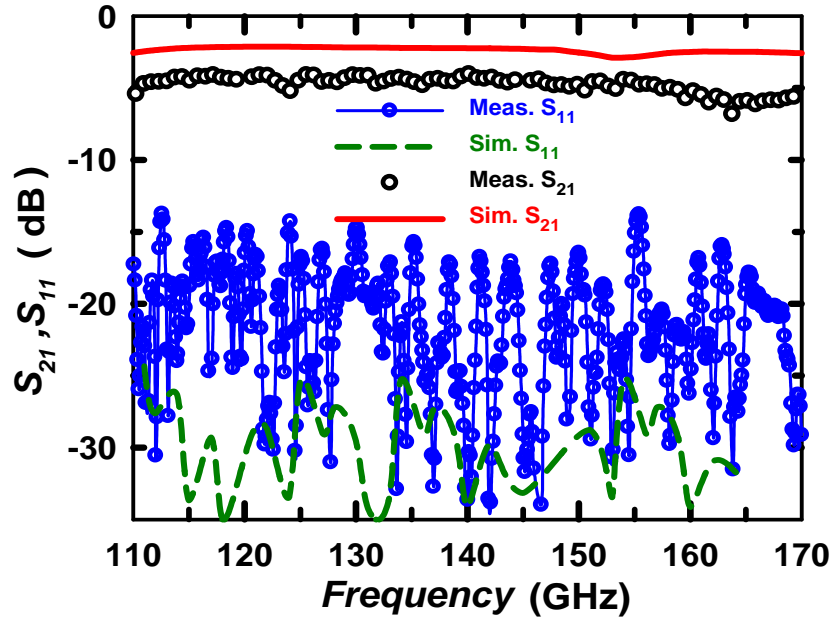


Figure 3-21: Measured and simulated D band S-parameters.

3.7. Conclusions

The design and performance of a multilayer dielectric rod waveguide with rectangular cross-section and 2:1 core aspect ratio has been studied at the extended Ku band (10 to 18 GHz). A mathematical model is presented to predict the fundamental mode cutoff frequency of the multilayer DRW as a function of the material properties and core dimension. The model is an adaptation of the dielectric slab waveguide cutoff frequency expression for the dielectric rod and it aims to 1) reduce the extensive simulation time in the design stage that results from full-wave EM simulations, and 2) provide an insight into the relationship between the variables. The simulation time of DRW with rectangular cross-section is higher than for other geometries due to the waveguide corners and it is even more significant when several iterations are needed to determine the appropriate core cross-section dimension for a specific

material and a specific frequency of interest. The proposed model shows an excellent agreement with the full-wave EM simulated data.

The performance of the multilayer DRW is proven to be superior compared to its single layer equivalent. The multilayer design shows a 16.7% and 24% improvement of the 1 dB cutoff frequency for $10 \times 10 \text{ mm}^2$ and $20 \times 20 \text{ mm}^2$ cladding areas, respectively. It also shows significant improvements in the lower end of the band for 90-degree waveguide bends. In particular, the attenuation at 12 GHz for a 35 mm radius of curvature bend is reduced by 9.5 dB when compared to a bent single-layer rod waveguide of the same core dimension. The attenuation due to the DRW and due to each transition to RWG was extracted using numerical calibration. The resulting values show a maximum attenuation of $\sim 0.023 \text{ dB/mm}$ due to the dielectric, an attenuation due to each RWG transition between 0.2 and 0.55 dB, and an attenuation due to radiation of about $7 \times 10^{-4} \text{ dB/mm}$.

CHAPTER 4: KU-BAND ADDITIVE MANUFACTURED MULTILAYER DIELECTRIC ROD WAVEGUIDE

4.1. Introduction

In this chapter a multilayer dielectric waveguide design completely fabricated with additive manufacturing techniques is characterized over the extended Ku-band (10-18 GHz). The multilayer DRW is formed by a medium- k dielectric core printed with a custom-made ceramic composite and a low permittivity ABS cladding. It is demonstrated that the 3D printed multilayer waveguide performance is comparable to a multilayer waveguide created with traditional fabrication methods and commercial materials. The device performance is measured with and without the presence of the low permittivity cladding. It is proven that cladding improves the 1dB operational bandwidth by 50%.

4.2. Preparation and Characterization of the Medium- k Electromagnetic Composites for FDM

4.2.1. Preparation of Ceramic Thermoplastic EM Composites

Zeonex[®]RS420, an amorphous thermoplastic polymer based on Cyclo Olefin Polymer (COP), which is widely used for injection molding and conventional machining of optical components, was used as the polymer matrix. COP has a melting temperature of about 280°C and a glass transition temperature of 136°C, which is superior to other widely used thermoplastics such as ABS, Polypropylene (PP), and PLA. It is chemically inert to strong acids and solvents. Meanwhile, the tested dielectric and loss properties of high- k MgCaTiO₂ ceramic fillers (MCT-140 from Trans Tech Inc.) chosen for this work were $\epsilon_r \sim 127.26$ and $\tan \delta < 0.0012$ at 6GHz.

The high- k ceramic powders were sintered at 1200°C to further enhance their dielectric and loss properties as reported in [3]. This process achieves the highest ϵ_r and lowest $\tan \delta$ with the lowest ceramic filler volume fraction for the desired EM properties, thus avoiding feedstock filament brittleness. The FDM feedstock filament preparation process starts by pulverizing the sintered ceramic particles using a high-energy ball milling tool for 24 hrs, followed by a sieving process to ensure that the maximum particle sizes are below 38 μm . The COP thermoplastic matrix and

The content of this chapter has been published in [51] and it is included in this dissertation with permission from the IEEE. A copy of the permission is included in the Appendix A-2.

sintered ceramic particles are then uniformly mixed along with a hyperdispersant using a planetary centrifugal mixer at the desired volume fraction, followed by a hot extrusion compounding process at 220°C to produce loaded filaments with a diameter of ~ 1.65 mm.

4.2.2. Dielectric Characterization of EM Composites

The dielectric properties of 330 μm -thick FDM printed thin-sheet specimens composed of the medium- k 30 vol. % COP-MgCaTiO₂ were assessed at Ku-band using a cavity resonator test fixture (015 from Damaskos Inc.) and an 8720ES vector network analyzer from Keysight Technologies. The measured EM properties are $\epsilon_r \sim 4.82$ and $\tan \delta \sim 0.0018$ at 17 GHz. The fabrication, modeling and characterization of this medium- k and low loss EM composite is reported by Castro *et al.* in [20].

4.3. Multilayer Dielectric Rod Waveguide (DRW) Design and Fabrication

The proposed multilayer DRW design presented in [50] was modified to allow for a complete fabrication using direct digital manufacturing (DDM). The modified DRW design is comprised of a medium permittivity dielectric rod waveguide core with rectangular cross-section surrounded by a low permittivity cladding. Fig. 4-1 presents the design geometry and key dimensions of the Ku-band DRW design. The width of the core (W) was selected according to (3.1) for single mode operation of the dielectric slab waveguides. This is a suitable approximation, which can be optimized using High Frequency Structure Simulator (HFSS) by Ansys; The height of the core was set as twice the width to avoid cross polarization and field degeneracies [45, 51]. The cladding has a square cross-section and the dimensions were also varied in HFSS to achieve the desired response. As shown in Fig. 4-1, the DRW core is terminated with tapered sections at both ends, which are the transitions to rectangular waveguide for measurement purposes.

The complete multilayer waveguide system was fabricated and fully developed by using FDM. The in-house prepared ceramic composites used for the core exhibit higher dielectric constant than other commercially-available materials for FDM ($\epsilon_r = 4.82$ and $\tan \delta = 0.0018$ at 17 GHz). The material selected for the low permittivity cladding is ABS ($\epsilon_r = 2.6$ and $\tan \delta = 0.0052$ at 17 GHz), which is readily available for FDM.

The dielectric waveguide core and cladding filaments were separately extruded through a 125 μm inner diameter ceramic tip at 290°C and 235°C, respectively. Both pieces were then individually patterned using 200 μm layer height and a 100% infill. These parts were printed onto a metallic bed heated at 140°C and 110°C for the core

and cladding, respectively. The process was realized with an nScript 3Dn Tabletop printer. Fig. 4-2 shows the FDM fabricated dielectric waveguide core (top) and the entire DRW waveguide with cladding (bottom).

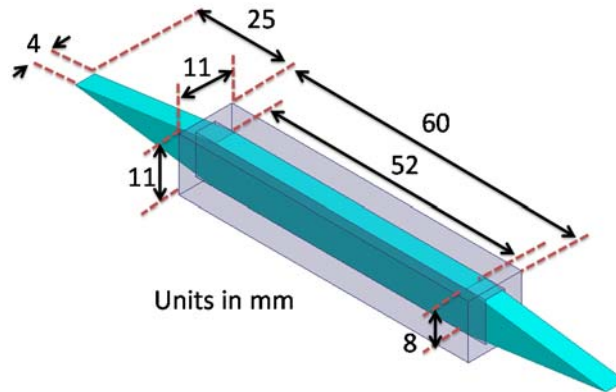


Figure 4-1: Proposed multilayer dielectric rod waveguide design and dimensions.



Figure 4-2: Picture of the FDM-fabricated dielectric rod waveguide without the cladding (top) and with the ABS cladding (bottom).

4.4. Characterization and Measured Results

To measure the multi-layer DRW, transition to a pair of WR-62 straight rectangular waveguide was implemented. The tapered sections of the DRW core were partially inserted inside the rectangular waveguide ports to gradually match the impedance and allow the coupling between them. A 50 micron layer of Rogers Ultralam 3850 liquid crystal polymer (LCP) ($\epsilon_r=3.14$, $\tan \delta=0.002$ at 10 GHz) was patterned and attached to the WR-62 flange to hold the DRW core in position.

Fig. 4-3 presents the simulated and measured S parameters of the DRW core with a back-to-back transition to a pair of WR-62 ports without and with the ABS cladding for the extended Ku band (10-18 GHz). It can be noticed that the addition of the cladding extends the waveguide 1 dB and 2 dB cut-off frequencies by 2 GHz and 2.2 GHz, respectively, thus improving the 1 dB operational bandwidth by 50%. The addition of the cladding does not affect the performance of the waveguide at the higher end of the Ku band since the majority of the electric field travel through the core and the attenuation is determined by the loss tangent of the core at high frequencies.

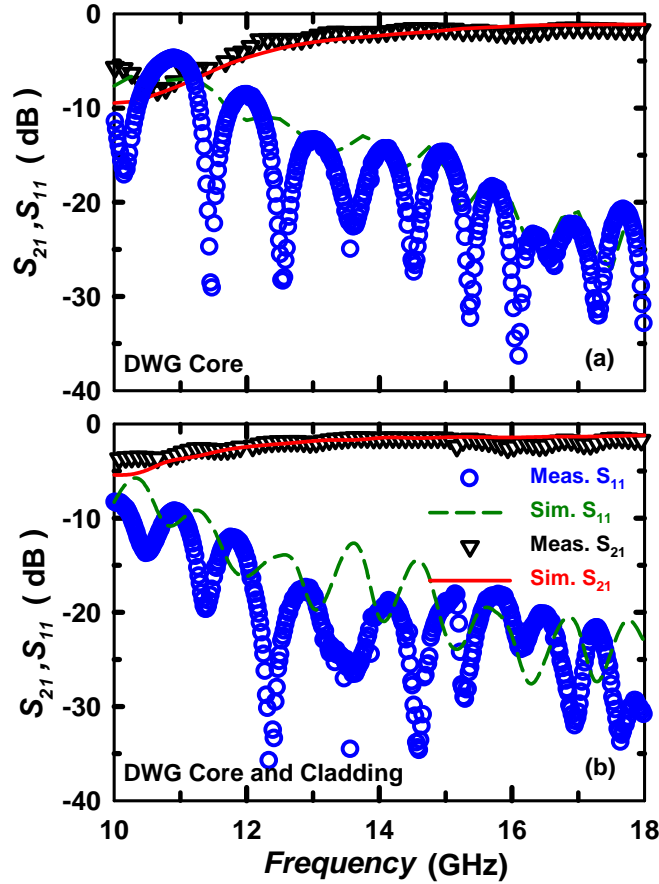


Figure 4-3: Measured and simulated S -parameters for the DRW with transition to WR-62 waveguide ports without cladding (a), and with ABS cladding (b).

The insertion loss of the multilayer dielectric rod waveguide falls within 0.01 dB/mm and 0.012 dB/mm in the extended Ku Band. The attenuation due to each end transition for the DRW without cladding is 0.9 dB and 0.29 dB at 14 and 18 GHz, respectively. The attenuation due to each transition for the DRW with cladding is 0.46 dB and 0.29 dB at 14 and 18 GHz respectively. The overall performance of the 3D printed multilayer waveguide presented in Fig. 4-3 is on par with the previously reported multi-layer DRW that was fabricated from a commercial high- k material not compatible with FDM [50]

The dielectric rod waveguide performance and cut-off frequency are mainly determined by the material properties and its cross-sectional dimensions. Increasing the dimensions of its cross section shifts the waveguide operational bandwidth to a lower frequency range. The cross-section of the DRW is inversely proportional to the material permittivity as shown in (1). If the core material has a medium permittivity value, the core cross-section must be enlarged compared to a higher dielectric constant design for the same frequency range. Depending on the actual

dimensions, effectively coupling between a medium- k design and a standard rectangular waveguide might be challenging.

Since there are no high- k FDM-ready materials available, the addition of a low permittivity cladding is an effective solution to miniaturize the waveguide core. It increases the waveguide effective permittivity and lowers the cut-off frequency, without affecting the core dimension, the transition to rectangular waveguide or the overall attenuation. Also, as reported in [50] it encases the electric field that propagates outside the core to decrease the electromagnetic interaction with its surroundings. To achieve the same bandwidth of the multi-layer DRW as shown in Fig. 4-3, without the use of the cladding, the core cross-sectional area must increase by 4 times, and the taper sections would be twice as long.

It is worth mentioning that the proposed DRW design is very sensitive to the permittivity of the core and cladding materials as well as the cross-sectional areas. Hence, further improvements can be achieved through strategic adjustment of the material properties and dimensions.

4.5. Conclusions

A multilayer DRW proposed for the extended Ku-band (10-18 GHz) was fabricated using FDM. An in-house prepared ceramic composite based on 30 vol.% COP-MgCaTiO₂ with fillers sinter at 1200°C was selected 3-D printing of the core. It exhibits higher permittivity than all commercially available FDM-ready materials. The DRW waveguide core is encased in a low permittivity cladding fabricated by FDM using ABS.

The addition of the ABS cladding extends the 1 dB cut-off frequency by 2 GHz, therefore increasing the bandwidth by 50%. The overall performance of the additive manufactured multilayer design is on par with the multilayer DRW made of commercial printed circuit board (PCB) materials reported in [50]. The ABS cladding allows the miniaturization of the core cross-sectional area by a factor of 4 while resulting in a smoother transition to rectangular waveguide. The proposed DRW can be easily scaled to other frequency ranges and the rectangular cross-section is amenable to system integration.

CHAPTER 5: KU BAND METAL-STRIP-LOADED DIELECTRIC ROD WAVEGUIDE FILTER

5.1. Introduction

Novel dielectric waveguides have proven to be low loss effective waveguiding structures at mm wave frequencies and beyond [26]. To avoid cross-talk between neighboring dielectric ribbon waveguides and improve packing density, embedded band stop filters have been designed by alternating high and low dielectric constant sections [59]. Dielectric ribbons waveguides are compatible with PCB multilayer technologies and on wafer integration [33, 59].

This chapter presents a band stop filter formed by a corrugated metal pattern on a dielectric rod waveguide. The band stop center frequency can be tuned by adjusting the metal strips periodicity. The corrugated metal pattern spacing can be optimized to achieve optimum performance at the desire frequency without degrading the waveguide attenuation in the pass band. Some of the advantages of the proposed design are the simple and low-cost fabrication process, the embedded nature of the design and the straightforward scalability to other frequency bands. The combination of different metal patterns on a single DRW will be explored in a future work to allow multiple band rejection.

5.2. Metal-Strip-Loaded Dielectric Rod Waveguide (MSL DRW) Design and Fabrication

The proposed design is formed by a high permittivity dielectric rod core with rectangular cross-section and a metal grated pattern on the rod top and bottom as illustrated in Fig. 5-1. The loaded waveguide was optimized for the Ku band using Ansys (HFSS) and the resulting dimensions are: $L_{\text{taper}}=25$ mm, $L_D=110$ mm, $W=2.5$ mm, $H=5$ mm, $L_m=1.12$ mm and $L_{\text{gap}}=4$ mm. The waveguide width was initially selected according to the dielectric slab waveguide single mode operation, prior to the optimization [50]. A waveguide height to width ratio of 2:1 was chosen to break the field degeneracies [50].

The high permittivity DRW core is made from Rogers RO3010 ($\epsilon_r=10.2$ a loss tangent=0.0035 @ 9 GHz) and it was cut into shape using a Rabbit HX-1290SE laser machine. The metal strip layer was fabricated using copper foil taper that was patterned with a cutting machine. The copper foil thickness is 0.07 mm.

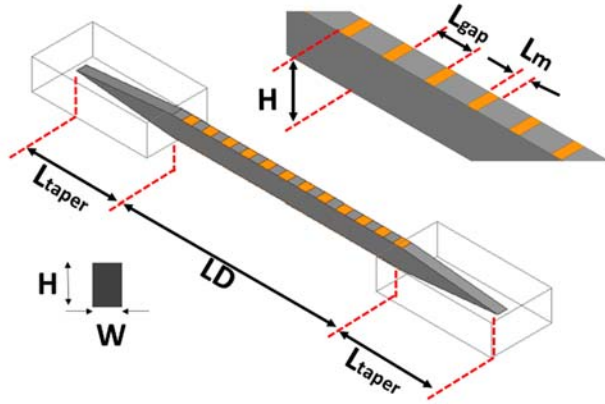


Figure 5-1: MSL DRW geometry and key parameters.

5.3. MSL DRW Characterization and Measured Results

A transition to WR-62 was implemented to characterize the proposed MSL DRW in the Ku Band, from 12 to 18 GHz. As shown in Fig.5-1 the ends of the DRW are tapered and inserted into the rectangular waveguide to gradually match the impedance. A 50 micron layer of Rogers Ultralam 3850 liquid crystal polymer (LCP) ($\epsilon_r=3.14$, $\tan\delta=0.002$ at 10 GHz) was patterned and attached to the WR-62 flange to hold the DRW core in the center of the RWG aperture.

Fig. 5-2 presents the simulated and measured S parameters of the MSL DRW. The metal strip length is $L_m=1.12 \text{ mm} \sim \lambda_g/5$ and the spacing is $L_{\text{gap}}=4 \text{ mm} \sim 1.5 \lambda_g$ at the resonant frequency. The measured data shows a maximum band stop rejection of 28 dB at 16.2 GHz and 1 GHz bandwidth. The passband attenuation is between 1.5 and 2.2 dB for a 110 mm long dielectric rod which is comparable to the attenuation of an equivalent non-loaded DRW [50]. The reflection coefficient of the MSL DRW is below -10 dB in the passband and it rapidly increases in the stop band reaching -0.9 dB. It can be noticed from Fig. 5-2 a good agreement between the measured and simulated data, small discrepancies can be ascribed to misalignments during measurements.

The band stop center frequency can be adjusted by changing the periodicity of the metal strips. Fig. 5-3 shows the simulated transmission coefficient versus frequency for different metal strip spacing L_{gap} . The frequency at which the maximum rejection occurs decreases as the spacing between the metal strips increases. It can be noticed from Fig. 5-3 that the rejection level also decreases as L_{gap} increases. Since the corrugated metal layer considered covers the totality of the DRW length, increasing the strip separation decreases the number of metal strips. Each transition

between non-loaded dielectric and loaded dielectric section can be considered as a filter stage, a greater number of filter stages will lead to a higher band stop rejection.

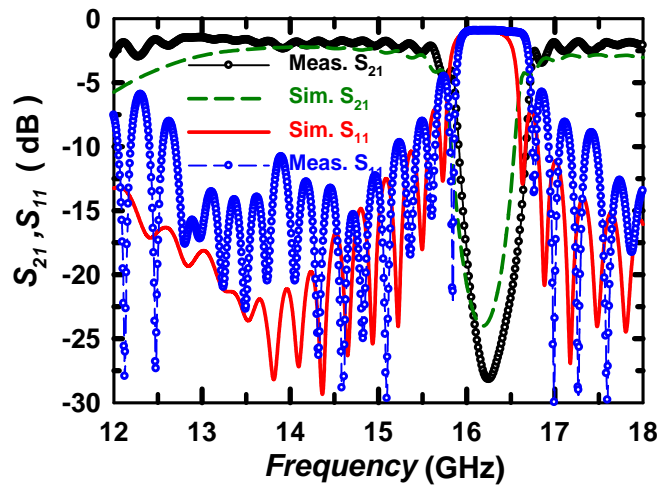


Figure 5-2: Measured and simulated S parameters of the MSL DRW of $L_m=1.12$ mm and $L_{gap}=4$ mm.

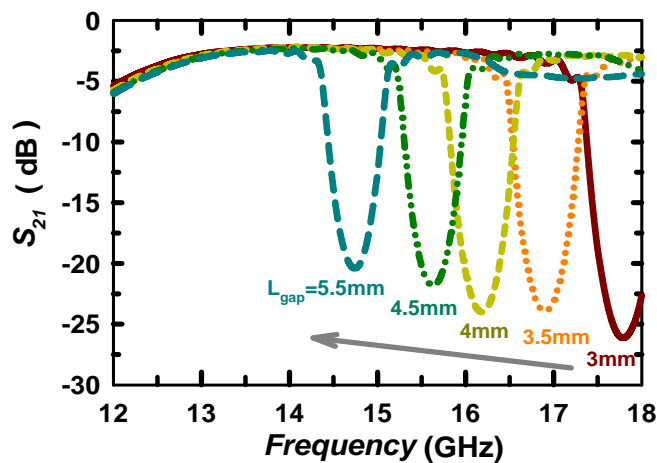


Figure 5-3: Simulated transmission coefficient of the MSL DRW of $L_m=1.12$ mm and variable L_{gap} .

Fig. 5-4 shows the simulated S parameters of the MSL DRW for two different strip spacings $L_{gap}=3$ and 5.5 mm with 14.7 and 17.7 GHz stop band frequencies respectively. It can be noticed that the reflection coefficient remains below -10 dB in the pass band in these two cases and it also does for all the other L_{gap} values in between. Stop band rejection above 20 dB is observed in both cases.

Adjusting the metal strips length L_m has also an effect on the band stop center frequency and bandwidth. It was observed from simulated data that larger values of L_m can lead to significant degradation of the reflection coefficient.

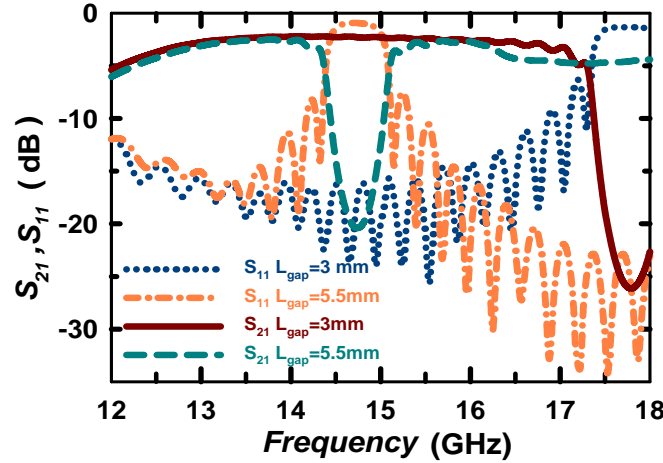


Figure 5-4: Simulated S parameters of the MSL DRW of $L_{gap}=3$ and 5.5 mm.

5.4. Conclusions

A metal grating pattern was implemented in a high permittivity dielectric rod waveguide obtaining a band stop behavior at a frequency determined by the metal pattern distribution. Up to 28 dB rejection was measured at 16.2 GHz for $L_m=1.12$ mm and $L_{gap}=4$ mm. It is shown that the addition of the conductive corrugated layer does not negatively affect the attenuation in the passband and the reflection coefficient remains below -10 dB. Strip spacings ranging from 3 to 5.5 mm can be implemented to obtain resonant frequencies from 14.7 to 17.7, which cover almost the entire Ku band, in all cases the rejection level is above 20 dB.

CHAPTER 6: MULTILAYER DIELECTRIC END-FIRE ANTENNA WITH ENHANCED GAIN

6.1. Introduction

Dielectric rod antennas are an attractive option for millimeter-wave integrated circuits due to their small size, low cost, high gain and broadband performance [50, 60]. Numerous applications make use of end-fire, highly directive radiation; and dielectric rod antennas (DRA) are commonly used in these cases. Designs in applications such as satellite communications [5], radar systems, chip-to-chip communications [7], and millimeter-wave imaging [8, 9], have been successfully developed.

It is well known that gain enhancements in DRAs can be achieved by increasing the rod permittivity or the rod diameter. Increased gain is also possible with increased antenna length, although this may degrade other antenna parameters such as cross polarization and side lobe levels [4]. Increasing the core diameter, on the other hand, may affect the operational bandwidth, since higher order modes are excited at frequencies where the diameter becomes much larger than the guided wavelength [4]. Gain improvements have been reported in [61] where two low permittivity dielectrics are used with a small refractive index difference and a custom metal waveguide transition. Additionally, the implementation of multiple dielectric layers in circular DRAs is often used to improve the antenna bandwidth [62, 63]. In other types of antennas such as dipoles, variation of the substrate dielectric constant has been studied as a means to enhance the broadside gain [64].

The present chapter addresses the characterization and gain enhancement of a low permittivity cladding in a DRA design with rectangular cross-section, a concept initially presented in [50]. The multilayer DRA design is comprised of a high permittivity core ($\epsilon_r = 10.2$) encased in a low permittivity cladding ($1.6 \leq \epsilon_r \leq 2.6$). This chapter demonstrates that the cladding permittivity can be strategically selected to provide a significant gain enhancement relative to a single layer DRA of the same length, without reducing the operational bandwidth. Variations of the cladding permittivity were achieved by implementing commercially available additive manufacturing (AM) techniques, and used to tune the peak gain in the extended Ku band (10-18 GHz). In particular, it is shown how a

The content of this chapter has been published in [65] and it is included in this dissertation with permission from the IEEE. A copy of the permission is included in the Appendix A-3.

cladding of $\epsilon_r = 1.6$ increases the antenna gain between 2.7 dB and 4.5 dB in the entire frequency range, comparable to a single layer (non-cladded) DRA that is 1.8 times longer. More generally, through simulation it is demonstrated that for the presented design a cladding permittivity to core permittivity ratio between 0.15 to 0.4 provides the best overall gain performance. In this range, the radiated fields along the antenna length are appropriately phased to maximize directionality without significant increase in the sidelobe level [65].

6.2. Dielectric Rod Antenna Design and Fabrication

The geometry of a traveling wave rod antenna is usually formed by three sections: a feed taper which is inserted into the rectangular waveguide feed to gradually match the input impedance; a body gradient; and, a constant height section to minimize the reflected surface wave [9, 66, 67]. For a DRA with circular cross-section, the diameter of the antenna $D1$ should satisfy (6.1) to ensure that the fundamental mode (HE_{11}) is supported

$$\frac{D1}{\lambda_0} < \frac{0.626}{\sqrt{\epsilon_r}} \quad (6.1)$$

where λ_0 is the free space wavelength [9]. The geometry should also satisfy (6.2) to guarantee that the fundamental mode is confined within the core, as for smaller diameters the electromagnetic energy is loosely guided [4].

$$D1 > \frac{\lambda_0}{4} \quad (6.2)$$

Since the DRA design in this work utilizes a rectangular cross-section, an equivalence radii between the two geometries (i.e rectangular and circular) is followed as a suitable approximation to satisfy (1) and (2) [50]. For a rectangle of 2:1 aspect ratio its equivalent diagonal $D1$ is then selected as $1.315 D$ according to [68]. The geometry of the multilayer antenna for the extended Ku band is depicted in Fig. 6-1. The antenna length determines the peak gain and the half power beamwidth, and in this type of antenna the total body length often falls within $3 \lambda_0$ and $6 \lambda_0$. As it will be seen later in this work DRAs with shorter electrical length show less gain variation with frequency across the band compared to longer rods, a short length makes easier to analyze the effect of the cladding. In this design a total length of 75 mm ($3.5 \lambda_0$ at the center frequency) was chosen as a baseline to study the effect of the cladding.

The DRA core was fabricated by laser cutting a Rogers RO3010 ($\epsilon_r=10.2$ and loss tangent=0.0035) substrate. The cladding is fabricated as a separate hollow structure using fused deposition modeling (FDM) of acrylonitrile butadiene styrene (ABS) ($\epsilon_r=2.6$ and loss tangent=0.0052). Two claddings were fabricated, one with 100% infill to achieve an effective cladding permittivity ϵ_r of 2.6 [50], and one with 50% honeycomb infill to achieve $\epsilon_r = 1.6$ at 18

GHz. An attractive feature of the multilayer DRA design is its compatibility with 3D printing technology. A fully 3D printed variation of this design was successfully implemented in the Ka band [69].

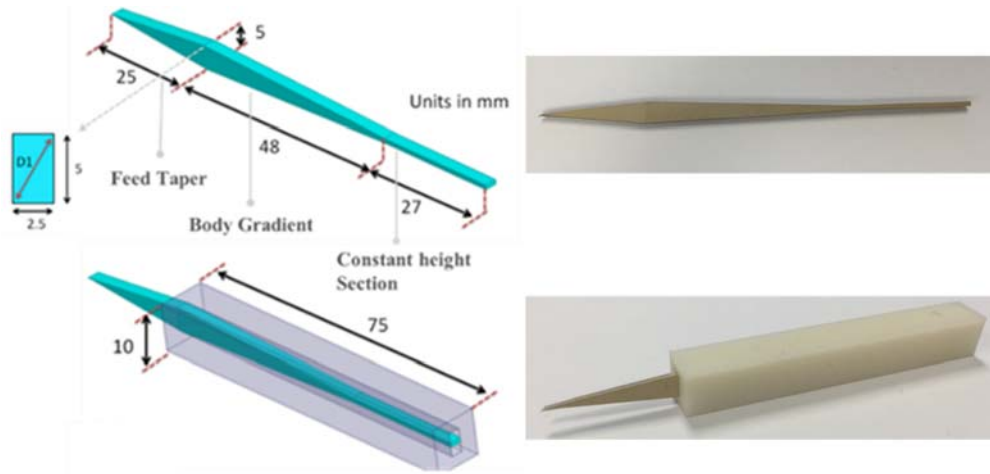


Figure 6-1: Proposed multilayer DRA geometry and key dimensions, showing the inner core (top) and multilayer design (bottom).

6.3. DRA Characterization and Measurements

The DRA performance was measured in an anechoic chamber with claddings permittivities of 1.6 and 2.6. The performance of the single layer or non-cladded design was also measured for comparison purposes. The resulting peak gain and corresponding HFSS simulations are shown in Fig. 6-2(a). The multilayer antenna with $\epsilon_r = 1.6$ cladding shows a significant gain improvement at all frequencies of interest compared to the non-cladded antenna of the same length. The multilayer antenna peak gain is 16.24 dBi at 17.2 GHz, representing a 4.44 dB improvement with respect to the single layer rod antenna. The multilayer design with a $\epsilon_r = 2.6$ cladding shows an enhanced gain in the low end of the Ku band and a comparable gain beyond 15 GHz when compared to the non-cladded rod performance. In this multilayer DRA a 14.6 dBi peak gain occurs at 12.2 GHz, representing a 4.8 dB gain increment. In all cases, the measured gain follows the simulated trend over frequency, however, the slight variations observed can be attributed to the presence of the fixture stage, and the feeding metallic waveguide on the back of the antenna under test.

Fig. 6-2 (b) presents a comparison of the measured and simulated return loss for the single and multilayer DRA with $\epsilon_r = 2.6$ cladding while Fig. 6-2 (c) shows the same comparison but with a cladding of $\epsilon_r = 1.6$. In both cases, the multilayer designs have an improved return loss at the low end of the frequency band, specifically from 9.7 dB to 25 dB for a $\epsilon_r = 2.6$ cladding and to 15 dB for a $\epsilon_r = 1.6$ cladding, both measured at 12.2 GHz. For the multilayer

DRAs, the return loss is greater than 10 dB across the entire frequency range. In summary, both multilayer DRA designs provide >4 dB peak gain improvements in the Ku band without a negative effect on the bandwidth when compared to a single layer design of the same length.

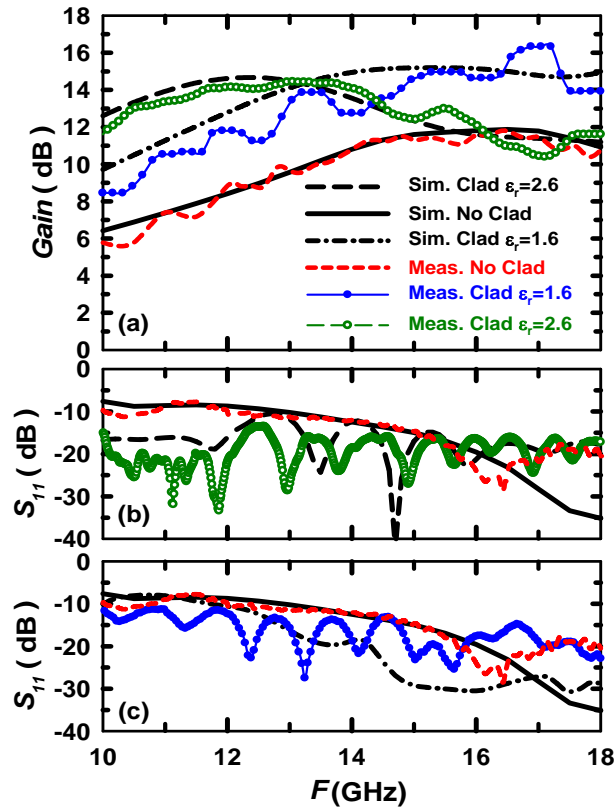


Figure 6-2: Measured and simulated peak gain (a) and reflection coefficient (b-c) of the single and multilayer DRA with different cladding permittivities.

The measured and simulated E-plane radiation patterns of the single and multilayer DRA with $\epsilon_r = 2.6$ cladding at 12.2 GHz are presented in Fig. 6-3. The radiated fields are affected by the presence of the cladding, as the half power beamwidth reduces from 61 degrees to 22 degrees in the multilayer design [50]. The end fire cross-polarization discrimination is 47 dB for the single layer DRA and 39 dB for the multilayer DRA at 12.2 GHz. Similarly, the measured and simulated E-plane radiation patterns at 17.2 GHz for the single and multilayer DRA with $\epsilon_r = 1.6$ cladding are shown in Fig. 6-4. In this case, the half power beamwidth reduces from 48 degrees to 28 degrees in the multilayer design. A measured front to back ratio of 26 dB is also achieved for the multilayer antenna. The end fire cross-polarization discrimination is 43 dB and 38 dB for the single and multilayer DRA, respectively.

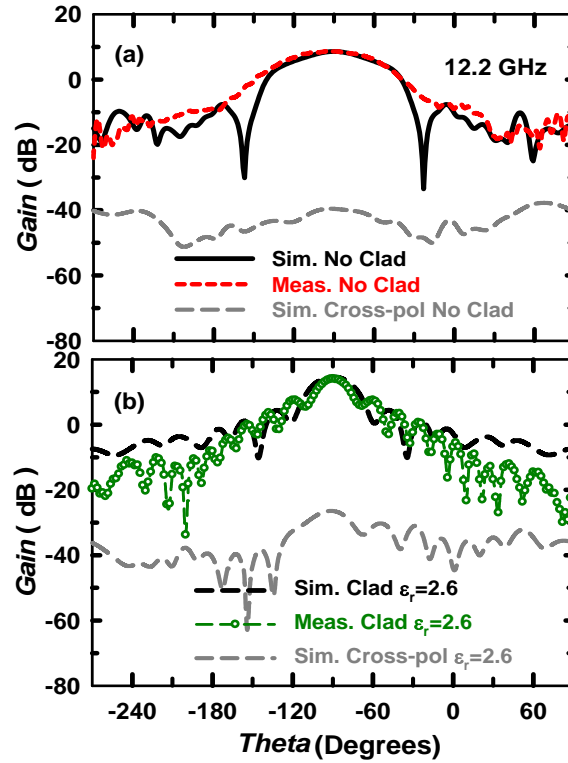


Figure 6-3: Measured and simulated E-plane radiation pattern for the single (top) and multilayer (bottom) DRA with $\epsilon_r = 2.6$ cladding at 12.2 GHz [50].

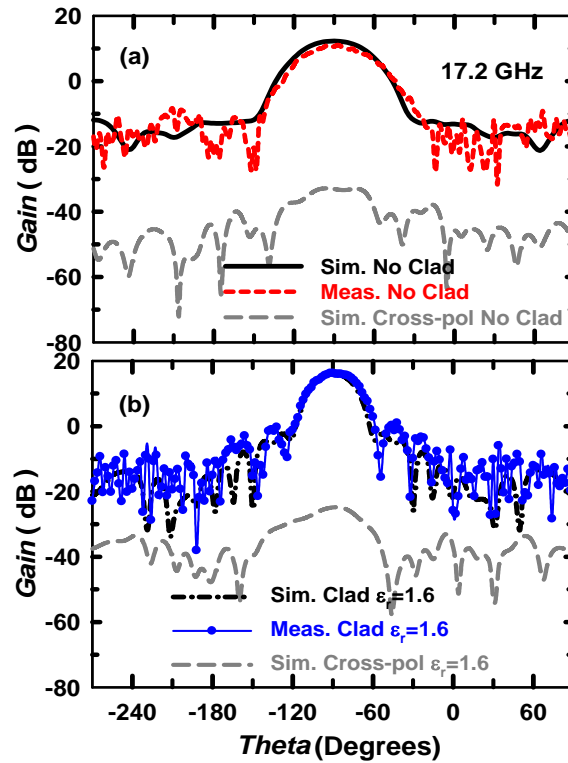


Figure 6-4: Measured and simulated E-plane radiation pattern for the single (top) and multilayer (bottom) DRA with $\epsilon_r = 1.6$ cladding at 17.2 GHz.

The addition of the low permittivity cladding results in a peak gain increment, which can be attributed to two effects: 1) an increase in the effective permittivity and thus the electrical length of the antenna, and 2) an increase in the field confinement that reshapes the radiation pattern and results in higher directivity. The electric field magnitude of the single and multilayer antenna with $\epsilon_r = 2.6$ cladding is presented in Fig. 6-5. It can be observed that in the multilayer DRA there is a higher portion of the E-field radiated in the end fire direction.

The 3D radiation pattern of the single and multilayer DRA at 17.2 GHz with $\epsilon_r = 1.6$ cladding is shown in Fig. 6-6(a) and 6-6(b), respectively. The corresponding E and H plane radiation patterns are plotted in Fig. 6-6(c) and 6-6(d) for the single and multilayer DRA, respectively. It can be seen that the symmetry of the radiation patterns in both planes are affected by the 2:1 core cross-section ratio. The differences in symmetry are more noticeable for the single layer DRA.

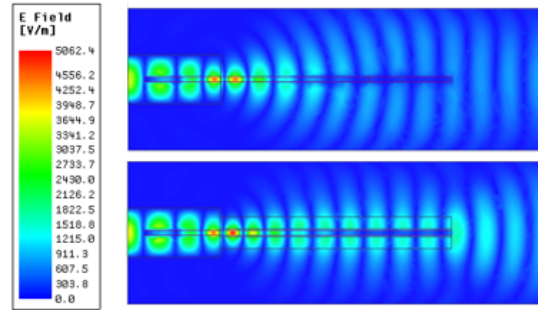


Figure 6-5: Simulated E-Field distribution at 17.2GHz for single (top), and multilayer (bottom) DRA with $\epsilon_r = 2.6$ cladding.

Fig. 6-7 shows the simulated non-cladded DRA peak gain versus frequency for different length increments (ΔL) of the core body gradient. The curve with the lowest gain ($\Delta L = 0$ mm) corresponds to the original design shown in Fig. 6-1 with no cladding. The gain versus frequency response of the multilayer DRA with $\epsilon_r = 1.6$ cladding is included in the plot as a reference. As shown, an increment of at least 60 mm is required to match the gain of the multilayer antenna at the center frequency; this represents a 2.25x increase in the body gradient length and a 1.8x increase in the total DRA length.

For frequencies above 15 GHz, an increment of 120 mm or 3.5 times the body gradient is necessary to match the multilayer DRA gain. It can be seen in Fig. 6-7 that increasing the rod length increases the gain in a non-uniform way. For frequencies above 14 GHz, the gain slowly decays due to an increase in the side lobe level (SLL) in the H plane. Additionally, increasing the antenna length from $\Delta L = 0$ to 140 mm reduces the cross-polarization discrimination at 18 GHz from 44 dB to 34 dB.

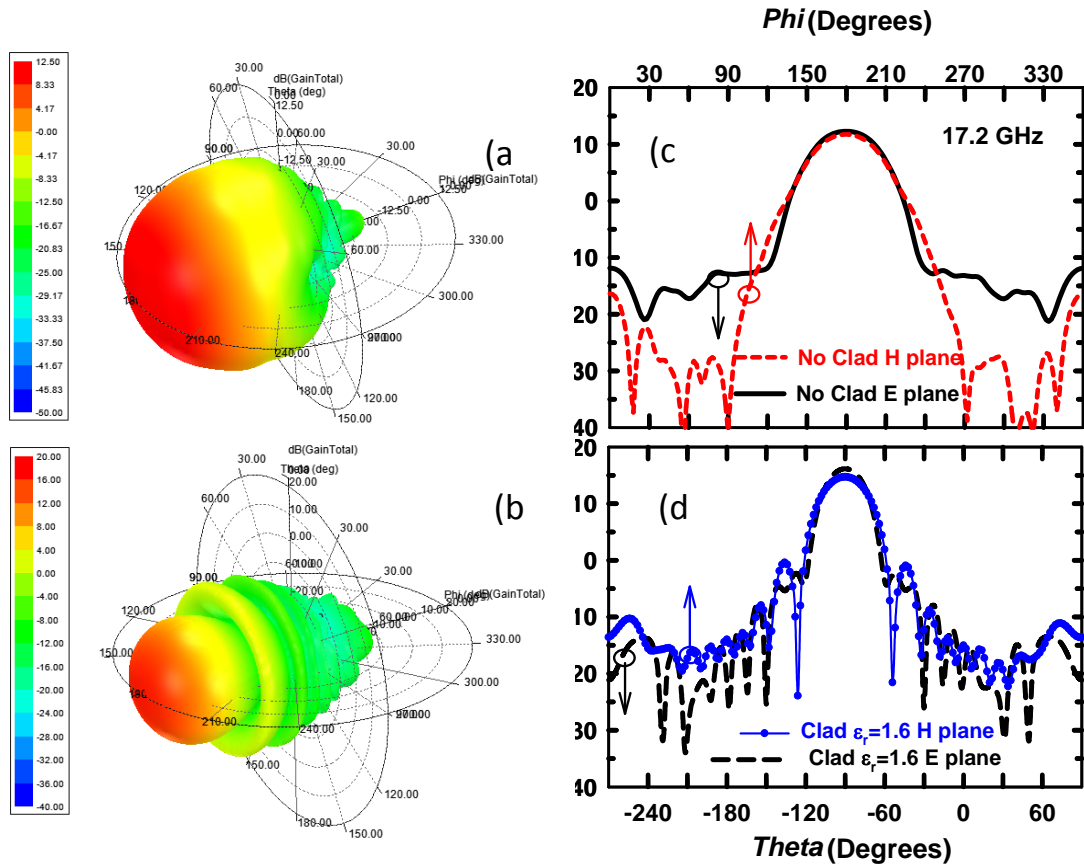


Figure 6-6: Simulated 3D radiation pattern for the single (a) and multilayer (b) DRA. Simulated E and H plane radiation patterns of the single (c) and multilayer (d) DRA with $\epsilon_r = 1.6$ cladding at 17.2 GHz.

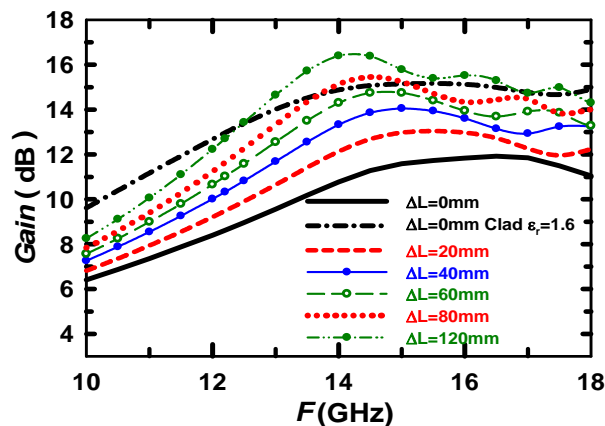


Figure 6-7: Simulated gain vs frequency for different length increments of the body gradient in a single layer DRA.

Fig. 6-8 presents the end-fire gain of the single and multilayer DRA with body gradient increments of 120 mm, 60 mm and 0 mm (original design). The cladding permittivity considered in the multilayer DRA is 1.6. It is seen

how the advantages of the cladding are scalable and consistent with different antenna lengths, providing significant gain increments when compared to a single layer rod of the same length.

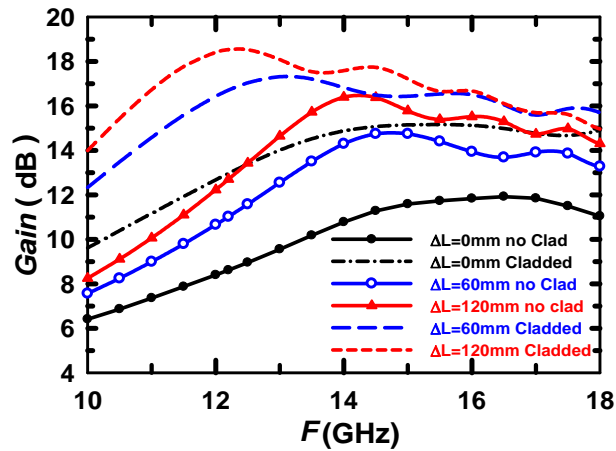


Figure 6-8: Simulated gain vs frequency for different length increments of the body gradient in a single and multilayer DRA.

6.4. Parametric Study of the Cladding Properties

Fig. 6-9 (a) and (b) show the simulated effect of the loss tangent variation of the core and the cladding on the multilayer DRA gain at 14 GHz and 18 GHz, respectively. The loss tangent ($\tan\delta$) values of the core and cladding were varied from 0 to 0.015. Two sets of curves are plotted in Fig. 6-9, one where the cladding $\tan\delta$ is varied (black curves) considering a Rogers RO3010 core and a lossless core, and one where the core $\tan\delta$ is varied (red curves) considering an ABS cladding and a lossless cladding. At both frequencies, the difference between the dashed and solid red lines (ABS and lossless cladding) is larger than the difference between the dashed and solid black lines (RO3010 and lossless core). The data show that selecting a lossy material ($\tan\delta=0.015$) over a low loss material ($\tan\delta=0.005$) for the DRA cladding yields a ~ 0.5 dB reduction of the end-fire gain. Therefore, it can be concluded that the cladding loss tangent variation has a more significant effect on the multilayer DRA gain than the variation of the core loss tangent in the same range of values. This behavior can be attributed to the higher portion of the electromagnetic field that is radiated through the cladding in comparison to the core.

The simulated effects of varying the cladding permittivity on the gain of the multilayer DRA are presented in Fig. 6-10. The permittivity value is increased from $\epsilon_r=1$, which represents the absence of the cladding, up to a value of $\epsilon_r=10.2$ representing an identical material to that used for the core. Cladding permittivities between 1.6 and 2.6 provide a significant gain enhancement when compared to the gain response of the non-cladded antenna. The gain

increment in these cases can range from 1.8 dB up to 7 dB over frequency. Moreover, the frequency of the end-fire peak gain can be tuned within the Ku band by adjusting the cladding dielectric constant. For cladding permittivity values between 2.6 and 3.6, the gain improvement is only present in the lower end of the frequency band, thus worsening the antenna performance for higher frequencies. For all frequencies within the band, the best performance of the proposed multilayer DRA is achieved when a low permittivity material ($1.6 \leq \epsilon_r \leq 2.6$) is utilized.

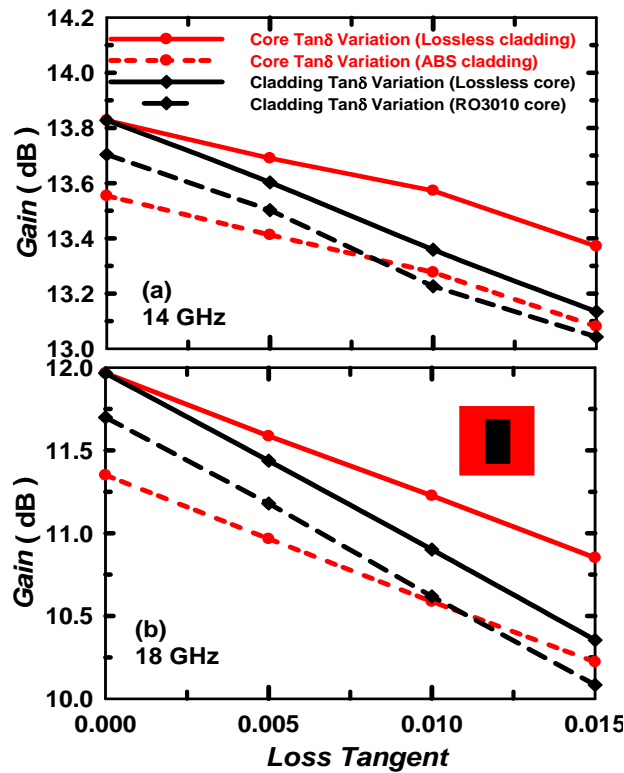


Figure 6-9: Simulated end-fire gain versus loss tangent variation at 14 GHz (a) and 18 GHz (b).

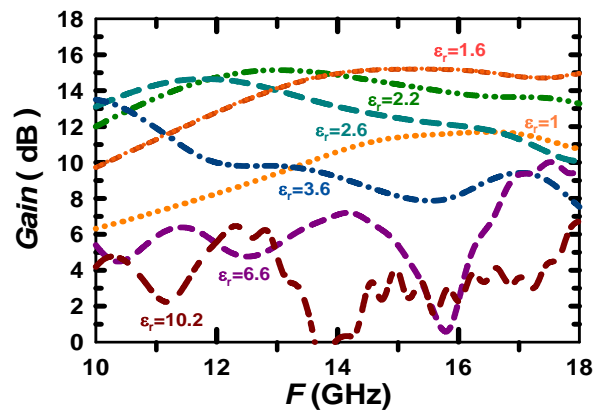


Figure 6-10: Simulated gain vs frequency for different cladding permittivities.

Fig. 6-11 shows the simulated end-fire peak gain versus the permittivity ratio $\epsilon_{\text{clad}}/\epsilon_{\text{core}}$. As in Fig. 6-10, the cladding permittivity was varied from 1 to 10.2 (the core permittivity value) corresponding to a permittivity ratio variation of 0.1 to 1. For all frequencies within the Ku band, the best performance of the proposed design is achieved when the cladding to core permittivity ratio lies between 0.15 and 0.4.

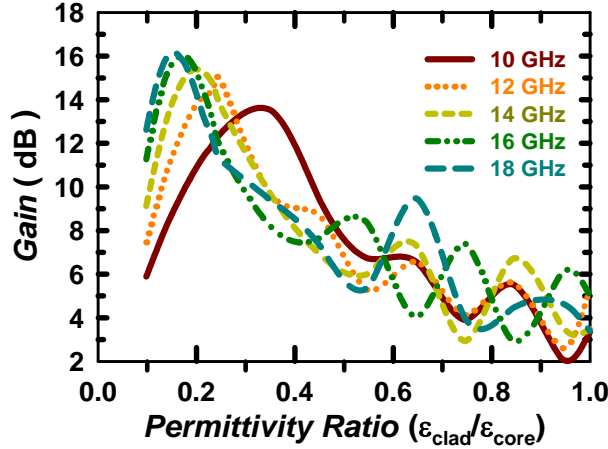


Figure 6-11: Simulated gain vs cladding to core permittivity ratio for different frequencies.

6.5. Conclusions

The effect of the cladding properties on the proposed multilayer DRA performance was studied. The multilayer DRA is formed by a high permittivity core ($\epsilon_r=10.2$) with rectangular cross-section, surrounded by a low permittivity cladding ($1.6 \leq \epsilon_r \leq 2.6$). It is found that enhancements in gain and beamwidth can be achieved by providing the proper dielectric loading with respect to a single layer design of the same length, without reducing the operational bandwidth. Simulated and measured data show that a low permittivity cladding can be utilized to tune the end fire peak gain to the desired frequency, from 12 GHz with $\epsilon_r = 2.6$ cladding to 17 GHz with $\epsilon_r = 1.6$ material. Physical changes to achieve the desired permittivity are easily obtained by modifying the printing infill factor of the thermoplastic material. A multilayer DRA with a $\epsilon_r = 1.6$ cladding shows a gain enhancement in the entire frequency band, with a peak gain improvement of 4.5 dBi and 20 degrees HPBW reduction at 17.2 GHz. The gain increment in the multilayer DRA with a cladding of $\epsilon_r = 1.6$ can be achieved by a DRA without cladding if the body tapered length is increased more than 2.25 times. The multilayer DRA also increases the electric field confinement in the core, which translates to a higher potential packing density in an array configuration.

CHAPTER 7: 3D PRINTED MULTILAYER MM-WAVE DIELECTRIC ROD ANTENNA WITH ENHANCED GAIN

7.1. Introduction

Dielectric traveling wave antennas are an attractive option for many applications in the upper microwave and mm-wave frequency range due to some key advantages including small size, high gain, broadband performance, and low loss depending on the constituent materials [1]. Dielectric devices typically have easier, less expensive fabrication process and more tolerance for geometric discontinuities as compared to metal devices.

In this chapter, a multilayer end-fire dielectric rod antenna is proposed for use at Ka-band. It is fabricated using additive manufacturing (AM), specifically fused deposition modeling (FDM), which is a low cost and minimum waste fabrication process. A ceramic composite that is compatible with FDM and has a higher dielectric constant than commercially-available 3D printing materials was used for the core. The addition of a low permittivity ABS cladding enhances the antenna gain performance in the entire frequency range. The proposed design has a rectangular cross section that offers the possibility of integration with mm-wave systems and it can be easily scaled to operate at other frequency ranges.

7.2. Preparation and Characterization of the Medium-K Electromagnetic Composite for FDM

Cyclo Olefin Polymer (COP) Zeonex[®] (RS420), an amorphous thermoplastic polymer, was used as the host matrix for the ceramic composite material that forms the DRA core. COP has a relative permittivity of 2.12, a low $\tan \delta < 0.0009$ measured at 17 GHz, and particle tapped density of 0.55 g/cm³. The MgCaTiO₂ particles used as micro-fillers were sintered at 1200°C for 3 hours and exhibit a density of 1.85 g/cm³ [2]. The FDM feedstock filament preparation process starts with the re-pulverization of the sintered MgCaTiO₂ ceramic using a high-energy ball milling tool, followed by a sieving process to ensure that the maximum particle sizes are below 38 μm. The COP thermoplastic matrix and 30 vol. % sintered ceramic particles are then uniformly mixed along with a hyperdispersant using a planetary centrifugal mixer followed by a hot extrusion process at 220°C, to produce filaments with a diameter of

The content of this chapter has been published in [63], and it is included in this dissertation with permission from the IEEE. A copy of the permission is included in the Appendix A-3.

about 2.0 mm. The complete fabrication, modeling and characterization of this medium-k and low loss electromagnetic composite is reported by Castro *et al.* [2].

The dielectric characterization in the mm-wave spectrum was performed using a model 400 circular cavity from Damaskos Inc. The electromagnetic properties of 3D-printed cylindrical shaped specimens made of 30 vol. % COP-MgCaTiO₂ were measured to be $\epsilon_r \sim 4.34$ and $\tan \delta \sim 0.0060$ at 44 GHz.

7.3. Dielectric Rod Antenna (DRA) Design and Fabrication

The physical geometry of the multilayer DRA is depicted in Fig 7-1(a). As presented in [3], the antenna is formed by a medium permittivity end-fire, traveling wave rod antenna surrounded by a low permittivity cladding. The DRA core is formed by 3 sections: a feed taper, a body gradient and a constant height section [4,5]. The antenna is fed by a straight rectangular waveguide (RWG) and the feed taper section of the DRA core is partially inserted into the rectangular waveguide to match the impedances of both waveguides.

The diameter d_1 of the antenna was approximated according to the design expression for circular dielectric rods: $d_1/\lambda_0 < 0.626 \sqrt{\epsilon_r}$, where λ_0 is the free space wavelength, to guarantee the HE₁₁ mode [4]. The ratio of H_1 to W_1 was selected as 2:1 to avoid cross polarization [6]. The total radiator body length determines the peak gain and HPBW and should fall within $3\lambda_0$ to $6\lambda_0$.

The DRA core is surrounded by the low-permittivity cladding with a square cross-section to improve the gain performance of the antenna. The dimensions of the antenna core and cladding were optimized using the High Frequency Structure Simulator (HFSS) software by Ansys. The resulting dimensions are: $L_1=17.7$ mm, $L_2=21.6$ mm, $L_3=18.2$ mm, $H_1=4$ mm, $W_1=2$ mm, $H_2=1$ mm, $W_C = H_C=16$ mm, $L_C=46.2$ mm.

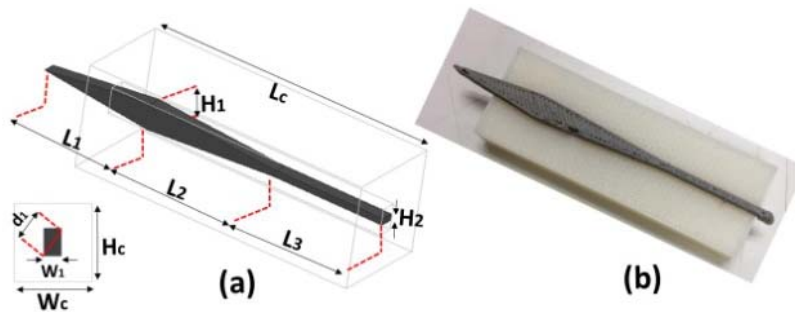


Figure 7-1: Antenna physical geometry and dimensions (a), and fabricated prototype (b).

The DRA was fabricated using direct digital manufacturing (DDM), specifically fused deposition of the medium-k composite for the core and ABS ($\epsilon_r=2.6$ and $\tan\delta=0.0052$ measured at 17 GHz) for the cladding. A layer height of 150 μm was used to print both materials, 100% infill was set to print the core and 60% infill to print the cladding to reduce the effective ABS permittivity to the designed value ($\epsilon_r=2$). Fig. 7-1(b) shows a picture of the fabricated multilayer antenna.

7.4. Measured Results

To measure the DRA, a transition to standard WR28 rectangular waveguide was implemented. A 50 micron layer of Rogers Ultralam 3850 liquid crystal polymer (LCP) ($\epsilon_r=3.14$, $\tan\delta=0.002$ @ 10 GHz) was cut into shape and attached to the RWG flange to hold the DRA core in the center during the measurement. Fig. 7-2 (a) shows the simulated and measured end-fire peak gain versus frequency of the DRA with and without the ABS cladding, while Fig. 7-2 (b) presents the measured and simulated reflection coefficient of the antenna with and without cladding. It can be noticed that the addition of the cladding improves the gain performance of the antenna over the entire frequency range by 3 dB to 8.5 dB and the measured return loss is greater than 10 dB in both cases within the entire frequency range. The peak gain response of the antenna is sensitive to the permittivity of the cladding and higher gain can be achieved through precise control of the infill to realize the desired permittivity.

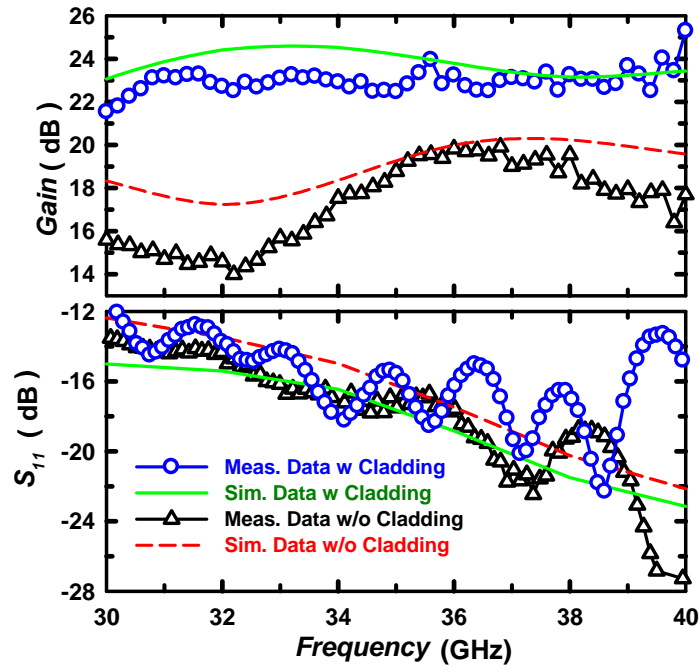


Figure 7-2: Measured and simulated gain vs frequency (top) and return loss (bottom) of the multilayer DRA.

The addition of the low-permittivity cladding has two effects on the antenna: (1) it increases the effective permittivity and consequently the electrical length of the antenna; (2) it increases the field confinement, which results in a more directive radiation pattern. Both effects contribute to the peak gain increase. Fig. 7-3 presents the simulated and measured E-plane radiation pattern of the DRA with and without the cladding at 35.6 GHz. It can be noticed that the incorporation of the cladding results in a peak gain increase of 4.3 dB and a half power beamwidth reduction from 40 degrees to 18 degrees at 35.6 GHz.

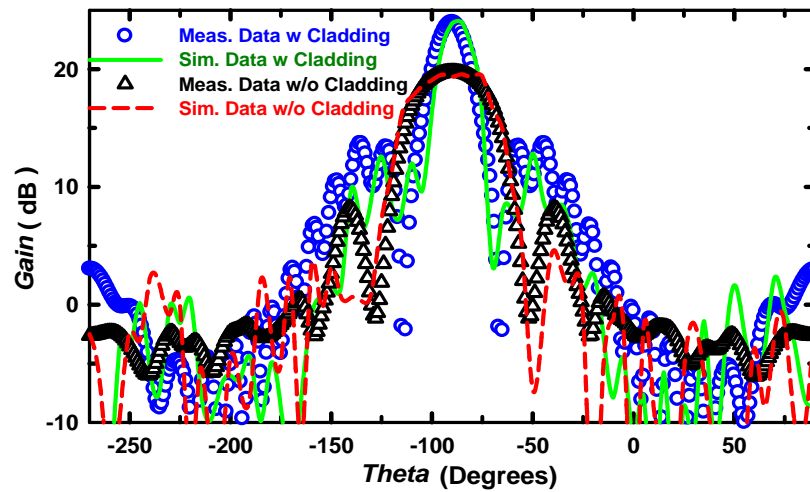


Figure 7-3: Measured and simulated E-plane radiation pattern without and with ABS cladding for the dielectric rod antenna at 35.6 GHz.

7.5. Conclusions

A multilayer dielectric rod antenna has been fabricated using fused deposition modeling of ABS thermoplastic and an in-house prepared COP-MgCaTiO₂ based composite material of higher-k than commercially-available materials for FDM. It has been demonstrated that encasing the antenna core inside a 16x16 mm² ABS cladding (60% infill) enhances the antenna peak gain in the entire frequency range (30 to 40 GHz) by up to 8.5 dB. The addition of the cladding also increases the antenna electrical length which makes it a low cost and convenient technique to miniaturize the dielectric rod waveguide while allowing expedited fabrication.

CHAPTER 8: KU BAND METAL-STRIP-LOADED DIELECTRIC ROD ANTENNA WITH NARROWBAND GAIN ENHANCEMENT

8.1. Introduction

The introduction of periodic metallic perturbations on one side of a dielectric rod antenna have been implemented to DRA for frequency scanning [70]. The perturbations can be considered as radiating elements excited by a surface wave propagated along the dielectric rod [60, 70, 71]. In this chapter, micro dispensed silver paste was used to create a metal grated pattern and to enhance the peak gain in a narrow band without increasing the antenna dimensions. Micro-dispensing was the fabrication method selected for the metal loading because it is a high precision (down to 100 microns), rapid prototyping and low cost option.

8.2. Metal-Strip-Loaded Dielectric Rod Antenna (MSL DRA) Design and Fabrication

The proposed design is comprised of a high permittivity dielectric rod core and periodic conductive strips as illustrated in Fig. 8-1. The antenna geometry was optimized for the Ku band using Ansys (HFSS) and the resulting dimensions are: $L_1=25$ mm, $L_2=48$ mm, $L_3=27$ mm, $H_1=5$ mm, $H_2=1$ mm, $L_m=2.25$ mm and $L_{gap}=3$ mm. As specified in [50] the physical geometry of a traveling wave rod antenna is formed by: a feed taper to gradually match the input impedance; a body gradient; and a constant height section to minimize the reflected surface wave.

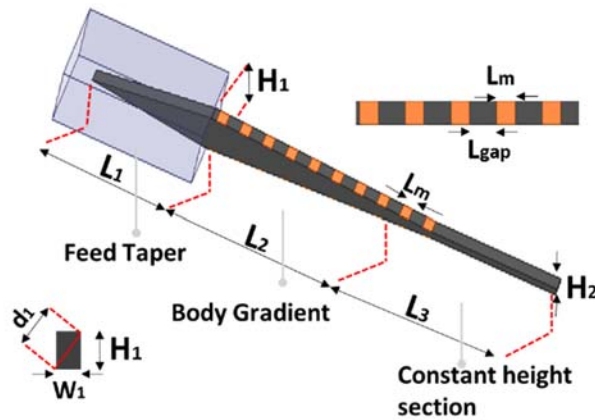


Figure 8-1: Antenna physical geometry and key parameters.

The material used for the DRA core is Rogers RO3010 ($\epsilon_r=10.2$ a loss tangent=0.0035) and it was cut into shape using a Rabbit HX-1290SE laser machine. The corrugated metal layer was micro-dispensed on the DRA top and bottom body gradient using DuPont CB028 silver paste in a nScript tabletop 3D printer. The dispensed conductive layer thickness is approximately 30 μm .

8.3. MSL DRA Characterization and Measured Results

To characterize the proposed antenna, a transition to standard WR-62 rectangular waveguide (RWG) was utilized. Fig. 8-2 presents the simulated and measured end-fire peak gain versus frequency of the DRA with and without the metal strip loading. The metal strip width is the same as the DRA core, the length is $L_m=2.25$ mm and the spacing is $L_{\text{gap}}=3$ mm. As shown in Fig. 8-2, the gain of the corrugated antenna is enhanced below 14 GHz and rapidly decays for higher frequencies. The position of the maximum peak gain can be adjusted by changing the periodicity of the metal strips.

Fig. 8-3 shows simulated data of the proposed antenna gain versus frequency for different metal strip lengths L_m . The frequency at which the maximum peak gain occurs decreases as the metal strip length increases, achieving up to 3 dB gain increment when compared to the its non-loaded counterpart. Table I summarizes the simulated maximum peak gain frequency for different values of L_m .

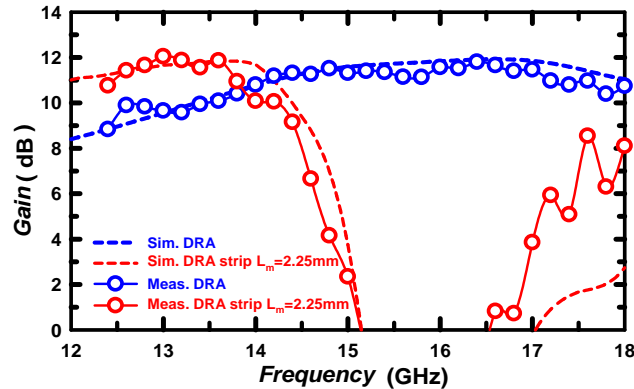


Figure 8-2: Measured and simulated gain vs frequency for the dielectric rod antenna with and without metal strips of $L_m=2.25$ mm.

The reflection coefficient of the MSL DRA remains under -10 dB for frequencies below the peak gain and rapidly increases to 0 dB as the peak gain rolls off. Fig. 8-4 shows the simulated and measured E field radiation pattern with and without the metal strip loading for $L_m=2.25$ mm ($0.27 \lambda_g$) and $L_{\text{gap}}=3$ mm at 13 GHz. The addition of the

metal loading increases the peak gain by 2 dB and the half power beamwidth (decreases from 64 degrees to 52 degrees at 13 GHz. A good agreement between the simulated and measured data was obtained, although some discrepancies in the back-lobe level are due to the measurement fixture and the back placed RWG transition.

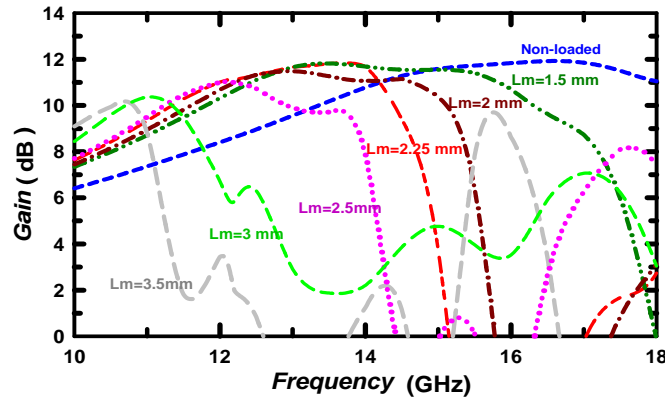


Figure 8-3: Simulated gain vs frequency for the DRA with metal strips of variable widths.

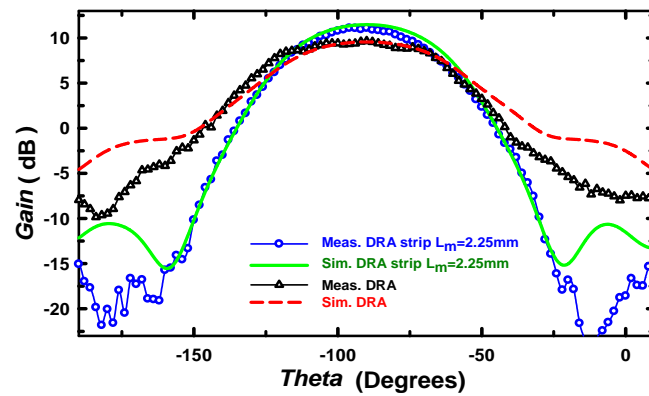


Figure 8-4: Measured and simulated E-plane radiation pattern without and with metal strips for the dielectric rod antenna at 13 GHz.

Table 8-1: Peak gain frequency and variation with LM.

L_m (mm)	Frequency (GHz)	Peak Gain Increment (dB)
Non-loaded	16.5	0
1.5	13.5	1.87
2.25	13	2.23
2.5	12	2.60
3	11	2.99
3.5	10.5	3.08

8.4. Conclusions

A micro-dispersed metal strip loading was implemented in a high permittivity dielectric rod antenna obtaining an optimum gain at a frequency determined by the metal pattern dimensions. For $L_m=2.25$ mm and $L_{gap}=3$ mm a 2 dB peak gain increment and a 12 degrees reduction of the HPBW was obtained at 13 GHz. To obtain an equivalent gain increment at 13 GHz without the addition of metal loading the DRA body gradient length needs to be increased by 50 mm. Simulated data demonstrate the dependency of the metal strip length and the maximum gain, a narrowband gain increment can be achieved by tuning the corrugated geometry without increasing the antenna dimensions.

CHAPTER 9: KU BAND BROADBAND TRANSITION FOR DIELECTRIC ROD WAVEGUIDES TO PLANAR TRANSMISSION LINES

9.1. Introduction

Dielectric rod waveguides offer many advantages such as low loss, broadband performance, low cost and their fabrication methods are usually simple. One of the challenges of dielectric waveguides is the implementation of effective transitions to standard metal-based waveguides, especially planar transmission lines. Transitions from dielectric waveguides to microstrip and CPWs at millimeter wave frequencies haven been proposed in the literature [46-49]. Significant attenuation values at high frequencies have been reported for transitions to microstrip, for example, transmission losses of 10 dB have been measured at 140 GHz in a transition from dielectric ribbon to CPW, where an 8 dB loss is attributed to the transition [46].

In this chapter a low loss broadband transition is designed and characterized at the Ku band. The proposed transition is compatible with dielectric rod waveguides and antennas with rectangular cross-section. Measured data indicate a loss of ~ 0.62 dB per transition at the center frequency. A feature of the proposed design is that it provides mechanical stability as opposed to a rectangular waveguide transition in which the DRW core should be positioned in the center of the hollow cavity. The proposed transition is easily removable and non-invasive to the dielectric structures under test. Planar transitions also allow the possibility of simpler feed designs for multiple dielectric rod waveguide and antenna arrays.

9.2. Transition Design and Fabrication

9.2.1. Design Considerations

The proposed transition for DRW to planar transmission lines is illustrated in Fig. 9-1. The dielectric rod waveguide core is tapered and inserted in a low dielectric constant layer contained between two metal parallel plates. The height of the low permittivity layer is tapered down to form the microstrip substrate and the top parallel metal plate is tapered in width to create the microstrip trace. The dimensions of the transition were optimized in Ansys (HFSS) for the Ku band and the resulting parameter dimensions are presented in table I.

The cross-section area of the parallel plate section was initially set to the dimension of a RWG filled with the low permittivity dielectric. The microstrip width was selected to be 50Ω at the center frequency. The transition was characterized in the Ku band with an end launch K connector. A top ground is added on each side of the microstrip trace to also allow measurements by GSG probing.

Two dielectric rod waveguides are measured with the proposed transition, a single layer dielectric rod (DRW) and a multilayer dielectric rod (MDRW). The DRW is formed by a high permittivity dielectric ($\epsilon_r=10.2$) with rectangular cross-section. The height to width ratio of the rod was selected as 2:1 to avoid field degeneracies [50]. In the multilayer dielectric rod the DRW is completely surrounded by a low permittivity cladding ($\epsilon_r=2.1$) to extent the waveguide operational bandwidth [50]. The cladding height H_C and width W_C are presented in table I, and they match the transition parallel plate cross-section area.

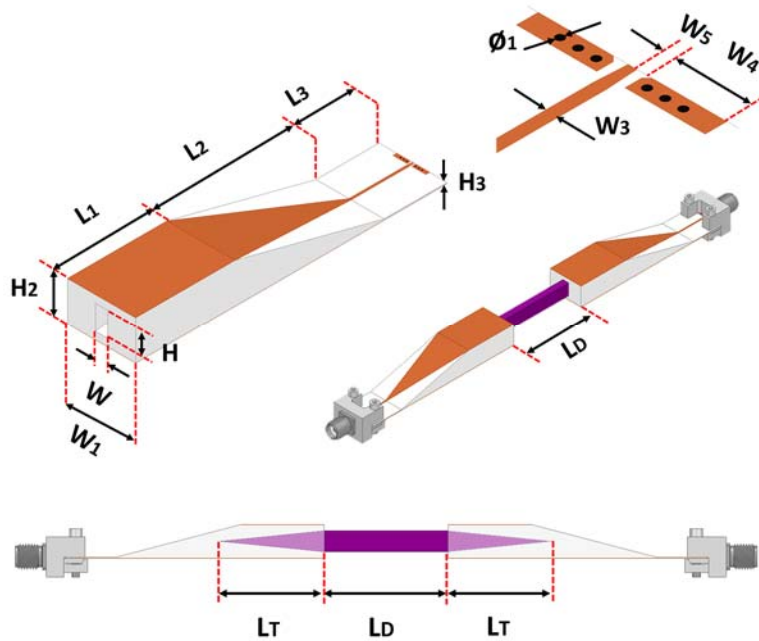


Figure 9-1: Proposed transition geometry and key parameters.

Fig. 9-2 shows the electric field magnitude in the proposed transition and the DRW. The parallel plate section E field in the Z direction excites the fundamental mode of the DRW, the $E_{z_{11}}$ mode. In the DRW most of the electric field propagates in the center of the waveguide core.

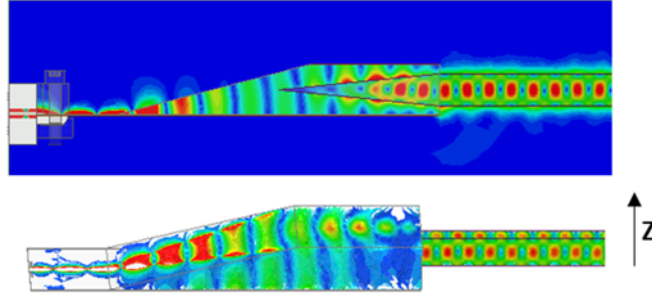


Figure 9-2: Electric field magnitude in the proposed transition and DRW at 20 GHz.

Table 9-1: Transition dimensions of interest.

Parameter		Dimension (mm)
DRW tapered length	L_T	25
DRW length	L_D	55
DRW width	W	2.5
DRW height	H	5
DRW cladding width	W_C	15.8
DRW cladding height	H_C	7.9
Microstrip substrate thickness	H_3	0.254
Microstrip trace width	W_3	0.639
Microstrip length	L_3	12.7
Microstrip top ground width	W_4	2.8
Via diameter	ϕ_1	0.3
Transition tapered section length	L_2	30
Parallel plate length	L_1	20
Parallel plate height	H_1	7.9
Parallel plate width	W_1	15.8
Signal-ground spacing	W_5	0.343

9.2.2. Fabrication

The DRW was made from Rogers RO3010 ($\epsilon_r=10.2$ and loss tangent=0.0035) and it was cut into shape using a Rabbit HX-1290SE laser machine. The low permittivity cladding of the MDRW was made from PTFE Teflon ($\epsilon_r=2.1$ and loss tangent=0.0005) and was patterned by CNC machining. The proposed transition was fabricated by fused deposition modeling (FDM) of Zeonex®RS420 ($\epsilon_r=2.1$ and loss tangent=0.0008). Zeonex is an amorphous thermoplastic polymer based on Cyclo Olefin Polymer (COP). The transition dielectric was printed as one piece using 100 μm layer height and a 100% infill. The transition metal traces were fabricated using photolithography on Rogers liquid crystalline polymer LCP ULTRALAM® 3850 laminate. The LCP has a 25 μm thickness and 18 μm copper cladding.

9.3. Characterization and Measured Data

The measured and simulated S parameters of the proposed back to back transition connected to a 55 mm long DRW and MDRW are presented in Fig. 9-3 (a) and (b) respectively. The transition was characterized from 12 to 21 GHz using an end launch K connector from Southwest Microwave. The measured attenuation at 16 GHz is 2.5 dB in both cases. It can be noticed from Fig 9-3 that the addition of the cladding in the MDRW does not negatively affect the attenuation, this is due to most of the E field being propagated inside the waveguide core. The MDRW extends the waveguide 1 dB cut-off frequency by 1.7 GHz when compared to the single layer DRW. The attenuation of a back to back rectangular waveguide transition to the same 55 mm DRW is approximately 1.25 dB at 16 GHz, which is only 1.25 dB lower than the attenuation obtained with the proposed transition. An excellent match between the simulated and measured data was obtained, as observed in Fig. 9-3.

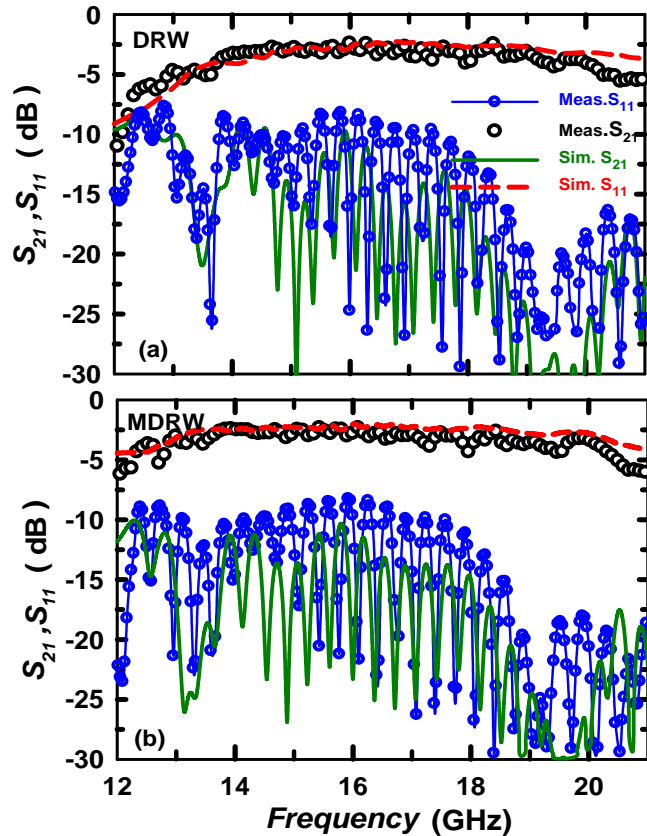


Figure 9-3: Measured and simulated S parameters of the back to back transition with a 55 mm DRW (a) and MDRW (b).

9.4. Transition Loss Analysis

The attenuation due to the dielectric rod waveguide is approximately 0.023 dB/mm and was calculated applying the multilayer method [57, 58] to measured data of dielectric rod of different length. To determine the loss due to each transition a thru connection was characterized. The thru connection of the proposed transition is illustrated in Fig. 9-4 and the simulated and measured S parameters are presented in Fig. 9-5. The small discrepancies between the measured and simulated data in this case can be attributed to the difficulties in achieving a tight connection between the two transitions without an air gap in between.

Simulated data shows an attenuation of 1.16 dB at 16 GHz, which indicates 0.58 dB loss per transition. To isolate the contribution of each source of loss, the total attenuation of the proposed transition with a 55 mm MDRW was simulated under different material loss conditions. The resulting simulated data is presented in Fig. 9-6. The curve with highest attenuation (solid black line) results from all the materials having their respective loss tangent values. This curve matches the measured data of Fig. 9-3 (b) and it shows an attenuation at 16 GHz of 0.25 dB.

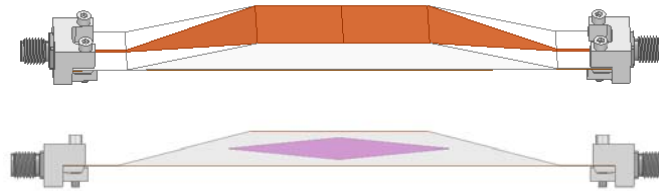


Figure 9-4: Proposed transition thru connection.

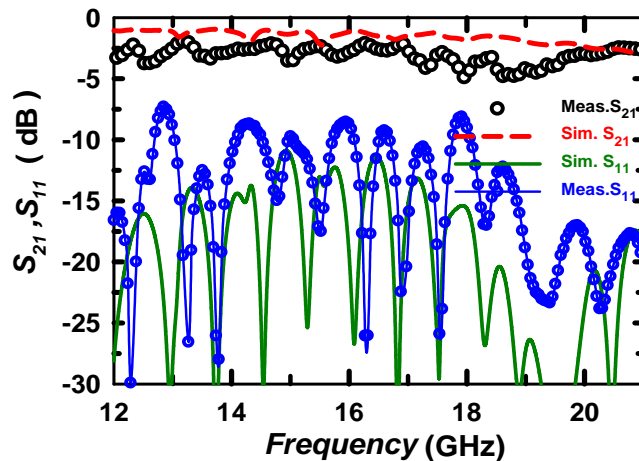


Figure 9-5: Measured and simulated S parameters of the proposed transition thru connection.

The first condition considers a lossless cladding, the resulting attenuation is the same as the one for a lossy cladding. As mentioned previously, the cladding does not negatively affect the attenuation of the DRW. The second condition considers both a lossless cladding and a lossless DRW core, in this case the attenuation reduces considerably, reaching ~ 1.1 dB at 16 GHz. The third condition evaluates a lossless cladding, a lossless DRW and a lossless Zeonex. In this case the attenuation at 16 GHz decrease to ~ 0.9 dB, it is a small reduction due to the low loss tangent value of the actual Zeonex. The last condition considers all the previous assumptions plus a perfect electric conductor for all metal layers. In this case the attenuation at 16 GHz is in average ~ 0.5 dB. This result indicates that for a back to back transition the radiation loss at the center frequency is approximate 0.5 dB.

The attenuation of a back to back transition to RWG with a lossless MDRW was included in Fig. 9-6 as a reference. The resulting attenuation at 16 GHz in that case is 0.13 dB, which is only 0.37 dB lower than the one obtained with the proposed transition.

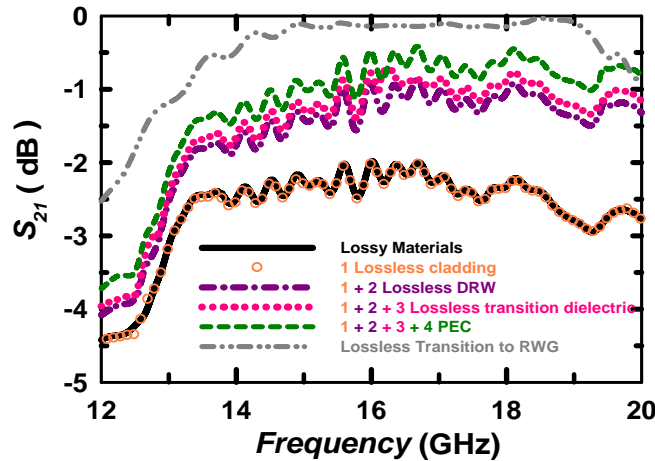


Figure 9-6: Simulated transmission coefficient of the proposed back to back transition under different material loss conditions.

9.5. DRA Planar Feed Characterization and Measured Data

The proposed transition was also used to characterize a dielectric rod antenna (DRA) and a multilayer dielectric rod antenna (MDRA). The geometry of the antenna is illustrated in Fig. 9-7 (a) and the transition with a DRA and MDRA is shown in Fig 9-7 (b) and (c) respectively. The DRA core is made from RO3010 and the cladding is made from Teflon as it was done for the multilayer dielectric rod waveguide.

Fig. 9-8 presents the measured and simulated antenna end fire peak gain of the single and multilayer DRA with the proposed transition. The measured end fire gain at 16 GHz is 12.3 dBi for the DRA and 15.2 dBi for the

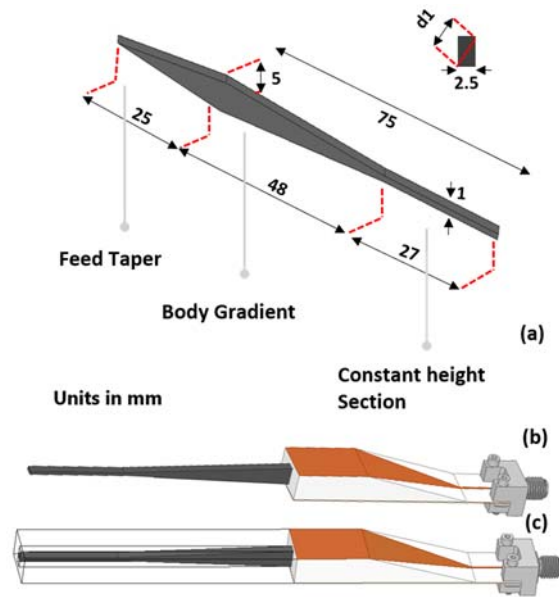


Figure 9-7: DRA geometry and key dimensions (a), proposed transition with a single (b) and with a multilayer DRA (c).

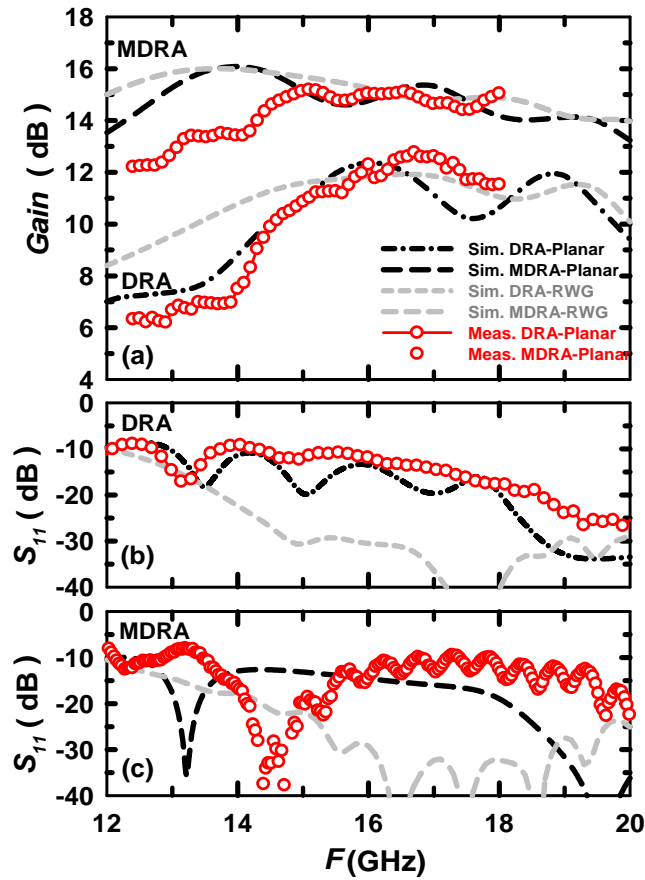


Figure 9-8: Measured and simulated peak gain (a) and reflection coefficient (b-c) of the DRA and MDRA.

MDRA. Fig. 9-8 shows a good agreement between the measured and simulated data. A difference in the MDRA measured and simulated data at the low end of the band can be attributed to misalignments during the measurements product of the cladding weight pulling down the antenna core. The simulated antenna gain with a transition to RWG has been included as a reference, for both a DRA and MDRA. It can be noticed that the antennas end-fire gain obtained with a RWG transition and with the proposed transition are comparable in the entire frequency range, especially for the MDRA. Fig 9-8 (b) and (c) show the measured and simulated return loss for the DRA and MDRA respectively. In both cases the reflection coefficient remains below -10 dB from 12 to 20 GHz.

Fig. 9-9 presents the E-field radiation pattern for the DRA (a) and MDRA (b) at 16.5 GHz. The half power beamwidth is 44 degrees for the DRA and to 37 degrees for the MDRA. The end-fire peak gain is 11.88 dBi and 15.3 dBi for the DRA and MDRA respectively. It can be noticed that the radiation pattern for the MDRA is more symmetric. Fig. 9-10 shows a good agreement between the measured and simulated data.

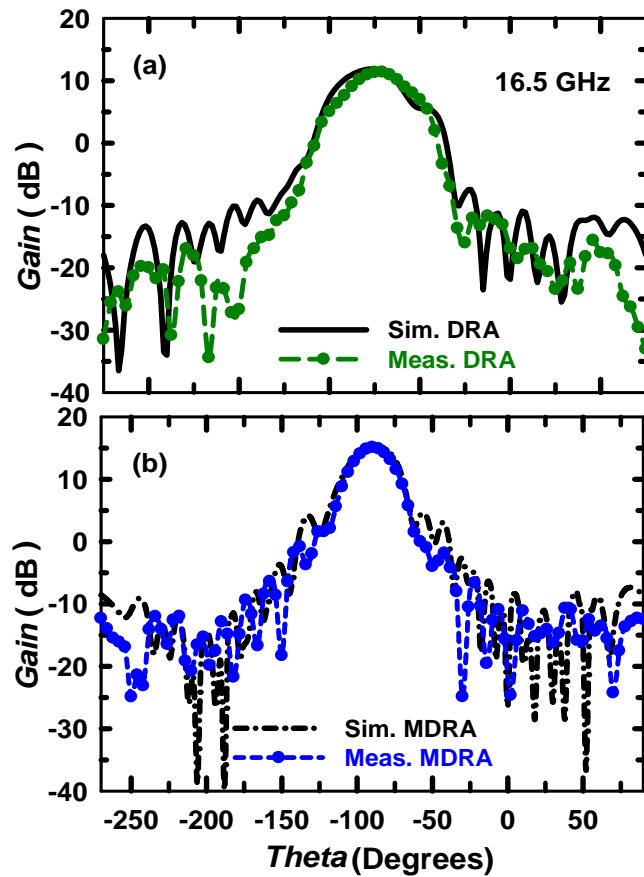


Figure 9-9: Measured and simulated E-plane radiation pattern for the single DRA (a) and multilayer DRA (b) at 16.5 GHz.

The simulated E field distribution for the DRA and MDRA with the proposed transition at 20 GHz is presented in Fig. 9-10 (top) and (bottom) respectively. It can be noticed that for the MDRA there is a higher portion of the E field radiated in the end-fire direction which leads to a higher gain. From Fig. 9-10 (top) it can be observed that there is an asymmetry in the E-plane field radiation of the DRA, this is due to the asymmetry of the transition feed. Fig. 9-10 (bottom) shows that since the cladding increases the field confinement, the radiation pattern is more symmetric as a result.

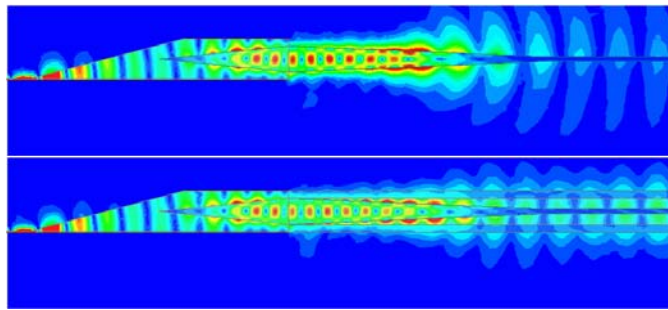


Figure 9-10: Simulated E-Field distribution at 20 GHz for single (top), and multilayer (bottom) DRA.

9.6. Conclusions

A broadband Ku band transition for dielectric rod waveguides to microstrip has been presented. The transition was used to characterize a single layer and multilayer dielectric rod waveguide and dielectric end-fire antenna. The transition performance was compared to a corresponding transition to RWG. All measurements were performed with a K band end launch connector, but the proposed transition design also allows measurements using a GSG probing. The attenuation of a back to back transition with a 55 mm dielectric rod waveguide is ~ 2.5 dB at the center frequency. Considering that the DRW has an attenuation of ~ 0.023 dB/mm, the attenuation per transition is ~ 0.62 dB per transition, from which ~ 0.25 dB is due to radiation and ~ 0.37 dB is due to material loss. The attenuation values of the MDRA and DRA are the same, but the MDRA extends the 1 dB operational bandwidth by 1.7 dB when compared to the DRA.

The measured antenna peak gain with the proposed transition to microstrip is 12.3 dBi and 15.2 dBi for the DRA and MDRA respectively. The end fire gain values obtained with the proposed transition are comparable to the resulting values if a RWG transition was implemented instead. The addition of the cladding in the MDRA increases the field confinement and it also improves the symmetry in the radiation pattern.

CHAPTER 10: RECOMMENDATIONS AND FUTURE WORK

1. It has been shown in this work D band (110-170 GHz) measurements of a dielectric rod waveguide design using D band extension modules. Further measurements can be performed with different dielectrics to achieve less attenuation at this frequency range.
2. A grating metal pattern has been implemented in a Ku Band dielectric rod waveguide to obtain a band stop filter behavior. The stop band center frequency can be adjusted by varying the periodicity of the metal strips. It is suggested the development of an equivalent circuit model to aid in the design of these filters.
3. A broadband transition from dielectric rods to planar transmission lines has been presented and characterized at the Ku band. The transition substrate was fabricated using fused deposition modeling and the metal traces with photolithography. Further test needs to be carried out to deposit the transition metal traces using micro-dispensing so it could be completely fabricated by additive manufacturing.
4. One of the advantages of the proposed transition is that facilitated the design of multiple feeds for dielectric rod waveguides and antennas. Additional simulations need to be performed to implement this transition as a dielectric rod antenna array feed.

REFERENCES

- [1] J. Tang, J. A. Hejase, J. C. Myers, S. R. Connor, D. M. Dreps, and J. Kuczynski, "A dielectric based waveguide integrated in a multilayer PCB for ultra high speed communications," in *2016 IEEE 25th Conference on Electrical Performance Of Electronic Packaging And Systems (EPEPS)*, 2016, pp. 197-200.
- [2] O. Mitrofanov, R. James, F. A. Fernandez, T. K. Mavrogordatos, and J. A. Harrington, "Reducing Transmission Losses in Hollow THz Waveguides," *IEEE Transactions on Terahertz Science and Technology*, vol. 1, pp. 124-132, 2011.
- [3] Y. Liu and X. Chen, "A Novel Microstrip-fed Dielectric ROD Antenna Array with High Gain," presented at the Progress In Electromagnetics Research Symposium Proceedings, Moscow, Russia, 2012.
- [4] R. Kazemi, A. E. Fathy, and R. A. Sadeghzadeh, "Dielectric Rod Antenna Array With Substrate Integrated Waveguide Planar Feed Network for Wideband Applications," *IEEE Transactions on Antennas and Propagation*, vol. 60, pp. 1312-1319, 2012.
- [5] K. Kumar, J. S. Sandhu, B. Bisht, P. Gupta, and G. Singh, "Dual-Band Dielectric Rod Antenna for Satellite Communication System," in *Communication Systems and Network Technologies (CSNT), 2011 International Conference on*, 2011, pp. 242-245.
- [6] C.-C. Chen, K. Rama Rao, and R. Lee, "A new ultrawide-bandwidth dielectric-rod antenna for ground-penetrating radar applications," *IEEE Transactions on Antennas and Propagation*, vol. 51, pp. 371-377, 2003.
- [7] N. Ghassemi and K. Wu, "Planar Dielectric Rod Antenna for Gigabyte Chip-to-Chip Communication," *IEEE Transactions on Antennas and Propagation*, vol. 60, pp. 4924-4928, 2012.
- [8] J. Richter, D. Notel, F. Kloppel, J. Huck, H. Essen, and L. p. Schmidt, "A Multi-Channel Radiometer with Focal Plane Array Antenna for W-Band Passive Millimeterwave Imaging," in *2006 IEEE MTT-S International Microwave Symposium Digest*, 2006, pp. 1592-1595.
- [9] J.-H. Qiu and N.-N. Wang, "Optimized dielectric rod antenna for millimeter wave FPA imaging system," in *Imaging Systems and Techniques, 2009. IST '09. IEEE International Workshop on*, 2009, pp. 147-150.
- [10] W. Fang, P. Fei, and F. Nian, "Millimetre-wave end-fired antenna array for active 3D holographic imaging system," *Electronics Letters*, vol. 50, pp. 341-343, 2014.
- [11] A. Elsherbini, C. Zhang, L. Song, M. Kuhn, A. Kamel, A. E. Fathy, *et al.*, "UWB antipodal vivaldi antennas with protruded dielectric rods for higher gain, symmetric patterns and minimal phase center variations," in *2007 IEEE Antennas and Propagation Society International Symposium*, 2007, pp. 1973-1976.

- [12] S. K. Mustafa and S. Yasir, "Design, development and testing of dielectric tapered rod feed for parabolic reflector antenna as an alternate to feed horns," in *Applied Sciences and Technology (IBCAST), 2013 10th International Bhurban Conference on*, 2013, pp. 369-371.
- [13] J. Y. Chung and C. C. Chen, "Two-Layer Dielectric Rod Antenna," *IEEE Transactions on Antennas and Propagation*, vol. 56, pp. 1541-1547, 2008.
- [14] S. K. Chatterjee and R. Chatterjee, "Dielectric loaded waveguides-a review of theoretical solutions. Part 2: Propagation through dielectric loaded waveguides," *Radio and Electronic Engineer*, vol. 30, pp. 195-205, 1965.
- [15] K. A. O'Connor and R. D. Curry, "Simulation of compact high power antenna concepts loaded by double-positive metamaterials," in *Pulsed Power Conference (PPC), 2015 IEEE*, 2015, pp. 1-5.
- [16] R. A. Ramirez and T. M. Weller, "Dielectric-loaded end-fire slot antenna with low back-lobe radiation for UHF RFID applications," in *2016 International Workshop on Antenna Technology (iWAT)*, 2016, pp. 186-188.
- [17] O. P. Leisten, "Capability and manufacturability: Some considerations concerning the current status of multi-filar dielectric loaded antennas," in *Antennas and Propagation Conference (LAPC), 2014 Loughborough*, 2014, pp. 7-12.
- [18] T. P. Ketterl, Y. Vega, N. C. Arnal, J. W. I. Stratton, E. A. Rojas-Nastrucci, C. M. F. *et al.*, "A 2.45 GHz Phased Array Antenna Unit Cell Fabricated Using 3-D Multi-Layer Direct Digital Manufacturing," *IEEE Transactions on Microwave Theory and Techniques*, vol. 63, pp. 4382-4394, 2015.
- [19] E. A. Rojas-Nastrucci, T. Weller, V. Lopez Aida, C. Fan, and J. Papapolymerou, "A study on 3D-printed coplanar waveguide with meshed and finite ground planes," in *Wireless and Microwave Technology Conference (WAMICON), 2014 IEEE 15th Annual*, 2014, pp. 1-3.
- [20] J. Castro, E. Rojas, A. Ross, T. Weller, and J. Wang, "Fabrication, Modeling and Application of Ceramic-Thermoplastic Composites for Fused Deposition Modeling of Microwave Components," *IEEE Transactions on Microwave Theory and Techniques*, vol. 65, pp. 2073-2084, June 2017.
- [21] M. F. Córdoba-Eraza, E. A. Rojas-Nastrucci, and T. Weller, "Simultaneous RF electrical conductivity and topography mapping of smooth and rough conductive traces using microwave microscopy to identify localized variations," in *2015 IEEE 16th Annual Wireless and Microwave Technology Conference (WAMICON)*, 2015, pp. 1-4.
- [22] J. Castro, E. Rojas, T. Weller, and J. Wang, "High-k and low-loss polymer composites with co-fired Nd and Mg-Ca titanates for 3D RF and microwave printed devices: Fabrication and characterization," in *Wireless and Microwave Technology Conference (WAMICON), 2015 IEEE 16th Annual*, 2015, pp. 1-5.
- [23] J. C. Myers, J. A. Hejase, J. Tang, and D. M. Dreps, "Embedded filtering in PCB integrated ultra high speed dielectric waveguides using photonic band gap structures," in *2017 IEEE 26th Conference on Electrical Performance of Electronic Packaging and Systems (EPEPS)*, 2017, pp. 1-3.

- [24] M. Nitas, V. Salonikios, S. Raptis, and T. V. Yioultsis, "Analysis and design of fully planar CSRR-enhanced substrate-integrated waveguides and slot antennas for 5G communications," in *2018 7th International Conference on Modern Circuits and Systems Technologies (MOCAST)*, 2018, pp. 1-5.
- [25] F. Töpfer, S. Dudorov, and J. Oberhammer, "Millimeter-Wave Near-Field Probe Designed for High-Resolution Skin Cancer Diagnosis," *IEEE Transactions on Microwave Theory and Techniques*, vol. 63, pp. 2050-2059, 2015.
- [26] S. Atakramians, S. Afshar V, T. M. Monroe, and D. Abbott, "Terahertz dielectric waveguides," *Advances in Optics and Photonics*, vol. 5, pp. 169-215, 2013/06/30 2013.
- [27] Q. Zhong, Z. Chen, N. Sharma, S. Kshattray, W. Choi, and K. O. Kenneth, "300-GHz CMOS QPSK transmitter for 30-Gbps dielectric waveguide communication," in *2018 IEEE Custom Integrated Circuits Conference (CICC)*, 2018, pp. 1-4.
- [28] A. Malekabadi, S. A. Charlebois, D. Deslandes, and F. Boone, "High-Resistivity Silicon Dielectric Ribbon Waveguide for Single-Mode Low-Loss Propagation at F/G-Bands," *IEEE Transactions on Terahertz Science and Technology*, vol. 4, pp. 447-453, July 2014.
- [29] H. Kogelnik, "Theory of Dielectric Waveguides," in *Integrated Optics*, T. Tamir, Ed., ed Berlin, Heidelberg: Springer Berlin Heidelberg, 1975, pp. 13-81.
- [30] C. R. Doerr and H. Kogelnik, "Dielectric Waveguide Theory," *Journal of Lightwave Technology*, vol. 26, pp. 1176-1187, 2008.
- [31] S. Atakramians, S. A. V, B. M. Fischer, D. Abbott, and T. M. Monroe, "Porous fibers: a novel approach to low loss THz waveguides," *Optics Express*, vol. 16, pp. 8845-8854, 2008/06/09 2008.
- [32] S. Atakramians, S. Afshar V, H. Ebendorff-Heidepriem, M. Nagel, B. M. Fischer, D. Abbott, *et al.*, "THz porous fibers: design, fabrication and experimental characterization," *Optics Express*, vol. 17, pp. 14053-14062, 2009/08/03 2009.
- [33] X. Yang and P. P. Chahal, "On-Wafer Terahertz Ribbon Waveguides Using Polymer-Ceramic Nanocomposites," *IEEE Transactions on Components, Packaging and Manufacturing Technology*, vol. 5, pp. 245-255, 2015.
- [34] S. Atakramians, S. Afshar, T. M. Monroe, and D. Abbott, "Terahertz dielectric waveguides," *Adv. Opt. Photon.* 5, 2013.
- [35] M. Grzeskowiak, J. Emond, S. Protat, G. Lissorgues, F. Deshours, E. Richalot, *et al.*, "Optimization of a Quasi Loss Less Air-Cavity Inverted Microstrip Line from Microwave to Millimeter-Wave Frequencies and Comparison with the Coplanar Goubau Line at 60 GHz," *Progress In Electromagnetics Research C*, vol. 43, pp. 67-78, 2013.
- [36] W. T. Khan, A. Ulusoy, and J. Papapolymerou, "D-Band characterization of co-planar wave guide and microstrip transmission lines on liquid crystal polymer," in *2013 IEEE 63rd Electronic Components and Technology Conference*, 2013, pp. 2304-2309.



- [37] L. Vincetti, "Hollow core photonic band gap fiber for THz applications," *Microwave and Optical Technology Letters*, vol. 51, pp. 1711-1714, 2009.
- [38] O. Mitrofanov and J. A. Harrington, "Dielectric-lined cylindrical metallic THz waveguides: mode structure and dispersion," *Optics Express*, vol. 18, pp. 1898-1903, 2010/02/01 2010.
- [39] J. C. S. Ponceca, R. Pobre, E. Estacio, N. Sarukura, A. Argyros, M. C. Large, *et al.*, "Transmission of terahertz radiation using a microstructured polymer optical fiber," *Optics Letters*, vol. 33, pp. 902-904, 2008/05/01 2008.
- [40] A. Dupuis, J.-F. Allard, D. Morris, K. Stoeffler, C. Dubois, and M. Skorobogatiy, "Fabrication and THz loss measurements of porous subwavelength fibers using a directional coupler method," *Optics Express*, vol. 17, pp. 8012-8028, 2009/05/11 2009.
- [41] K. Nielsen, H. K. Rasmussen, A. J. L. Adam, P. C. M. Planken, O. Bang, and P. U. Jepsen, "Bendable, low-loss Topas fibers for the terahertz frequency range," *Optics Express*, vol. 17, pp. 8592-8601, 2009/05/11 2009.
- [42] C. Yeh and F. Shimabukuro, *The Essence of Dielectric Waveguides*, 2008.
- [43] C. Yeh, F. Shimabukuro, and P. H. Siegel, "Low-loss terahertz ribbon waveguides," *Applied Optics*, vol. 44, pp. 5937-5946, 2005/10/01 2005.
- [44] X. Yang and P. Chahal, "THz ribbon waveguides using polymer-ceramic nanocomposites," presented at the 2012 IEEE 62nd Electronic Components and Technology Conference, San Diego, CA, 2012.
- [45] S. Dudorov, "Rectangular Dielectric Waveguide and its Optimal Transition to a Metal Waveguide," Helsinki University of Technology, 2002.
- [46] J. Vaes, I. Ocket, W.-L. Tsai, M. Cauwe, P. Reynaert, and B. Nauwelaers, "A PCB-Embedding Scheme for LCP Ribbon Waveguide at D band," presented at the 2018 IEEE MTT-S International Microwave Symposium, Philadelphia, PA, 2018.
- [47] B. Yu, Y. Liu, Y. Ye, X. Liu, and Q. J. Gu, "Low-loss and Broadband G-Band Dielectric Interconnect for Chip-to-Chip Communication," *IEEE Microwave and Wireless Components Letters*, vol. 26, pp. 478-480, 2016.
- [48] J. Richter, Y. Yazici, C. Ziegler, and L. P. Schmidt, "A Broadband Transition between Dielectric and Planar Waveguides at Millimeterwave Frequencies," in *Microwave Conference, 2003 33rd European*, 2003, pp. 947-950.
- [49] W.-L. Tsai, I. Ocket, J. Vaes, M. Cauwe, P. Reynaert, and B. Nauwelaers, "Novel Broadband Transition for Rectangular Dielectric Waveguide to Planar Circuit Board at D Band," presented at the 2018 IEEE MTT-S International Microwave Symposium, Philadelphia, PA, 2018.
- [50] D. Lugo, R. A. Ramirez, J. Wang, and T. Weller, "Low Permittivity Cladding to Improve the Performance of Dielectric Rod Waveguides and Dielectric End-Fire Antennas," presented at the 2016 IEEE MTT-S International Microwave Symposium, San Francisco, CA, 2016.


- [51] E. A. J. Marcatili, "Dielectric Rectangular Waveguide and Directional Coupler for Integrated Optics," *Bell System Technical Journal*, vol. 48, pp. 2071-2102, 1969.
- [52] J. E. Goell, "A circular-harmonic computer analysis of rectangular dielectric waveguides," *The Bell System Technical Journal*, vol. 48, pp. 2133-2160, Sept. 1969.
- [53] A. S. Sudbo, "Why are accurate computations of mode fields in rectangular dielectric waveguides difficult?," *Journal of Lightwave Technology*, vol. 10, pp. 418-419, 1992.
- [54] N. Ranjkesh, M. Basha, A. Taeb, A. Zandieh, S. Gigoyan, and S. Safavi-Naeini, "Silicon-on-Glass Dielectric Waveguide Part I: For Millimeter-Wave Integrated Circuits," *IEEE Transactions on Terahertz Science and Technology*, vol. 5, pp. 268-279, 2015.
- [55] D. C. Lugo, R. A. Ramirez, J. Castro, J. Wang, and T. M. Weller, "Ku-band additive manufactured multilayer dielectric rod waveguide," presented at the 2017 IEEE 18th Wireless and Microwave Technology Conference (WAMICON), Cocoa Beach, FL, 2017.
- [56] D. M. Pozar, *Microwave engineering*: Fourth edition. Hoboken, NJ : Wiley, [2012] ©2012, 2012.
- [57] R. B. Marks, "A multilayer method of network analyzer calibration," *IEEE Transactions on Microwave Theory and Techniques*, vol. 39, pp. 1205-1215, 1991.
- [58] M. D. Janezic and J. A. Jargon, "Complex permittivity determination from propagation constant measurements," *IEEE Microwave and Guided Wave Letters*, vol. 9, pp. 76-78, Feb 1999.
- [59] J. C. Myers, J. A. Hejase, J. Tang, and D. M. Dreps, "Embedded filtering in PCB integrated ultra high speed dielectric waveguides using photonic band gap structures," presented at the 2017 IEEE 26th Conference on Electrical Performance of Electronic Packaging and Systems (EPEPS), San Jose, CA., 2017.
- [60] S. Kobayashi, R. Lampe, R. Mittra, and S. Ray, "Dielectric rod leaky-wave antennas for millimeter-wave applications," *IEEE Transactions on Antennas and Propagation*, vol. 29, pp. 822-824, 1981.
- [61] R. B. Dyott, O. Lawn, and T. D. Monte, "Microwave Transition Using Dielectric Waveguides," USA Patent, 1997.
- [62] R. Kazemi, A. E. Fathy, and R. A. Sadeghzadeh, "Design guidelines for multi-layer dielectric rod antennas fed by Vivaldi antennas," *IET Microwaves, Antennas & Propagation*, vol. 6, pp. 884-892, 2012.
- [63] C.-W. Liu, "Development of Automatic Design Optimization Method for Ultrawide Bandwidth (UWB) Multi-Layer Dielectric Rod Antenna," The Ohio State University, 2011.
- [64] Y. Luo and Z. N. Chen, "Compressed Dipoles Resonating at Higher Order Modes With Enhanced Directivity," *IEEE Transactions on Antennas and Propagation*, vol. 65, pp. 5697-5701, 2017.
- [65] D. Lugo, R. A. Ramirez, J. Wang, and T. Weller, "Multilayer Dielectric End-Fire Antenna with Enhanced Gain," *IEEE Antennas and Wireless Propagation Letters*, pp. 1-1, 2018.

- [66] G. E. Mueller and W. A. Tyrrell, "Polyrod antennas," *Bell System Technical Journal*, The, vol. 26, pp. 837-851, 1947.
- [67] T. Milligan, "Design of polyrod and corrugated-rod antennas," *Antennas and Propagation Magazine, IEEE*, vol. 42, pp. 88-91, 2000.
- [68] C. Balanis, *Antenna Theory Analysis and Design*, 3rd ed. New Jersey, USA: John Wiley & Sons, 2005.
- [69] D. C. Lugo, R. A. Ramirez, J. Castro, J. Wang, and T. M. Weller, "3D printed multilayer mm-wave dielectric rod antenna with enhanced gain," presented at the 2017 IEEE International Symposium on Antennas and Propagation & USNC/URSI National Radio Science Meeting, San Diego, CA, 2017.
- [70] K. L. Klohn, R. E. Horn, H. Jacobs, and E. Freibergs, "Silicon Waveguide Frequency Scanning Linear Array Antenna," *IEEE Transactions on Microwave Theory and Techniques*, vol. 26, pp. 764-773, 1978.
- [71] M. Guglielmi, Z. M. Lu, J. Encinar, S. T. Peng, and A. A. Oliner, "Metal-strip-loaded rectangular dielectric rod leaky-wave antennas: experimental verification of a new simple theory," presented at the Antennas and Propagation Society International Symposium, 1990. AP-S. Merging Technologies for the 90's. Digest., Dallas, TX, USA, 1990.

APPENDIX A: COPYRIGHT PERMISSIONS

A.1. Permissions for Chapter 3

Home Create Account Help 



Title: Low permittivity cladding to improve the performance of dielectric rod waveguides and dielectric end-fire antennas

Conference Proceedings: 2016 IEEE MTT-S International Microwave Symposium (IMS)

Author: Denise C. Lugo

Publisher: IEEE

Date: May 2016

Copyright © 2016, IEEE

LOGIN

If you're a **copyright.com** user, you can login to RightsLink using your copyright.com credentials. Already a **RightsLink user** or want to [learn more?](#)

Thesis / Dissertation Reuse

The IEEE does not require individuals working on a thesis to obtain a formal reuse license, however, you may print out this statement to be used as a permission grant:

Requirements to be followed when using any portion (e.g., figure, graph, table, or textual material) of an IEEE copyrighted paper in a thesis:

- 1) In the case of textual material (e.g., using short quotes or referring to the work within these papers) users must give full credit to the original source (author, paper, publication) followed by the IEEE copyright line © 2011 IEEE.
- 2) In the case of illustrations or tabular material, we require that the copyright line © [Year of original publication] IEEE appear prominently with each reprinted figure and/or table.
- 3) If a substantial portion of the original paper is to be used, and if you are not the senior author, also obtain the senior author's approval.

Requirements to be followed when using an entire IEEE copyrighted paper in a thesis:

- 1) The following IEEE copyright/ credit notice should be placed prominently in the references: © [year of original publication] IEEE. Reprinted, with permission, from [author names, paper title, IEEE publication title, and month/year of publication]
- 2) Only the accepted version of an IEEE copyrighted paper can be used when posting the paper or your thesis on-line.
- 3) In placing the thesis on the author's university website, please display the following message in a prominent place on the website: In reference to IEEE copyrighted material which is used with permission in this thesis, the IEEE does not endorse any of [university/educational entity's name goes here]'s products or services. Internal or personal use of this material is permitted. If interested in reprinting/republishing IEEE copyrighted material for advertising or promotional purposes or for creating new collective works for resale or redistribution, please go to http://www.ieee.org/publications_standards/publications/rights/rights_link.html to learn how to obtain a License from RightsLink.

If applicable, University Microfilms and/or ProQuest Library, or the Archives of Canada may supply single copies of the dissertation.

BACK

CLOSE WINDOW

Copyright © 2018 [Copyright Clearance Center, Inc.](#) All Rights Reserved. [Privacy statement](#). [Terms and Conditions](#).

Comments? We would like to hear from you. E-mail us at customercare@copyright.com

A.2. Permissions for Chapter 4



RightsLink®

Home

Create Account

Help



Title: Ku-band additive manufactured multilayer dielectric rod waveguide
Conference Proceedings: 2017 IEEE 18th Wireless and Microwave Technology Conference (WAMICON)
Author: Denise C. Lugo
Publisher: IEEE
Date: April 2017
Copyright © 2017, IEEE

LOGIN
If you're a **copyright.com** user, you can login to RightsLink using your copyright.com credentials. Already a **RightsLink** user or want to [learn more?](#)

Thesis / Dissertation Reuse

The IEEE does not require individuals working on a thesis to obtain a formal reuse license, however, you may print out this statement to be used as a permission grant:

Requirements to be followed when using any portion (e.g., figure, graph, table, or textual material) of an IEEE copyrighted paper in a thesis:

- 1) In the case of textual material (e.g., using short quotes or referring to the work within these papers) users must give full credit to the original source (author, paper, publication) followed by the IEEE copyright line © 2011 IEEE.
- 2) In the case of illustrations or tabular material, we require that the copyright line © [Year of original publication] IEEE appear prominently with each reprinted figure and/or table.
- 3) If a substantial portion of the original paper is to be used, and if you are not the senior author, also obtain the senior author's approval.

Requirements to be followed when using an entire IEEE copyrighted paper in a thesis:

- 1) The following IEEE copyright/ credit notice should be placed prominently in the references: © [year of original publication] IEEE. Reprinted, with permission, from [author names, paper title, IEEE publication title, and month/year of publication]
- 2) Only the accepted version of an IEEE copyrighted paper can be used when posting the paper or your thesis on-line.
- 3) In placing the thesis on the author's university website, please display the following message in a prominent place on the website: In reference to IEEE copyrighted material which is used with permission in this thesis, the IEEE does not endorse any of [university/educational entity's name goes here]'s products or services. Internal or personal use of this material is permitted. If interested in reprinting/republishing IEEE copyrighted material for advertising or promotional purposes or for creating new collective works for resale or redistribution, please go to http://www.ieee.org/publications_standards/publications/rights/rights_link.html to learn how to obtain a License from RightsLink.

If applicable, University Microfilms and/or ProQuest Library, or the Archives of Canada may supply single copies of the dissertation.

BACK

CLOSE WINDOW

Copyright © 2018 [Copyright Clearance Center, Inc.](#) All Rights Reserved. [Privacy statement](#), [Terms and Conditions](#).

Comments? We would like to hear from you. E-mail us at customer@copyright.com

A.3. Permissions for Chapter 6



RightsLink®

Home

Create Account

Help



Title: Multilayer Dielectric End-Fire Antenna with Enhanced Gain
Author: Denise Lugo
Publication: IEEE Antennas and Wireless Propagation Letters
Publisher: IEEE
Date: Dec 31, 1969
Copyright © 1969, IEEE

LOGIN

If you're a **copyright.com** user, you can login to RightsLink using your copyright.com credentials. Already a **RightsLink** user or want to [learn more?](#)

Thesis / Dissertation Reuse

The IEEE does not require individuals working on a thesis to obtain a formal reuse license, however, you may print out this statement to be used as a permission grant:

Requirements to be followed when using any portion (e.g., figure, graph, table, or textual material) of an IEEE copyrighted paper in a thesis:

- 1) In the case of textual material (e.g., using short quotes or referring to the work within these papers) users must give full credit to the original source (author, paper, publication) followed by the IEEE copyright line © 2011 IEEE.
- 2) In the case of illustrations or tabular material, we require that the copyright line © [Year of original publication] IEEE appear prominently with each reprinted figure and/or table.
- 3) If a substantial portion of the original paper is to be used, and if you are not the senior author, also obtain the senior author's approval.

Requirements to be followed when using an entire IEEE copyrighted paper in a thesis:

- 1) The following IEEE copyright/ credit notice should be placed prominently in the references: © [year of original publication] IEEE. Reprinted, with permission, from [author names, paper title, IEEE publication title, and month/year of publication]
- 2) Only the accepted version of an IEEE copyrighted paper can be used when posting the paper or your thesis on-line.
- 3) In placing the thesis on the author's university website, please display the following message in a prominent place on the website: In reference to IEEE copyrighted material which is used with permission in this thesis, the IEEE does not endorse any of [university/educational entity's name goes here]'s products or services. Internal or personal use of this material is permitted. If interested in reprinting/republishing IEEE copyrighted material for advertising or promotional purposes or for creating new collective works for resale or redistribution, please go to http://www.ieee.org/publications_standards/publications/rights/rights_link.html to learn how to obtain a License from RightsLink.

If applicable, University Microfilms and/or ProQuest Library, or the Archives of Canada may supply single copies of the dissertation.

BACK

CLOSE WINDOW

Copyright © 2018 [Copyright Clearance Center, Inc.](#) All Rights Reserved. [Privacy statement.](#) [Terms and Conditions.](#)

Comments? We would like to hear from you. E-mail us at customercare@copyright.com

A.4. Permissions for Chapter 7



RightsLink®

Home

Create Account

Help



Title: 3D printed multilayer mm-wave dielectric rod antenna with enhanced gain
Conference Proceedings: 2017 IEEE International Symposium on Antennas and Propagation & USNC/URSI National Radio Science Meeting
Author: Denise C. Lugo
Publisher: IEEE
Date: July 2017
Copyright © 2017, IEEE

LOGIN

If you're a **copyright.com** user, you can login to RightsLink using your copyright.com credentials. Already a **RightsLink** user or want to [learn more?](#)

Thesis / Dissertation Reuse

The IEEE does not require individuals working on a thesis to obtain a formal reuse license, however, you may print out this statement to be used as a permission grant:

Requirements to be followed when using any portion (e.g., figure, graph, table, or textual material) of an IEEE copyrighted paper in a thesis:

- 1) In the case of textual material (e.g., using short quotes or referring to the work within these papers) users must give full credit to the original source (author, paper, publication) followed by the IEEE copyright line © 2011 IEEE.
- 2) In the case of illustrations or tabular material, we require that the copyright line © [Year of original publication] IEEE appear prominently with each reprinted figure and/or table.
- 3) If a substantial portion of the original paper is to be used, and if you are not the senior author, also obtain the senior author's approval.

Requirements to be followed when using an entire IEEE copyrighted paper in a thesis:

- 1) The following IEEE copyright/ credit notice should be placed prominently in the references: © [year of original publication] IEEE. Reprinted, with permission, from [author names, paper title, IEEE publication title, and month/year of publication]
- 2) Only the accepted version of an IEEE copyrighted paper can be used when posting the paper or your thesis on-line.
- 3) In placing the thesis on the author's university website, please display the following message in a prominent place on the website: In reference to IEEE copyrighted material which is used with permission in this thesis, the IEEE does not endorse any of [university/educational entity's name goes here]'s products or services. Internal or personal use of this material is permitted. If interested in reprinting/republishing IEEE copyrighted material for advertising or promotional purposes or for creating new collective works for resale or redistribution, please go to http://www.ieee.org/publications_standards/publications/rights/rights_link.html to learn how to obtain a License from RightsLink.

If applicable, University Microfilms and/or ProQuest Library, or the Archives of Canada may supply single copies of the dissertation.

BACK

CLOSE WINDOW

Copyright © 2018 [Copyright Clearance Center, Inc.](#) All Rights Reserved. [Privacy statement](#). [Terms and Conditions](#).

Comments? We would like to hear from you. E-mail us at customer@copyright.com

ABOUT THE AUTHOR

Denise Lugo-Muñoz received the Professional Electronics Engineer degree in 2009 and the Master of Science in Electronics Engineering, with a major in Solid State Electronics, in 2011, both from Universidad Simón Bolívar, Caracas, Venezuela. From 2009-2013, she worked as a Research Assistant at USB's Solid State Electronics Laboratory, where she carried out research activities in the areas of physics based modeling, simulation and parameter extraction of MOSFETs, PIN diodes and Solar Cells. She graduated "Cum Laude" from her undergraduate engineering studies, her Master's thesis was awarded a mention of "Outstanding," and her Master's degree was conferred "With Honors." In her Master's Thesis she dealt with modeling and parameter extraction of SOI PIN diodes for applications from cryogenic to above room temperatures, within the framework of an international research project with colleagues in Brazil and Belgium.

In fall 2013, she joined the WAMI Research Center at USF as a member of the RF and Microsystems group. In 2015, she received her Master of Science in Electrical Engineering with a concentration in RF and Microwave from University of South Florida where she continued her Ph.D studies in Electrical Engineering. Her doctoral research is focused on the design and characterization of 3D printed microwave and mm - wave dielectric rod waveguides (DRW), dielectric rod antennas (DRA) and low loss transitions from dielectric waveguide to microstrip. In the development of her research project she worked with fused deposition modeling (FDM) of thermoplastics and ceramic composites, S - parameters measurements of DRW with frequency extension modules, rectangular waveguide calibration, antenna gain and radiation pattern measurements in anechoic chamber, photolithography and electromagnetic simulation of 3D dielectric structures using the High Frequency Structure Simulator (HFSS) software by Ansys.